12-2015

Failure Simulations at Multiple Length Scales in High Temperature Structural Alloys

Chao Pu
University of Tennessee - Knoxville, cpu@vols.utk.edu

To the Graduate Council:

I am submitting herewith a dissertation written by Chao Pu entitled "Failure Simulations at Multiple Length Scales in High Temperature Structural Alloys." I have examined the final electronic copy of this dissertation for form and content and recommend that it be accepted in partial fulfillment of the requirements for the degree of Doctor of Philosophy, with a major in Materials Science and Engineering.

Yanfei Gao, Major Professor

We have read this dissertation and recommend its acceptance:

Peter Liaw, Haixuan Xu, Timothy Truster

Accepted for the Council:
Carolyn R. Hodges

Vice Provost and Dean of the Graduate School

(Original signatures are on file with official student records.)

Failure Simulations at Multiple Length Scales in High Temperature Structural Alloys

A Dissertation Presented for the

Doctor of Philosophy

Degree

The University of Tennessee, Knoxville

Chao Pu

December 2015

Dedication

This doctoral dissertation is dedicated to my parents, my lovely wife, my parents-in-law and all beloved ones who unconditionally loved and supported me.

Acknowledgements

I would like to presents my sincere gratitude to those people who helped and supported me all through my Ph.D. study. Without their helps, I wouldn't finish this dissertation. I would like to give my greatest appreciation to my advisor, Professor Yanfei Gao for his devotion of countless time and efforts advising me for my doctoral research. During these years, he provided me with many valuable opportunities and wise advices helping me develop in the career. Also he is also a navigator for my personal life and makes my stay in USA easier and smoother.

I would also like express my gratitude to my doctoral committee members, Dr. Peter Liaw, Dr. Haixuan Xu and Dr. Timothy Truster. Our collaboration with Dr. Liaw and Dr. Haixuan Xu enriched my understanding from different scientific views of material study. Dr. Timothy Truster shared his profound knowledge in computational mechanics.

I feel so lucky to get the chance to work with Dr. Sam Sham, Dr. Yanli Wang, Mr. Robert Jetter and Dr. Kevin Walker at Oak Ridge National Laboratory. Their outstanding knowledge and great scientific enthusiasm impressed me and guided me in pursuing a successful academic career.

I enjoyed great time with my friends and colleagues who have constantly helped me and shared happiness together. They are Yuzhi Xia, Haoling Jia, Lu Huang, Jinbo Dou, Weidong Li, Lin Li, Yi Wang, Shuo Zhang, Xin Zhao, Peijun Hou, Tingkun Liu, Caijun Su, Yujie Meng, Peizhi Liu, Jianjiang Yang and many other peoples.

Finally, I want to acknowledge NSF, DOE and Joint Institute for Neutron Source for their funding for this work.

Abstracts

A number of computational methodologies have been developed to investigate the deformation and damage mechanism of various structural materials at different length scale and under extreme loading conditions, and also to provide insights in the development of high-performance materials.

In microscopic material behavior and failure modes, polycrystalline metals of interest include heterogeneous deformation field due to crystalline anisotropy, inter/intra grain or phase and grain boundary interactions. Crystal plasticity model is utilized to simulate microstructure based polycrystalline materials, and micro-deformation information, such as lattice strain evolution, can be captured based on crystal plasticity finite element modeling (CPFEM) in ABAQUS. The comparison of advanced experimental measurement and numerical simulation facilitates the understanding of the deformation and stress partitioning mechanisms in dual phase steel (DP980) and multilayered steel.

For corrosion or oxidation induced failure in high temperature alloys, a cohesive zone model (CZM) is introduced to describe the interfacial traction and separation behavior. By coupling diffusion process with CZM, impurity degradation effect at grain boundary can be studied to predict intergranular failure mechanism under corrosive environments. On the other hand, microscopic numerical methods are not efficient or applicable in the damage predictions for structural components. To this end, elastic perfect plastic (EPP) model has been proposed as an efficient tool to evaluate creep and fatigue damage for structural material (nickel based superalloy A617, SS316 etc.) at elevated temperatures. This methodology will be applied in numerous finite element simulations. By comparing

with simplified method test data, the feasibility of EPP methodology at elevated temperatures can be verified.

Table of Contents

List of Tables

List of Figures

Chapter 1 Introduction

The investigation of advanced structural materials has been motivated primarily due to the high demands from automotive, aerospace [1,2] and power industries [3] in order to improve reliabilities, duration and strength of engineer components. Aiming at reducing emission of greenhouse gas and increase energy efficiency, extreme environmental conditions, such as elevated temperature and high strength-weight ratio, are widely used for engineering applications. However, this poses grand challenges to in the study of next-generation workforce and development of next-generation energy materials. In order to improve the performance of advanced materials, numerous studies are concentrated on uncovering the deformation and damage mechanisms with the development of advanced measurement techniques and sophisticated numerical methods.

1.1. Numerical Methods at Mesoscale

Continuum crystal plasticity is introduced to provide a critical link from microstructures to overall mechanical behavior which is known as mesoscale study [4], even though the crystal plasticity theory is greatly phenomenological [5]. The concept of mesoscale modeling is presented to connect the studies between the length scale of atom and continuum [6] which can take both microscopic and macroscopic properties into the model, the smallest of which is the length scale over which electronic structure is accounted for (up to $\sim 10^3$ atoms), and largest being the continuum which is the domain of engineering. The studies at mesoscale are governed by a complicated interaction between atoms, microstructures in a microscopic level and also by the large scale structural behavior [5].

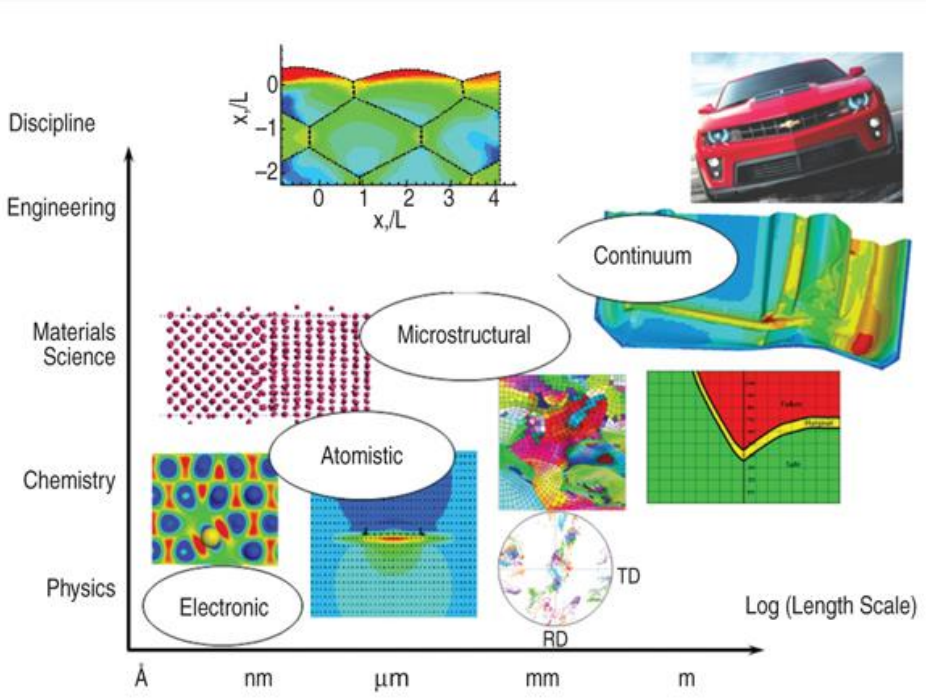

Figure 1.1 Schematic illustration of the simulation techniques performed at different length scales [6].

Intergranular stress/strain fields appear in polycrystalline metals due to the deformation heterogeneity in individual grains or from the neighboring grains. This can have significant effects on overall localized material mechanical properties. Theoretically, the above microstructure-related information could be captured at the grain by modeling a polycrystalline structure with grain presented explicitly with slip based crystal plasticity constitutive law attributed to. As shown in Fig. 1.2, the total deformation can be decomposed into plastic part, induced by material plastic flow on activated slip system, and elastic part induced by lattice stretching and rotation.

The development of plasticity models always relies on a comparison with experimental measurements such as hardness, stress-strain curves or other macroscopic measurements. With the development of new measurement technologies, the deformation and damage under an intermediate level are uncovered. Provided with the advanced testing observations, the development of predictive plasticity theories has been progressed forward, which leads to a new view of scientific research on material studies.

1.2. Experimental motivations

With the establishment of many user-friendly facilities worldwide by the aid of advanced technologies, neutron and synchrotron X-ray diffraction techniques have attracted numerous attentions from multi-disciplines with its non-destructive and deep penetration features.

Because of the deep penetration capability of neutron beams, neutron diffraction allows bulk measurements with a typical spatial resolution in the order of millimeters. Recently neutron diffraction and high-energy XRD techniques have been widely used to

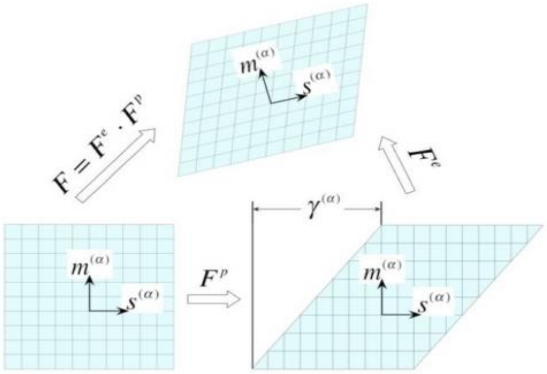

Figure 1.2 Deformation component of slipped based crystal plasticity. The total deformation can be decomposed into plastic part and elastic part.

study the effects of material microstructure, thermo-mechanical loading conditions, and environment, among many others on the deformation and failure behavior of polycrystals [4,7 – 11]. From the diffraction measurement, the lattice strain can be recorded from the shift of the diffraction peaks, thus corresponding to the elastic lattice distortion of the grains that satisfy the diffraction conditions. Two example plots are illustrated for multiphase steel lattice strain measurements under tensile test in Fig. 1.3. The lattice strain relies on the intergranular interactions of the inhomogeneous deformation fields in neighboring grains Fig. 1.4 schematically represents the strain measurement by neutron diffraction in two different directions: axial (in-plane) and transverse (through thickness) of specimen. The incident neutron beam impinges on the sample with an angle rotated from the loading axis and is scattered onto two detector banks situated at relative to the incident beam. It is believed that the heterogeneous stress and strain developed in a polycrystalline material is critical for the crack initiation [12] because the residual stress combined with the applied stress or together with some unknown defects or poor microstructures can somehow lower the critical stress when failure occurs.

1.3. Corrosion assisted intergranular crack in polycrystalline materials

High temperature gas-cooled reactor design (HTGR) has been proposed and studied to improve the energy efficiency of new designed power plant and gas turbine [3]. The U.S. Department of Energy has granted the study of HTGR for the Next Generation Nuclear Plant (NGNP) Demonstration Project. However, despite the severe creep damage at elevated temperatures, due to the thermal activation, environmental impurities like oxygen and hydrogen atoms can have higher diffusivity resulting in deeper corrosive

(a)

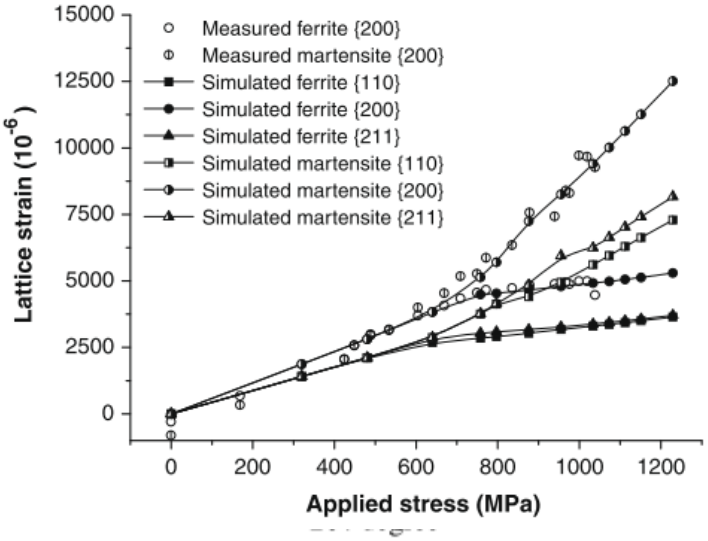

(b)

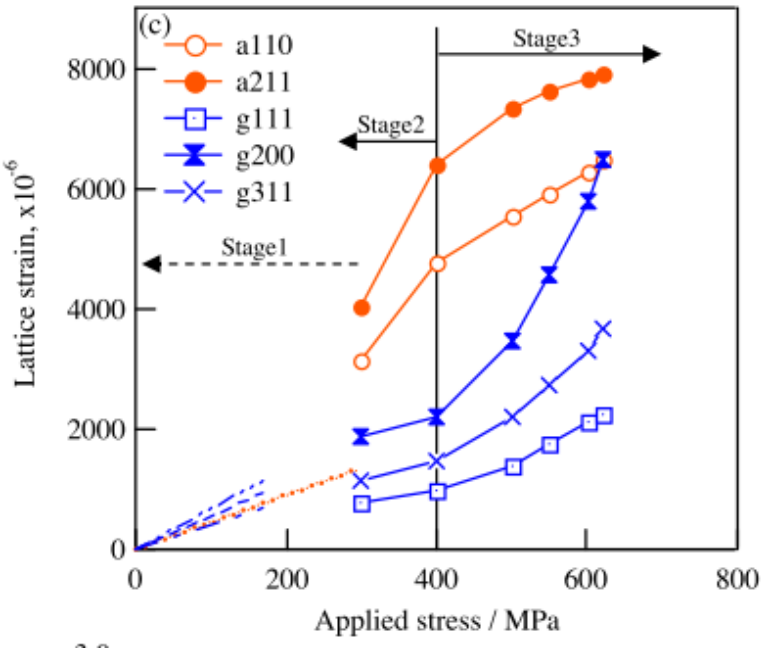

Figure 1.3 Response of lattice strains along the tensile axis for different reflections of (a) DP 980 [2] and (b) multilayered steel [13]

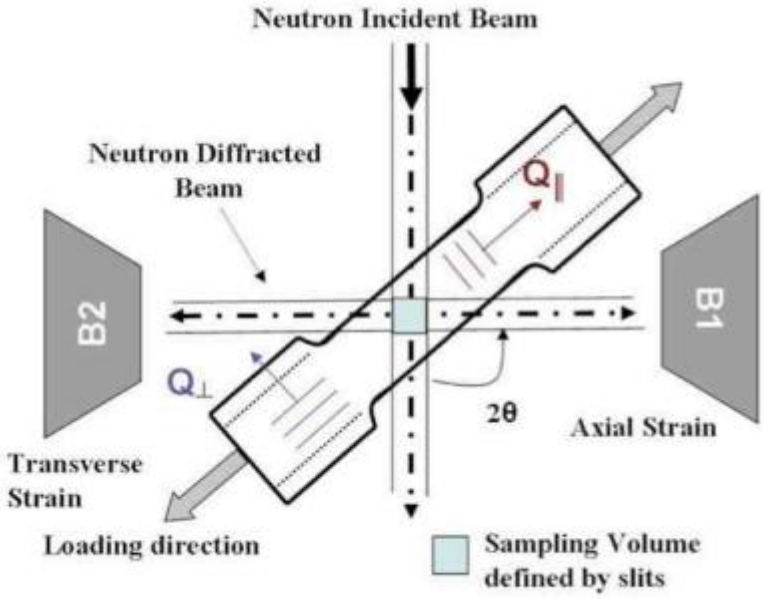

Figure 1.4 Schematic representation of the strain measurement by neutron diffraction technique in two different directions: axial (in-plane) and transverse (through thickness) of specimen [14]

penetration in structural components than normal temperature. Corrosion damage will lead to degradation of material mechanical properties in components, and such damage is demonstrated to be one of catastrophic damage factors in structural materials.

Nickel-based superalloy A617 (53.5% Ni, 21.9% Cr, 11.4% Co, 9.78% Mo, 1.69% Fe, 0.96% Al, and other elements) is a promising candidate material for the HTGR because of its high strength and high temperature sustainability. Numerous experimental studies have been conducted concerning the damage mechanism of A617. Oxidation induced intergranular cracking has attracted researcher's interests since the oxidation layer can be observed at both sample surface and interiors as shown in Fig. 1.5 (a). The oxidation can cause the degradation of grain boundary interfacial strength and grain interior strength, which is considered as fracture mechanism of A617 at elevated temperatures.

While diffused impurities can affect material properties, mechanical responds also play a significant role in the diffusion induced corrosion process [15–20]. Moreover, because of heterogeneity of microstructure in polycrystalline materials, the stress field can either enhance or suppress impurity diffusion. As a result, impurities can aggregate at some grain junction points inducing a severer localized degradation of material properties. Since the localized inelastic heterogeneous deformation has been widely regarded as an important cause of structural local failure, the aggregation of impurities can deteriorate material performance leading to micro-scale fracture at grain boundaries thus resulting in sudden failure of structural components.

Due to practical restrictions, experimental measurement of diffusivity and impurity concentration still remain unclear. Moreover, diffusion in polycrystalline

(a)

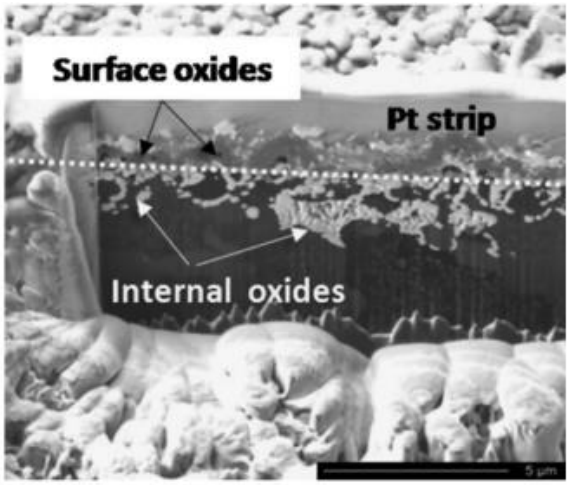

(b)

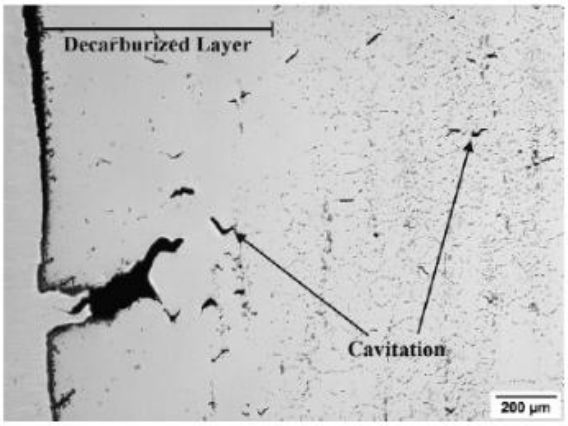

Figure 1.5 Both surface oxides and internal oxides can be observed in A617 [21].

materials requires time consuming experiments and high safety testing environment [18]. As a result, a feasible computational approach that studies stress-coupled diffusion with considering microstructure heterogeneity is greatly required to study corrosion effects in materials microscopic failures.

1.4. Elastic perfect plastic methodology in the evaluation of creep-fatigue damage

In current AMSE Code (Subsection NH), the rules of evaluating creep fatigue damage is not applicable for material at elevated materials, such as A617 above 650℃. Because at high temperatures, it is difficult to decouple plasticity and creep-induced inelasticity, which is the basic procedure in current evaluation methods, a simplified method based on EPP model is adopted to resolve these difficulties[22,23].

Numerous experiments are conducted in to evaluate the creep fatigue damage to support EPP methodology verification [24,25]. One of experimental methods is the simplified model test (SMT) approach based on an elastic follow-up characterization of stress and strain redistribution due to creep. The SMT geometric design is shown in Fig. 1.6 (a) and testing system in Fig. 1.6(b). An end displacement is applied at one specimen end and displacement profile in one loading cycle is as descried in Fig. 1.6(c). One failed SMT specimens is shown in Fig. 1.6(d).

1.5. Outline of this dissertation

Based on above discussion, this dissertation is organized as follows. In Chapter 2, we will use crystal plasticity model to simulate the lattice strain evolution in dual-phase and multi-layered steels and compare it with diffraction measurement data. With the correlation, we will discuss the stress partitioning mechanism in the multiphase steels. In Chapter 3, a diffusion coupled cohesive zone model will be introduced to study

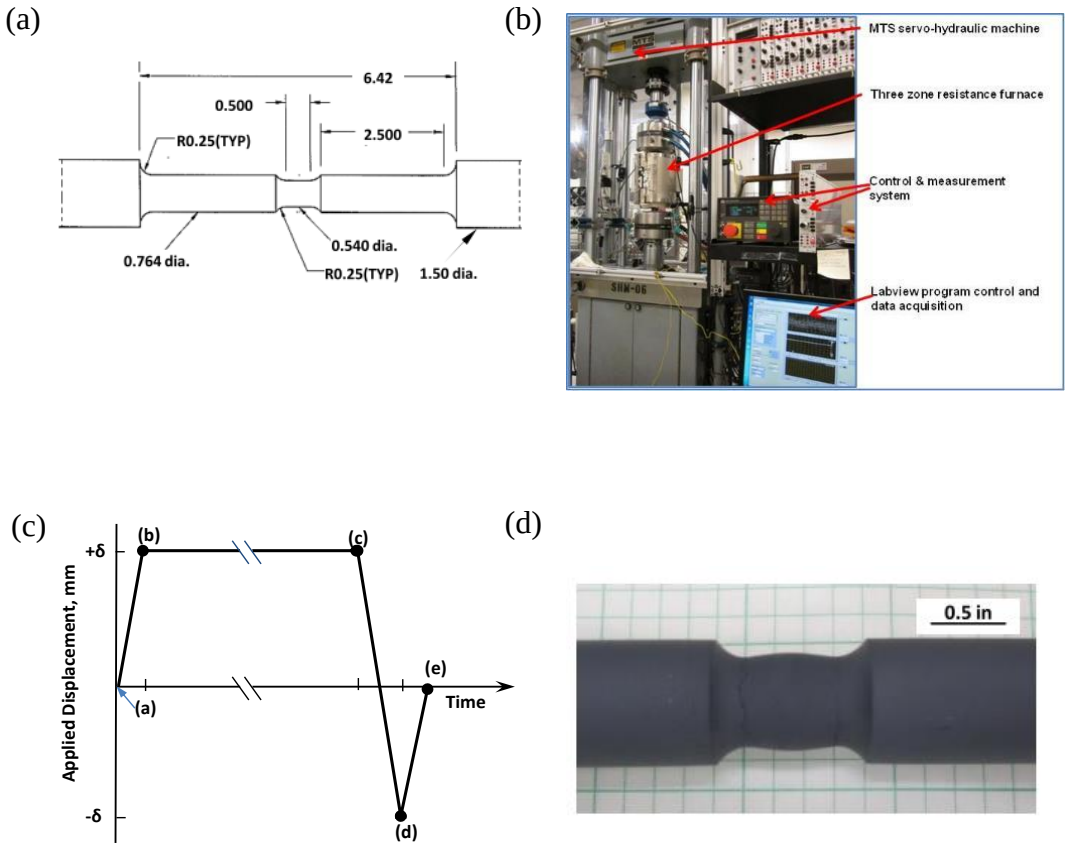

Figure 1.6 (a) Design figure of SMT test specimen. (b) SMT testing system (c) Applied displacement profile in one loading cycle. (d) Failed specimen of SMT geometry

intergranular fracture mechanism under corrosive environment. In next section, the EPP creep-fatigue methodology will be introduced and the conservation of proposed method will be demonstrated. Additionally, the application of computational tools in practical application and experimental design will be introduced, and the development of utility to expand the feasibility of FEA simulation is discussed in Chapter 5.

Chapter 2 Crystal Plasticity Analysis of Stress Partitioning Mechanisms and their Microstructural Dependence in Advanced Steels

2.1. Introduction

Demands from automotive and aerospace industries have stimulated the investigations of multi-phase steels that can achieve both high strength and high ductility and thus have tremendous applications in vehicle and aircraft body structures. In advanced high strength steels (AHSS) [26] that are broadly used in these applications, two phases are introduced, including a hard phase that provides high strength and the other phase that is capable of large elongation prior to failure. As a result of complex intergranular and interphase interactions, a good balance of strength and elongation strain can be achieved. One example is the dual phase (DP) steel, consisting of low carbon, hard martensite phase (about 5-30 vol. %) dispersed in the ferrite matrix [1,2,27]. An alternative design beyond AHSS is the multilayered steel as processed by rolling bonding of stacked, alternating martensite and austenite layers [13,26,28]. On the so-called "banana curves" plotting the tensile strength against fracture elongation (i.e., a ductility measure) in [26], DP steel shows a better combination of strength and ductility than conventional steels. However, the multilayered steel has the potential to even outperform than the dual phase steel as shown in [26]and as reviewed in [28].

Provided with strong interfaces between the constituent phases, the failure strain in the brittle martensite phase will be delayed by the surrounding geometric constraints, while the rule of mixture will dictate a large strength of the composite. To this end, the microstructural design is imperative especially in terms of the stress partitioning mechanisms amongst the constituent phases. In recent works [2,13], advanced diffraction

measurements were conducted on both types of multi-phase steels under tensile tests. Advanced diffraction measurements provide an in situ, nondestructive and deep-penetrating method to capture the evolution of grain-level and phase-level deformation behavior. Lattice strain evolution in DP 980 steel (68 vol. % ferrite and 32 vol. % martensite) was collected using high energy X-ray diffraction (HEXRD) [2]. Neutron diffraction measurements were conducted in [13] on multilayered steel with alternating martensitic and austenitic layers. The objective of these diffraction studies is to investigate the stress partitioning mechanism between the two constituent phases, but the direct information from these measurements, being the lattice strain evolution, has a complex convolution of intergranular and interphase interactions. Considering a single-phase polycrystal material, we can see that the *hkl* diffraction peaks will be governed by a number of grains whose {*hkl*} planes satisfying the diffraction condition. The peak shift will give rise to the lattice strain, and microscopically this is a result of the lattice stretching of these {*hkl*} planes in the chosen grain family. Some grain families will yield before others, and the yield sequence is determined by the intergranular interaction. With the presence of two phases, the respective yield sequences of {*hkl*} grain families in these two phases will be further complicated by the interphase interaction.

The understanding of the lattice strain evolution in these mutli-phase steels can be obtained by numerical simulations. For instance, an elasto-plastic model is adopted in [29] to investigate the macroscopic hardening behavior by using a modified Swift equation describing the stress-strain relationship. Such a model, however, does not have a direct reference to the inhomogeneous deformation fields on gain levels. On the other hand, lattice strains can be successfully investigated by microstructure-dependent analysis, such

as the crystal plasticity finite element method (CPFEM) [7,9,30], and visco-plastic self-consistent (VPSC) method [2,31,32] for both FCC and BCC materials. In the VPSC model, each grain is assumed to be embedded in a homogeneous matrix, of which the material properties obey the macroscopic deformation properties. The consistency condition is derived from the fundamental Eshelby solution that determines the deformation fields induced by the inclusion or inhomogeneity. Although efforts have been attempted to extend the VPSC model to multi-phase materials [2,32], important questions such as the interplay between intergranular and interphase deformation fields and the dependence of stress partitioning mechanisms on microstructural designs (i.e., dual phase as opposed to multilayers) cannot be clearly addressed. An explicit treatment of these material microstructures by CPFEM will be clearly more advantageous.

In this work, CPFEM simulations are conducted to investigate the stress partitioning amongst various grain families in both phases. A representative volume element (RVE) approach is used to describe the unique microstructures in DP 980 steel, and a full-scale model for the multilayered steel. Geometric input parameters include volume fraction, characteristic grain shape, and phase distributions as derived from the scanning electron microscopy (SEM) image in [2] for DP 980 steel and from optical images in [13] for the multilayered steel. By fitting to all the available {*hkl*} lattice strains from experimental observations, the crystal plasticity parameters can be determined. Three deformation stages can be identified, each of which exhibits microstructure-dependent intergranular and interphase characteristics. Our simulations will allow us to explore possible microstructure and material designs that can be used to tune the stress partitioning, the study of which will help understand and possibly delay the localized failures in these materials.

2.2. Numerical Model Description

An RVE model containing two phases is constructed for DP steel simulation in Fig. 2.1. The entire model is of $100\mu m \times 100\mu m \times 100\mu m$ in dimension, and is made of $10 \times 10 \times 10$ cubic units. Note that during the annealing process, the austenitic grains are nucleated randomly at the ferritic grain boundaries, and then they grow the fastest along the grain boundaries. After further cooling, prior austenitic grains are transformed into martensite, and this thermal treatment history determines the shape and locations of martensite phase. A numerical method simulating the above process is introduced in [33] and implemented to simulate the microstructural evolution in DP steel in [1]. Here a simplified model is used in our simulation that captures the essential microstructural features in DP steel. The cubic unit in Fig. 2.1(a) is composed of one martensitic grain and one ferritic grain, and the martensite phase is aligned along the grain boundaries, as shown in the cubic unit in Fig. 2.1(b). That is, it is placed randomly on one of the six surfaces of the cubic unit. A total of $3 \times 3 \times 3$ cubic elements (C3D8 – three dimensional 8-node continuum element in ABAQUS finite element software) are used to represent this martensite and austenite duo. As compared to the mesh in [13], the simplification lies on the use of cubic elements. Since lattice strains are based a statistical average of many grains, this simplification has been proved to be effective and computationally less intensive [8-10]. To satisfy the volume fraction of martensitic phase (Table 2.1), the martensitic phase has $3 \times 3 \times 1$ cubic elements. A two-dimensional view of the mesh in Fig. 2.1(b) exhibits similar phase patterns as in SEM images. These grains will be assigned with random crystallographic orientations. The faces of RVE model with normal directions of $-x$, $-y$ and

Table 2.1 The volume fractions of constituent phases in DP 980 steel.

Material	Ferrite Phase (vol. %)	Martensite Phase (vol. %)
DP 980 steel	68	32

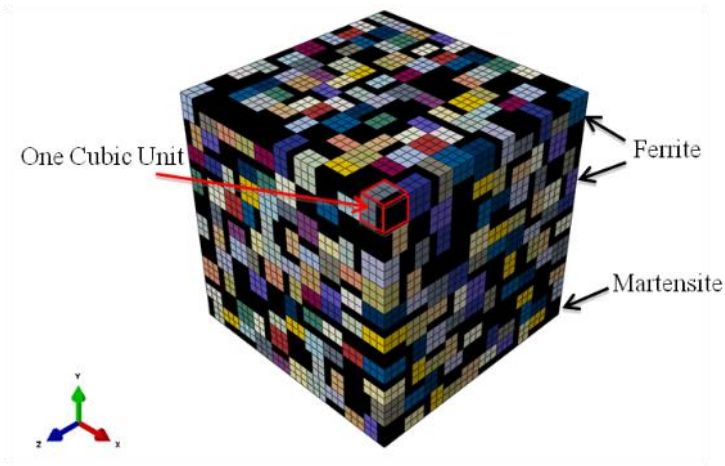

(a)

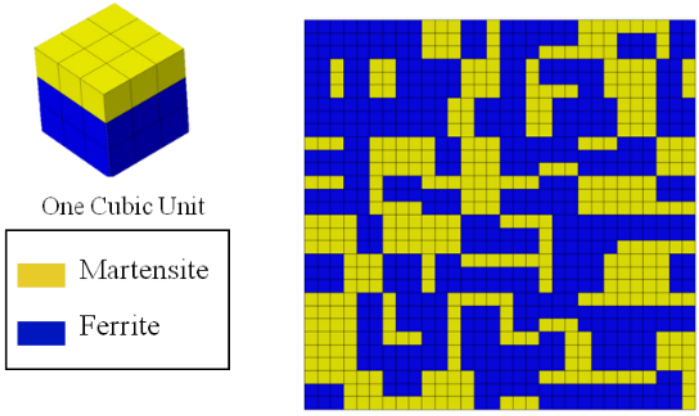

(b)

Figure 2.1 (a) Representative volume element (RVE) for DP 980 steel. The RVE model size is $100\mu m \times 100\mu m \times 100\mu m$ consisting of $10 \times 10 \times 10$ cubic units. Black elements denote the martensitic phase, while colored elements correspond to ferritic grains. (b) Each cubic unit consists of $3 \times 3 \times 3$ C3D8 solid elements including one martensite grain and one ferritic grain. Due to the martensitic phase transformation during annealing, these martensitic phases are located at the grain boundaries. A two-dimensional cut of the RVE mesh is shown to compare with the SEM image in [2].

–*z* as shown in Fig. 2.1(a) are prescribed with the symmetric boundary conditions. A ramping displacement with a constant rate is applied on the surface with *z* normal direction. The diffraction vector is parallel with the loading direction that is the *z* direction in Fig. 2.1(a).

As described by the detailed manufacturing procedure in [13], the multilayered steel is manufactured by hot-rolling low-carbon martensitic steel layer and austenitic stainless steel layers. The full-scale model sketched in Fig. 2.2 simulates a three-layer sample, whereas the layer thickness and volume fraction are derived from optical observations in [5] (Table 2.2). From symmetric conditions, only one eighth of the full model is meshed in our simulations, leading to a body of $250\mu m \times 250\mu m \times 500\mu m$ containing $25 \times 25 \times 50$ C3D8 cubic elements, where each cubic element represents one grain. According to the SEM image in [34] and transmission electron microscopy (TEM) image in [35], the average grain size of WT780C martensitic phase is about $11.1\mu m$ and that of SS316L austenitic phase is about $10\mu m$. Thus our simulations do not distinguish this slight difference in grain size. Again these grains and phases are assigned with random crystallographic orientations without considering the texture effect. As sketched in Fig. 2.2, the symmetric planes are applied with symmetric boundary conditions, while a ramping displacement is applied in parallel to the layer interface direction in the numerical model. The diffraction vector is also parallel with the loading direction.

The CPFEM simulation is based on the classic crystal plasticity theory in Peirce et al. [5], and the ABAQUS user defined subroutine (UMAT) by Huang [11]. The UMAT has been modified by Zheng et al. [4] in order to investigate the lattice strain evolution in a polycrystal aggregate.

Table 2.2 Parameters used in the three-layer model in Fig. 2.2 for the multilayered steel.

Material	Austenite layer thickness (mm)	Martensite layer thickness (mm)	Martensite Phase Volume fraction
Multilayered Steel	0.4	0.2	20%

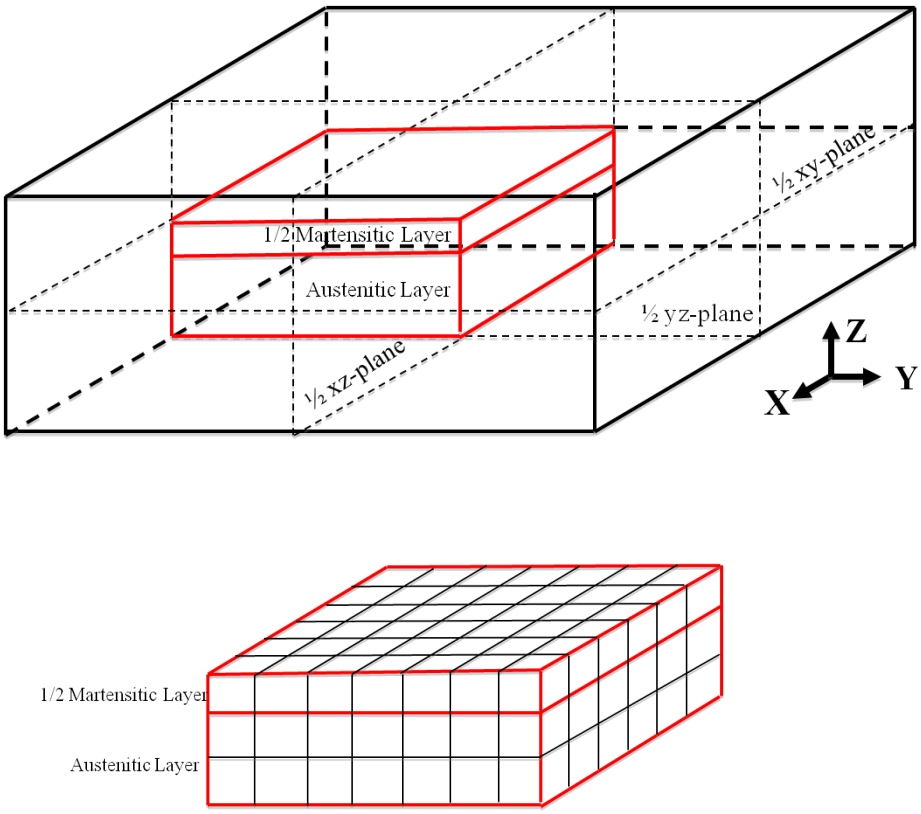

Figure 2.2 Schematic illustration of CPFEM model of multilayered steel. One eighth of the model is meshed due to symmetric considerations.

Here a concise review of the CPFEM is given below. For the Schmid-type crystal plasticity, the plastic deformation rate is regarded as a summation over all slip systems,

$$\dot{F}_{ik}^{p} F_{kj}^{p\,-1} = \sum_{\alpha=1}^{N_{slip}} \dot{\gamma}^{(\alpha)} s_i^{(\alpha)} m_j^{(\alpha)} \tag{2.1}$$

where N_{slip} denotes the total number all activated slip directions, $\dot{\gamma}^{(\alpha)}$ is the slip rate of the α-th slip system, $s_i^{(\alpha)}$ and $m_j^{(\alpha)}$ represent the slip direction and slip plane normal, and F_{kj}^{p} is the plastic deformation gradient. The slip rate updates according to the power-law flow rule,

$$\dot{\gamma}^{(\alpha)} = \dot{\gamma}_0 \left| \frac{\tau^{(\alpha)}}{\tau_{flow}^{(\alpha)}} \right|^n \operatorname{sgn}\left(\tau^{(\alpha)}\right) \tag{2.2}$$

where $\dot{\gamma}_0$ is the reference strain rate, $\tau^{(\alpha)}$ and $\tau_{flow}^{(\alpha)}$ are the resolved shear stress and current slip strength of the α-th slip system respectively, and n is the stress exponent. The hardening behavior of $\tau_{flow}^{(\alpha)}$ is described by the Peirce-Asaro-Needleman model,

$$\dot{\tau}_{flow}^{(\alpha)} = \sum_{\beta} h_{\alpha\beta} \left| \dot{\gamma}^{(\beta)} \right| \tag{2.3}$$

where $h_{\alpha\beta}$ is the hardening moduli. The self-hardening modulus is expressed as,

$$h_{\alpha\alpha} = h(\gamma) = h_0 \operatorname{sech}^2 \left| \frac{h_0 \gamma}{\tau_s - \tau_0} \right| \tag{2.4}$$

where no summation is assumed for the repeated index α, h_0 is the initial hardening modulus, τ_0 is the initial slip strength, and τ_s is the saturation slip strength. And the latent hardening part is given by

$$h_{\alpha\beta} = h(\gamma)\left[q + (1-q)\delta_{\alpha\beta}\right] \tag{2.5}$$

where $\alpha \neq \beta$, and q is the latent hardening coefficient.

Among all the grains, we choose the ones whose {*hkl*} planes satisfy the diffraction condition. That is, their <*hkl*> directions are parallel to the diffraction vector. In practice, we allow a small tolerance of $\pm 5^{\circ}$ between these two vectors in order to obtain sufficient fraction of grains. Then the lattice strain, ε_{hkl}, is evaluated by

$$\varepsilon_{hkl} = \frac{\sum_{N=1}^{N_{\text{grain}}} \int \varepsilon_{ij}^{\text{elastic}} q_i q_j d\Omega_N}{\sum_{N=1}^{N_{\text{grain}}} \int d\Omega_N} \tag{2.6}$$

where N_{grain} denotes the number of grains whose direction is within $\pm 5^{\circ}$ with respect to diffraction vector, q_i is the component of diffraction vector, $\varepsilon_{ij}^{\text{elastic}}$ is the Lagrange-Green strain,

$$\varepsilon_{ij}^{e} = \frac{1}{2}\left(F_{ik}^{e} F_{kj}^{e} - \delta_{ij}\right) \tag{2.7}$$

and F_{ij}^{e} is the elastic deformation gradient.

2.3. Lattice strain evolution

Before presenting our simulation results, a mechanistic interpretation of the lattice strain is briefly given for a single-phase polycrystal. According to the work in [30], lattice strain partitioning, or splitting, in individual grain families indicate a sequence of yielding in these families. Consider a simple view in which every grain is subjected to the same strain as the macroscopic one, i.e., the Taylor iso-strain model. The first gain family to reach yield is the one that has the lowest yield strain, whereas the yield strain is inversely proportional to the product of Schmid factor and directional modulus. Assuming no

hardening, the grain family upon yielding will not have further elastic deformation, so its lattice strain will remain constant with respect to the further increase of the applied stress. Correspondingly, a larger portion of the applied stress will be supported by the grain families that have not reached yield, and the lattice strains of these grain families will increase rapidly. The yield sequence, $\{hkl\}_1 \rightarrow \{hkl\}_2 \rightarrow \ldots \rightarrow \{hkl\}_N$, will thus govern the lattice strain splitting on the lattice strain versus applied stress plots. This is denoted as intergranular interaction in this study. This simple view can be generalized to the two-phase polycrystal, and we will see the interactions of two yield sequences, i.e., $\{hkl\}_1^{\text{phase I}} \rightarrow \{hkl\}_2^{\text{phase I}} \rightarrow \ldots \rightarrow \{hkl\}_N^{\text{phase I}}$, and $\{hkl\}_1^{\text{phase II}} \rightarrow \{hkl\}_2^{\text{phase II}} \rightarrow \ldots \rightarrow \{hkl\}_N^{\text{phase II}}$. These two sequences may be very likely intertwined; equivalently speaking, we may not be able to separate the intergranular and interphase interactions.

As described in introduction, HEXRD and neutron diffraction measurements were carried out to obtain the lattice strain evolution of different $\{hkl\}$s for both phases in DP 980 steel and multilayered steel under uniaxial tensile test. These experimental data are given in discrete markers in Figs. 2.3 and 2.4, while our simulations are given in solid curves. The mechanistic understanding in the preceding paragraph will help us determine the CPFEM constitutive parameters (see Tables 2.3 and 2.4). The elastic constants, C_{11}, C_{12} and C_{44}, can be found in literature such as [2], and our simulations will further fine-tune these values so as to fit the initial lattice strains when all grains and phases are in elastic deformation. Note that the initial lattice strain splitting is primarily determined by the Schmid factor (which is governed by the choice of slip system) and the directional modulus (which is governed by the elastic anisotropy). The slip system is chosen as the

Table 2.3 CPFEM parameters for the DP 980 steel.

Phase	C_{11} (GPa)	C_{12} (GPa)	C_{44} (GPa)	n	h_0	τ_0	τ_s	q
Ferrite	237	141	116	10	800	200	800	1
Martensite	237	141	116	10	1000	550	1000	1

Table 2.4 CPFEM parameters for the austenite/martensite multilayered steel.

Phase	C_{11} (GPa)	C_{12} (GPa)	C_{44} (GPa)	n	h	τ_0	τ_s	q
Austenite	204.6	137.7	126.2	10	400	65	180	1
Martensite	268	110	78	10	300	290	2000	1

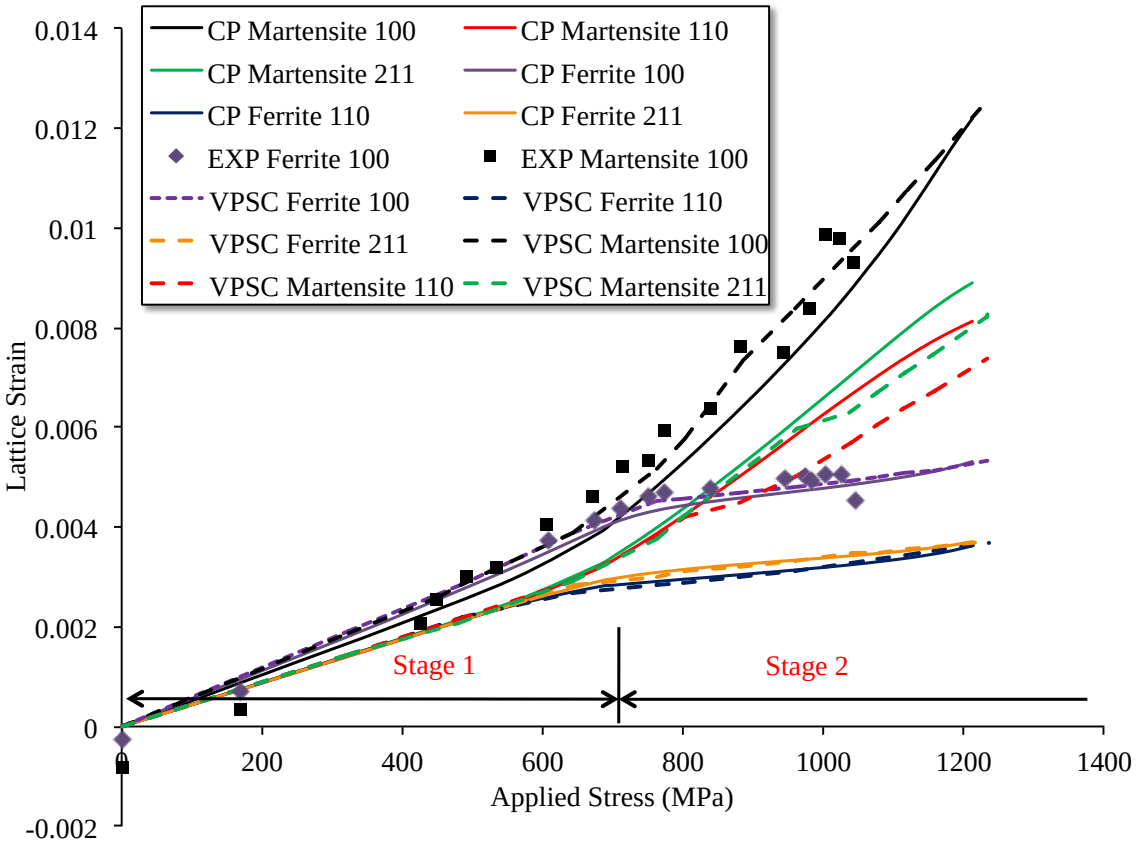

Figure 2.3 Crystal plasticity finite element simulations of lattice strain evolution in DP 980 steel (solid lines), as compared to experimental data (discrete markers [4]) and viscoplastic self-consistent simulations (dash curves).

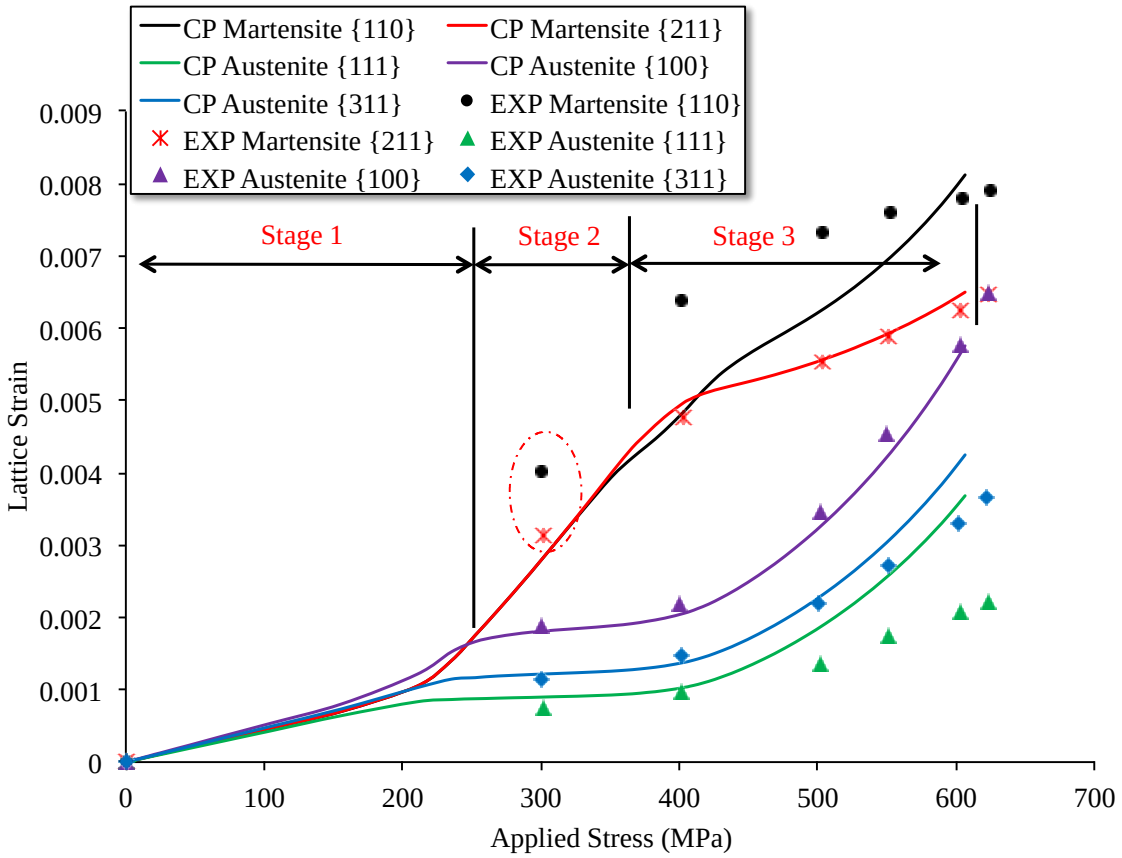

Figure 2.4 Lattice strain evolution in multilayered steel, with the comparisons of CPFEM simulations in this work and experimental data in [13]. A red dashed ellipse indicates the deviation of modeling from experimental data.

{110}<111> system for both ferrite and martensite phase, and as the {111}<110> for austenite. The initial slip strength, τ_0, can be estimated from the deviation of the lattice strain from linearity as the applied stress increases and exceeds the elastic stage, being about 700MPa in Fig. 2.3 and about 250MPa in Fig. 2.4. In single-phase polycrystals, τ_0 relates to the macroscopic yield stress by the Taylor factor, being about 3.0 for non-textured FCC and BCC polycrystal. This is how we estimate τ_0 for the soft ferrite and austenite phases in Tables 2.3 and 2.4. However, the Taylor-factor approach cannot be applied to estimate the initial slip strength in martensite phase. When the martensite phase yields, some grain families in ferrite or austenite phases have already reached yield but some have not. Therefore the slip strength of the martensite phase is obtained by fitting to the experiments in [4] and [5]. Also the hardening parameters as specified in Eqs. (2.3)-(2.5) are obtained from fitting the entire lattice strain curves for all these phases.

2.3.1 Intergranular versus interphase interactions

Experiments and simulations are presented for DP 980 steel in Fig. 2.3. Because the ferrite and martensite phases have similar lattice structure and constants, the diffraction peaks are convoluted, and only the {200} peaks have been separated in [2]. Thus experimental data are only given for {200} lattice strains for the constituent phases. For the other lattice strains, our CPFEM results are compared to the VPSC model presented in [2]. Results for the austenite/martensite multilayered steel only compare CPFEM results to the neutron diffraction measurements in Fig. 2.4. VPSC model was not attempted because the unique microstructure in multilayered steel differs from typical polycrystalline aggregates.

The lattice strain evolution can be categorized into several stages. At low applied stresses, all grain families and phases deform elastically, and the initial slopes in this Stage

1 are governed by the elastic constants and microstructure. Note that the martensite phase is much harder than the other ferrite or austenite phase. Therefore, we denote a Stage 2 in which none of the grain families in martensite phase yields. In Fig. 2.3, this corresponds to the applied stress in the range of about 600 MPa to 1200 MPa, while in Fig. 2.4 in the range of about 250 MPa to 380 MPa. Since the martensite phase deforms elastically in Stage 2, the ratios of the various {*hkl*} lattice strain slopes for this phase should remain roughly unchanged. The lattice strain curves for the soft phase in this stage, although all moving horizontally together, will branch in Fig. 2.3 and Fig. 2.4 because the applied stress is shifted among these grain families. With the further increase of the applied stress, some grain families in the martensite phase will yield, leading to the Stage 3. Because of the low applied stress in Fig. 2.3, Stage 3 is not observed, but our simulations in Fig. 2.5 suggest that eventually it will take place. In Stage 3, the start of the yield sequence in the martensite phase, $\{hkl\}_1^{\text{martensite}} \rightarrow \{hkl\}_2^{\text{martensite}} \rightarrow \ldots \rightarrow \{hkl\}_N^{\text{martensite}}$, falls into the middle place of the yield sequence of the soft phase, $\{hkl\}_1^{\text{ferrite/austenite}} \rightarrow \{hkl\}_2^{\text{ferrite/austenite}} \rightarrow \ldots \rightarrow \{hkl\}_N^{\text{ferrite/austenite}}$. Additionally, the hardening rates of these two phases are different in this stage. Therefore, it is observed that the lattice strain slopes of martensite phase decrease while those of austenite phase increase in Stage 3 of Fig. 2.4.

In Fig. 2.4, some discrepancies are observed for martensitic {110} lattice strain between CPFEM simulations and experiments, as marked by the dashed ellipse. This is likely due to the simplified microstructure in Fig. 2.2, while the actual microstructure has a transition of grain sizes from the interface and there are some correlations of crystallographic orientations in the grains adjacent to the interface. Also the actual grain shape in martensite phase is of lathe like.

2.3.2 Effectiveness of stress transfer amongst phases and grain families

Although both DP and multilayered steels have similar stress partitioning/transferring behavior, the multilayered steel is found to be much more superior in terms of the improved failure strain. Such a difference can be understood from the dependence of Stage 2 and Stage 3 on the composite microstructure. From a geometric point of view, the deformation field in the multilayered steel can be approximated by the iso-strain model, while that in the DP steel lies between the iso-strain and iso-stress models. That is, each grain or phase in DP steel is subjected to a complex constraint from the neighboring grains or phases, and the deformation field, although being close to the iso-strain model, can be nicely described by the self-consistent model. In the iso-strain case, the applied stress will be shift from the phase/grain with low yield strain to that with high yield strain, and such an "effectiveness" of stress transfer is more obvious than the iso-stress model or the self-consistent model. Previously in [13], an iso-strain assumption is introduced to evaluate the stress transfer behavior in these two types of different steels. However, in this simple model, the soft phase is assumed to not bear the applied stress after it yields. The work in [13] further compares the measurements in Fig. 2.3 and Fig. 2.4, which are clearly for different types of soft phase and different volume fraction. Moreover, the iso-strain assumption neglects the intergranular interactions due to the inhomogeneous deformation fields. In contrast, here we present CPFEM simulations to quantitatively evaluate the effectiveness of stress transfer in these two types of composite microstructures.

To demonstrate that the effectiveness of stress transfer is higher in multilayered steel, we construct a fictitious DP model with martensite and austenite phases. As shown in Fig. 2.5(a), the cubic unit in this modified DP model consists of 22 vol. % martensite

(a)

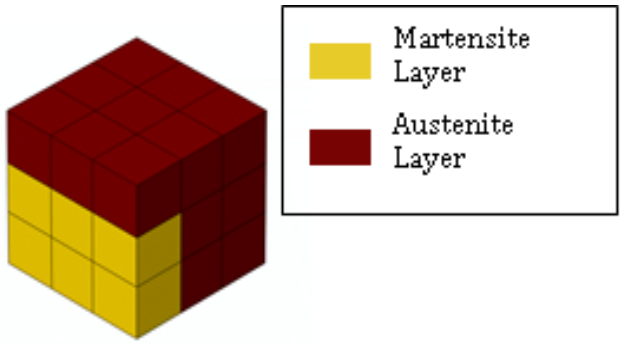

(b)

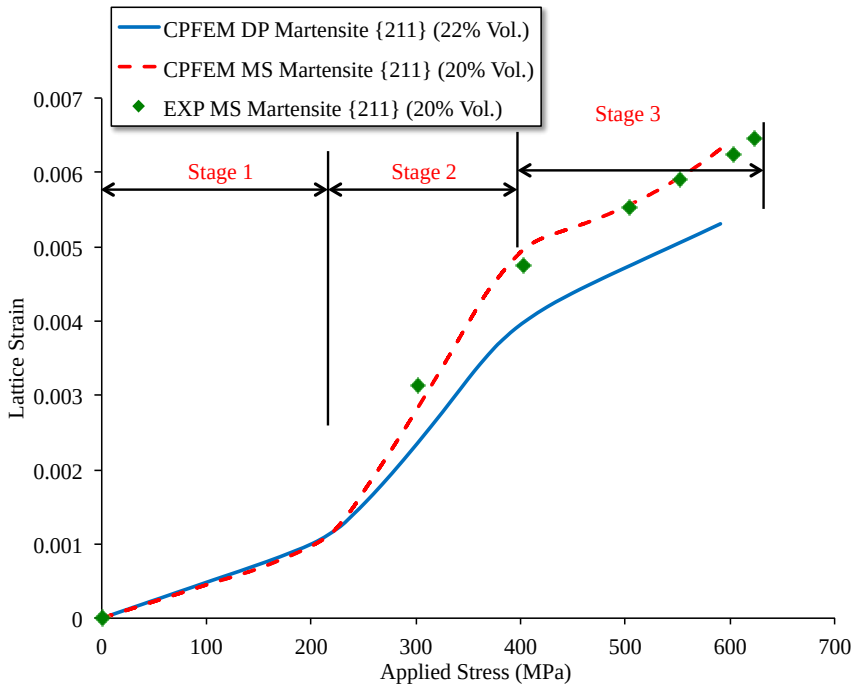

Figure 2.5 (a) Schematic illustration of the cubic unit used in the fictitious DP material that consists of martensite and austenite phases. (b) Direct comparisons of {211} lattice strain evolution in the fictitious DP material and multilayered steel of martensite and austenite phases.

and 78 vol. % austenite, which is consistent with the volume fractions in the multilayered steel. The entire RVE model contains $10 \times 10 \times 10$ of such cubic units with randomly assigned crystallographic orientations for both phases. The {211} lattice strains are given for the martensite phase in the fictitious DP model and the multilayered steel in Fig. 2.5(b). The general features in the three stages remain the same, while the magnitude of the martensite lattice strain is significantly higher in the multilayered steel, implying that a larger portion of the applied stress will be transferred to the hard phase. For instance, at an applied stress of about 420 MPa, the increase of lattice strain from fictitious DP to multilayered model is about 0.15%, corresponding to an extra stress of about 200 MPa on this grain family. In spite of the improved the effectiveness of stress transfer in multilayered steel, the microstructure will unavoidably make the inelastic deformation anisotropic if loading in different directions. All the lattice strains in the work are reported for the loading direction, and it is anticipated that the lattice strains in the transverse directions will be lower for the martensite phase in multilayered steel than those for the DP model.

The stress partitioning analysis will shed lights on understanding the superior elongation strain in the multilayered steel. For the multilayered steel, it has been found in [6] that the failure is preceded by a local debonding between austenite and martensite layers, and a slight necking and then brittle fracture in the debonded martensite. Debonding arises from the strain mismatch in the two phases, as evidenced in the synchrotron x-ray experiments in a composite consisting similar hard and soft phases [36]. In the multilayered steel, because of the improved lattice strain on the martensite phase as shown in Fig. 2.5(b), the mismatch of total strain between neighboring phases is significantly reduced. As a

consequence, the debonding and subsequent localized failure will be delayed, which help explain the improved macroscopic performance in such a material.

2.4. Summary

Intergranular and interphase interactions in DP steel and multilayered steel are investigated by crystal plasticity finite element simulations, with comparisons to the lattice strain measurements by advanced diffraction techniques in literature. Microstructural models are constructed from experimentally observed features such as the locations of martensite phase in DP steel. Three deformation stages are identified on the lattice strain evolution with respect to the applied stress. The yield sequences of various grain families in the two phases are found to be intertwined, leading to a complex interplay amongst the inhomogeneous deformation fields on grain and phase levels. The dependence of the effectiveness of stress transfer on the microstructure is investigated by the comparisons of a fictitious DP model (with austenite and martensite) and the multilayered steel. The enhanced stress transfer to the martensite phase will help delay localized failure such as martensite phase fracture and interface debonding.

Chapter 3 A Computational Approach to Study Corrosion Assisted Intergranular Crack in Polycrystalline Materials

3.1. Introduction

High temperature gas-cooled reactor design has been proposed and studied to improve the energy efficiency of new designed power plant and gas turbine [3]. However, due to the thermal activation, environmental impurities like oxygen and hydrogen atoms can have higher diffusivity resulting in deeper corrosive penetration in structural components than normal temperature. Corrosion damage can lead to degradation of material mechanical properties in components, and such damage is demonstrated to be one of catastrophic damage factors in structural materials. Impurity corrosion has been studied with a number of damage mechanisms, such as formation of external and internal brittle oxides, [21,37–40], hydrogen embrittlement [17,18,41–43] among many others.

While diffused impurities can affect material properties, mechanical responds also play a significant role in the diffusion induced corrosion process [15–20]. Moreover, because of heterogeneity of microstructure in polycrystalline materials, the stress field can either enhance or suppress impurity diffusion. As a result, impurities can aggregate at some grain junction points inducing a severer localized degradation of material properties. Since the localized inelastic heterogeneous deformation has been widely regarded as an important cause of structural local failure, the aggregation of impurities can deteriorate material performance leading to micro-scale fracture at grain boundaries thus resulting in sudden failure of structural components. Due to the technique restrictions, experimental measurement of diffusivity and impurity concentration still remain unclear. Moreover, diffusion in polycrystalline materials requires time consuming experiments and high safety

testing environment [18]. As a result, a feasible computational approach that studies stress-coupled diffusion with considering microstructure heterogeneity is greatly required to study corrosion effects in materials microscopic failures.

Even though the diffusivity of impurities increases at evaluated temperatures, the bulk diffusion is still trivial comparing to preferential path (such as grain boundary or crack path) diffusion except material surface. Numerous studies and models, i.e. Fisher's classical model [44] and Whipple's analytical model [45], etc. have been conducted to investigate the grain boundary diffusion, and these studies were reviewed by Herzig and Mishin [46]. It has been revealed the diffusivity of impurities at preferential path (grain boundary) can be several orders of magnitude, e.g., $10^5 \sim 10^8$, higher than the bulk diffusivity. Thus, the diffusion process in non-preferred part (like bulk or grains) is always neglected in the studies of corrosion assisted fracture [18,19,21]. Considering all above factors, a numerical finite element model coupled with cohesive zone model (CZM) and crystal plasticity finite element method (CPFEM) is proposed in this study.

Due to its simplicity and easy adaptability, CZM is widely employed to study the mechanical responds at material interfaces such as grain boundary interactions [47,48], crack growth [7,49] and micro-void growth [50]. In most recent studies, CZM strategy is applied in stress corrosion cracking simulations. Unlike sequentially coupled diffusion methods described in [21,38], concentration dependent CZM can ensure a fully couple of corrosion induced mechanical degradation by describing decohesion mechanism with impurity concentration together with stress driven diffusion. This coupled CZM approach is mainly applied in exploring the environment assisted crack growth considering impurities transport mainly along crack path in a macroscopic level currently. However,

many experimentalists observed intergranular crack initiation and growth deep inside the material [51], and these internal defects are induced by diffused oxygen corrosion through grain boundaries [52]. As a result, stress-coupled diffusion that takes microstructure heterogeneous deformation into consideration is an essential study to uncover corrosion assisted material damage mechanism.

In order to provide heterogeneous stress field for stress coupled diffusion simulations, CPFEM is adopted in this study. With strong capability of different boundary conditions, CPFEM model has successfully predicted grain-level deformations and explained microscopic mechanism in polycrystalline materials [8,9,11,53,54]. The plasticity anisotropic deformation can be determined by activated slip system, plastic flow rule and hardening law. Given different grain orientations, CPFEM offers an explicit treatment for microstructure-based simulations.

The objective of this study is to introduce a finite element simulation method to study fully stress-coupled diffusion and its effect on intergranular crack induced by grain boundary decohesion. The remainder of this paper is organized as follows: in section 2, diffusion coupled CZM model will be introduced. Adopted CPFEM model will be also briefly described in this section. In section 3, the numerical implementation of stress-coupled diffusion simulation will be presented including the method used to solve different boundary condition. To verify the accuracy and applications of proposed method, two example models will be illustrated. First model is comparing proposed numerical method with diffusion simulated with ABAQUS diffusion module under no external stress. The second example model couples CZM and CPFEM to study different damage mechanism

at different period. In last section, we will summarize the required technical improvements for future applications.

3.2. Stress-Coupled Diffusion Model and CPFEM

To study the corrosion assisted intergranular failure mechanism, an effective fully coupling method between impurity diffusion and crack growth is implemented in this study. ABAQUS introduces a sequentially coupling diffusion simulation module [55], and this method was widely adopted in studying material responds under environmental effects [21,39,56,57]. However, impurity concentration dependent degradation of material is not taken into consideration in the simulation of material mechanical response. Thus, fully coupled diffusion simulation is greatly required in corrosive fracture studies. Inspired by the method introduced by [18], a concentration dependent cohesive zone model is proposed and adopted to study the intergranular fracture mechanism.

By distributing initial orientation to each individual grain and introducing plasticity anisotropy, a Schmid-type crystal plasticity model has been widely implemented to study microstructural heterogeneity induced deformation mechanisms in polycrystalline material. A classic CPFEM model is adopted in this study to simulate the grain interiors and provide a heterogeneous stress field.

3.2.1 Stress-coupled diffusion equation

Based on different diffusion mechanisms, the governing equation describing impurity transporting in the materials can be slightly different by considering different affecting factors. Nevertheless, all types of diffusion equations are following Fick's first law stating diffusion flux being proportional to local density gradient. In this study, a general diffusion equation is adopted with stress gradient driven factor considered.

$$\mathbf{J} = -D(T)\cdot\left(\nabla c + k_p \nabla p\right), \tag{3.1}$$

where **J** is the diffusion flux, *D* is the diffusion coefficient of impurities as a function of the temperature, *c* is the impurity concentration, k_p is a factor that measures the stress effect, and *p* is the local pressure. In Eq. (3.1), the stress-coupled diffusion is evaluated by the pressure gradient thus treated as one driving force. Since only diffusion along grain boundary path is considered in studied CZM, the Eq. (3.1) will be expressed as one-dimensional form in later discussions. Considering mass conservation, the governing equation of stress-coupled diffusion can be expressed as,

$$\frac{\partial c}{\partial t} = D(T)\left(\nabla^2 c + k_p \nabla^2 p\right). \tag{3.2}$$

The terms including *p* in Eq. (3.1) and (3.2) bring the effect of pressure gradient into diffusion process. And stress gradient information will be evaluated through mechanical responds of CZM discussed in next subsection.

3.2.2 Cohesive interface model

A large number of constitutive CZM have been proposed to study relative motions and mechanical response of two contacting material surfaces. Different mechanisms are introduced to the framework to describe various interfacial properties and external loading conditions [58]. The constitutive equations relating the traction vector $\left(T_n, T_1, T_2\right)$ to the separation $\left(\Delta_n, \Delta_1, \Delta_2\right)$ is most conveniently characterized by a scalar interplanar potential $\Phi\left(\Delta_n, \Delta_1, \Delta_2\right)$,

$$T_n = \frac{\partial \Phi}{\partial \Delta_n},\ T_1 = \frac{\partial \Phi}{\partial \Delta_1},\ T_2 = \frac{\partial \Phi}{\partial \Delta_2}, \tag{3.3}$$

where subscripts, *n*,1,2, denote the normal and two tangential directions, respectively.

In our previous study[59], a reversible cohesive interface model was studied with introducing a viscosity-like parameter to avoid the convergence problem caused by snap-back instability in finite element calculations. In this proposed CZM, the form of separation potential Φ is based on theory proposed by Xu and Needleman [49] as follows,

$$\Phi\left(\Delta_n, \Delta_t\right) = \Phi_n - \Phi_n \exp\left(-\frac{\Delta_n}{\delta_n}\right)\left(1+\frac{\Delta_n}{\delta_n}\right)\exp\left(-\frac{\Delta_t^2}{\delta_t^2}\right). \tag{3.4}$$

Here $\Delta_t = \sqrt{\Delta_1^2 + \Delta_2^2}$, and δ_n and δ_t are characteristic lengths. As proposed by Gao and Bower [59], the viscosity included traction-separation relation for cohesive interfaces can be expressed as

$$T_n = \sigma_{\max} \frac{\Delta_n}{\delta_n} \exp\left(1 - \frac{\Delta_n}{\delta_n} - \frac{\Delta_t^2}{\delta_t^2}\right) + \zeta_n \frac{d}{dt}\left(\frac{\Delta_n}{\delta_n}\right), \tag{3.5}$$

$$T_t = 2\sigma_{\max}\left(\frac{\delta_n}{\delta_t}\right)\left(\frac{\Delta_t}{\delta_t}\right)\exp\left(1-\frac{\Delta_n}{\delta_n}-\frac{\Delta_t^2}{\delta_t^2}\right) + \zeta_t \frac{d}{dt}\left(\frac{\Delta_t}{\delta_t}\right), \tag{3.6}$$

where $\sigma_{\max} = \Phi_n \big/ \left(\delta_n \exp(1)\right)$ is identical to the maximum traction stress when the interface separation Δ_n is equal to characteristic normal separation δ_n with only normal loading applied on contacting interface. ζ_n and ζ_t are viscosity-like parameters that govern viscous energy dissipation under normal and tangential loading.

To take corrosion induced degradation effect into consideration, a concentration dependent traction separation law will be adopted in Eq. (3.5) and Eq. (3.6). It has been recognized that the impurities penetrating in grain boundary can induce a drop of interfacial strength with a function of local concentration [19,60]. Several sophisticated grain boundary fracture mechanisms under environmental corrosion were proposed in early studies and reviewed by Faulkner [15]. For simplicity, a simple description is implemented to study corrosive degradation effect following the idea developed by Scheider et al. [19].

Local impurity concentration dependent degradation can be evaluated by considering reduction of maximum cohesive strength $\sigma_{\max}$, characteristic separation δ_n and δ_t. They are functions of the concentration:

$$\sigma_{\max}(c) = \sigma_{\max}(0)(1-\mu c), \tag{3.7}$$

$$\delta_n(c) = \delta_n(0)(1-\mu c), \tag{3.8}$$

$$\delta_t(c) = \delta_t(0)(1-\mu c), \tag{3.9}$$

where μ is a cohesive strength degradation factor. To illustrate how concentration affects the cohesive surface mechanical behavior, the concentration dependent traction-separation curves are plotted for normal traction in Fig. 3.1(a) and tangential traction in Fig. 3.1(b) respectively. These three parameters can give some indications of the contacting surface characterization of fracture toughness for Mode I crack-like behavior in plane strain using relation $K_{IC} = (1- m)\sqrt{\frac{E}{1- n^2}\mathsf{F}_n}$.

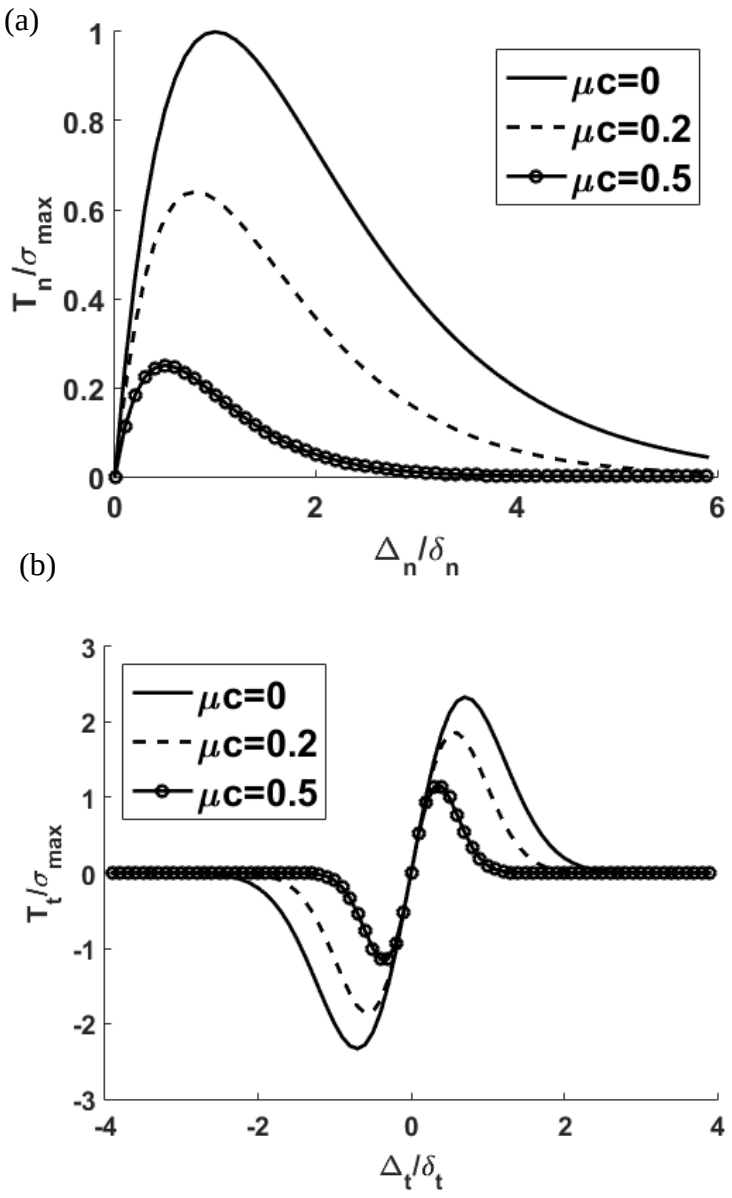

Figure 3.1 Concentration-dependent traction-separation relationships in (a) normal direction and (b) tangential direction, with tangential separation Δ_t and normal separation Δ_n being zero respectively. For simplicity, $\delta_n = \delta_t$.

3.2.3 Description of CPFEM

The adopted crystal plasticity model is based on the classic crystal plasticity theory developed by Peirce et al[5], and the ABAQUS user defined material subroutine (UMAT) by Huang [11]. Based on this framework, many deformation mechanisms, such as dislocation (Chen et al., 2014) etc., can be considered to study more specific subjects. In this study, a general slip-based CPFEM is adopted for corrosion assisted intergranular failures. In CPFEM framework, the total deformation gradient $\mathbf{F}$ can be regarded as a cumulative deformation gradient attributed by two successive deformations gradients, elastic part $\mathbf{F}^e$ and plastic part $\mathbf{F}^p$, expressed as

$$F_{ij} = F_{ik}^{e} F_{kj}^{p} . \tag{3.10}$$

For the Schmid-type crystal plasticity, the plastic deformation rate is regarded as a summation of individual shear strain over all slip systems,

$$\dot{F}_{ik}^{p} F_{kj}^{p-1} = \sum_{\alpha=1}^{NSLIP} \dot{\gamma}^{(\alpha)} s_i^{(\alpha)} m_j^{(\alpha)}, \tag{3.11}$$

where NSLIP denotes the total number all activated slip directions, $\dot{\gamma}^{(\alpha)}$ is the slip rate of the α-th slip system, $s_i^{(\alpha)}$ and $m_j^{(\alpha)}$ represent the slip direction and slip plane normal. The power-law flow rule is used to describe the shear strain rate,

$$\dot{\gamma}^{(\alpha)} = \dot{\gamma}_0 \left| \frac{\boldsymbol{\tau}^{(\alpha)}}{\boldsymbol{\tau}_{flow}^{(\alpha)}} \right|^n \operatorname{sgn}\left(\boldsymbol{\tau}^{(\alpha)}\right) \exp\left(-\frac{Q}{kT}\right), \tag{3.12}$$

where $\dot{\gamma}_0$ is the reference strain rate, $\tau^{(\alpha)}$ and $\tau_{flow}^{(\alpha)}$ are the resolved shear stress and current slip strength of the α-th slip system respectively, and *n* is the stress exponent. When the stress exponent is smaller, it means the material is more rate-dependent. The thermal term $\exp\left(-Q/kT\right)$ is included here to consider the thermal activations from various mechanisms that contributing to the shear strain rate at different temperature [58]. Here, *Q* is the activation energy, *k* is the Boltzman constant, and *T* is the absolute temperature.

The Peirce-Asaro-Needleman model is introduced to describe the hardening behavior,

$$\dot{\tau}_{flow}^{(\alpha)} = \sum_{\beta} h_{\alpha\beta} \left| \dot{\gamma}^{(\beta)} \right|, \tag{3.13}$$

where $h_{\alpha\beta}$ are the hardening moduli. The self-hardening modulus is expressed as

$$h_{\alpha\alpha} = h\left(\gamma\right) = h_0 \operatorname{sech}^2 \left| \frac{h_0 \gamma}{\tau_s - \tau_0} \right|, \tag{3.14}$$

where no summation is assumed for the repeated index α, h_0 is the initial hardening modulus, τ_0 is the initial slip strength, and τ_s is the saturation slip strength. And the latent hardening part is given by

$$h_{\alpha\beta} = h\left(\gamma\right)\left[q + \left(1-q\right)\delta_{\alpha\beta} \right], \tag{3.15}$$

where $\alpha \neq \beta$, and *q* is the latent hardening coefficient.

3.3. Numerical Methodology

The proposed numerical approach embeds stress-coupled diffusion process into microstructure based model utilizing CZM. The diffusion process is affected by local stress both in grain boundaries and adjacent grains by considering pressure gradient in diffusion governing equation as described in Eq. (3.2). On the other hand, the diffused impurities can induce degradation of grain boundaries thus affecting stress field of grain interiors.

A two dimensional polycrystalline model with CZM coupled is sketched in Fig. 3.2(a). Each polygon represents an individual grain with different characteristic grain orientation denoted with different colors. Grain boundaries are highlighted with red solid lines consisting of four-node 2D user defined elements (UEL), and diffusion flux is denoted with multiple arrowed lines along the grain boundary. To illustrate how user-defined cohesive elements are coupled with two neighboring grains, one detailed sketch of grain boundary is shown in Fig. 3.2(b). The grain interior part is discretized with four-node hybrid element with reduced integration (CPE4HR). The thickness of grain boundary is extremely small relative to the grain dimension, thus initial separation of two cohesive elements is set to be zero. A new set of grain boundary node is duplicated based on the pairing grain's node set at grain boundary, and these two sets are sharing the same coordinates initially. Moreover, a sketch of grain boundaries at the junction point is presented in Fig. 3.2(c), where three nodes are paired. Note the thickness of grain boundaries are exaggerated in Fig. 3.2 (b) and (c).

The governing stress coupled diffusion equation can be expressed as Eq. (3.1). Since impurity diffusion is considered only along grain boundaries, one-dimensional

Figure 3.2 (a) A sketch of 2-D polycrystalline example model with CZM grain boundaries (GBs). (b) It shows how concentration dependent CZM is implemented between two grains. (c) Implementation of CZM at grain boundary junction points. The thickness of CZM layer is exaggerated in this sketch.

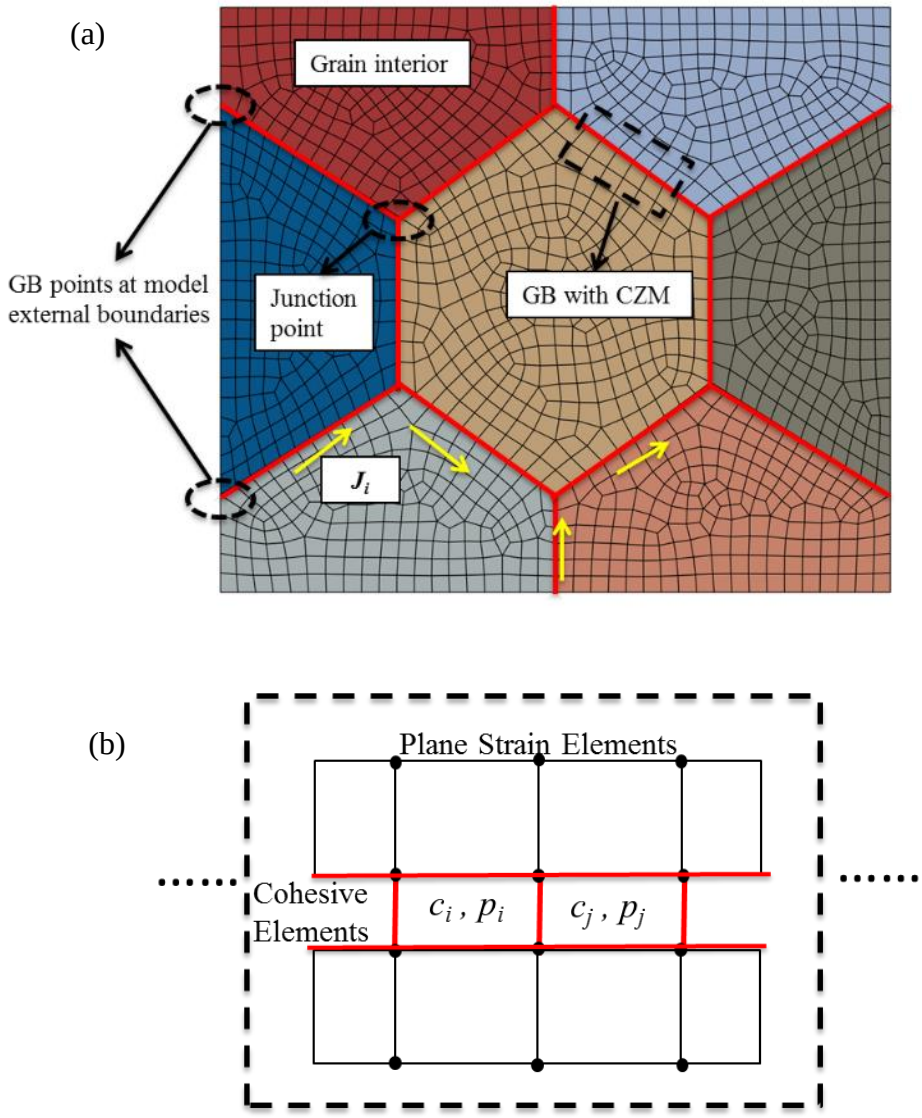

Figure 3.2 continued

(c)

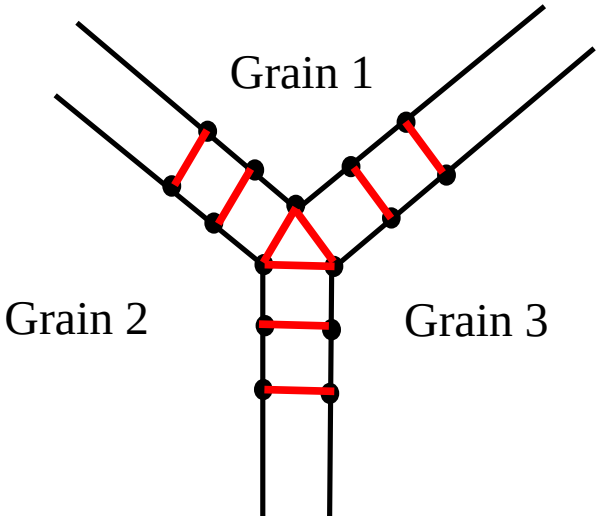

Figure 3.2 continued

form of diffusion described as Eq. (3.2) is adopted in this study. The stress-coupled diffusion governing equation, Eq. (3.2) is discretized with explicit finite difference method with forward difference at time t_n and second-order central difference for space derivation as follows,

$$\frac{c_j^{n+1} - c_j^n}{\Delta t} = D\left[\frac{c_{j+1}^n - 2c_j^n + c_{j-1}^n}{(\Delta x)^2} + k_p \frac{p_{j+1}^n - 2p_j^n + p_{j-1}^n}{(\Delta x)^2}\right], \qquad (3.16)$$

where c_j^n and p_j^n denote the concentration and pressure respectively at the *j*-element and the *n*-th time increment. To simplify this calculation, the grid length is considered to be uniform in this paper. Eq. (3.16) can be rewritten in the following form,

$$c_j^{n+1} = c_j^n + D\frac{\Delta t}{(\Delta x)^2}\left[\left(c_{j+1}^n - 2c_j^n + c_{j-1}^n\right) + k_p\left(p_{j+1}^n - 2p_j^n + p_{j-1}^n\right)\right]. \qquad (3.17)$$

For this central finite difference in space and explicit Euler method in time, the numerical stability can only be reached when

$$2D\Delta t \le (\Delta x)^2. \qquad (3.18)$$

At the beginning of each calculation step, each user-defined element is called for assembling stiffness matrix. As described in Section 2, the strength of interfaces is the function of concentration. Thus, diffusion equation is solved before stiffness matrix assembling and then updates the cohesive element strength according to the current concentration. Given Eq. (3.17), in order to get the update of concentration of c_j^{n+1}, the information of concentration and local pressure at $j-1$, j and $j+1$ element is required in

this scheme at t_n . However, UEL does not provide an interface to store and extract the information of neighboring elements while solving diffusion equation. In order to gathering necessary values for gradient terms in Eq. (3.17), the COMMON block technique is introduced for data storage and calling, as illustrated in Fig. 3.3.Four COMMON blocks are constructed to store pressure and concentration in both previous and current steps. These data are identified with user defined element number. At initial increment of the calculation, all the grain boundary cohesive elements are initialized according to boundary condition in current COMMON block sets, P_NEW and C_NEW. At the beginning of next increment, the data stored in current COMON blocks are transferred to old COMMON block sets, P_OLD and C_OLD. Then, the concentration information in each element is updated by solving Eq. (3.17) based on the correspond data in P_OLD and C_OLD, and stored in current COMMON blocks. The value of pressure is calculated based on normal traction as defined in Eq. (3.5). However, user defined element can be called multiple times in each increment. In order to distinct new increment and old increment with second call, a signal flag is defined to judge different cases.

According to the requirements of FD algorithm, two additional boundary condition need to be defined in addition to Eq. (3.17). There are two types of boundary condition considered in current cases. First, at model external boundaries, the concentration keeps same as bulk concentration or environmental concentration. The example of grain boundary points is illustrated in Fig. 3.2(a). The concentration of these points is defined at initial increment, and keeps constant during simulation. Second, the implementation of CZM at grain junction point is shown in Fig. 3.2(c), and diffusion

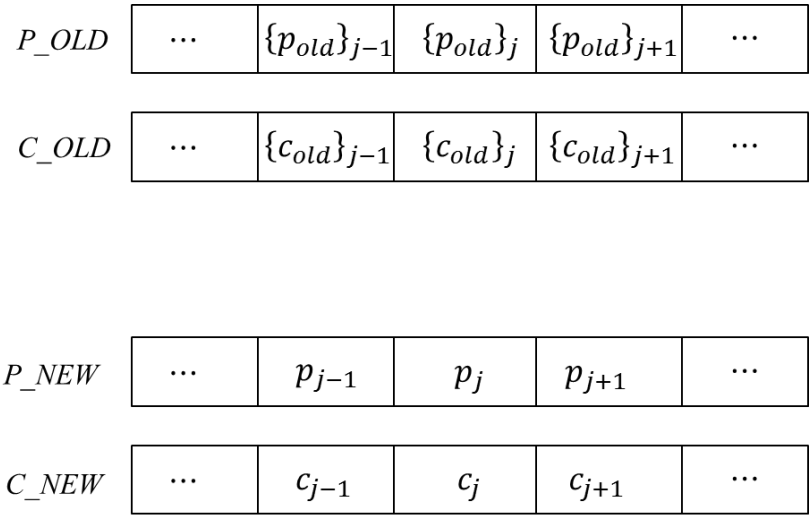

Figure 3.3 COMMON blocks for concentration and pressure updates.

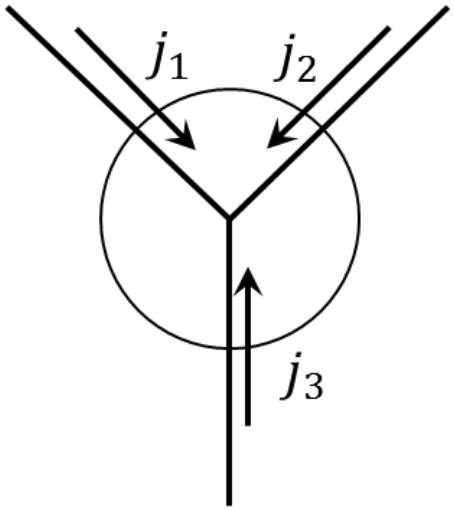

Figure 3.4 Illustration of diffusion flux at grain junction point.

fluxes are illustrated in Fig. 3.4. Based on mass conservation and inspired by analogy of Kirchhoff's current law, the sum of fluxes diffusing into the junction point is equal to the sum of fluxes flowing out.

If the flux direction flowing in is defined as positive, thus the algebraic sum of all flux vanishes, as expressed,

$$\sum_k j^k = 0. \tag{3.19}$$

Derived from Eq. (3.1) in 1D form, the flux can be written based on FD algorithm as,

$$j^k = \frac{D}{\Delta x}\left[\left(c_1 - c_2\right) + k_p\left(p_1 - p_2\right)\right], \tag{3.20}$$

where the subscript of concentration c_i and pressure p_i means the location of element. When $i=1$, it represents the element right next to the junction point, and $i=2$ denotes further element. Substitute Eq. (3.20) into Eq. (3.19) and suppose the time is small according to time span requirement as described in Eq. (3.18), the update of concentration can be expressed as follows, for grain boundary triple junction point.

$$\left\{c_1^{n+1}\right\}_i = \left\{c_2^n\right\}_i - c_{term} - k_p p_{term} \tag{3.21}$$

where

$$c_{term} = \left\{c_1^n\right\}_j - \left\{c_2^n\right\}_j + \left\{c_1^n\right\}_k + \left\{c_2^n\right\}_k, \tag{3.22}$$

$$p_{term} = \left\{p_1^n\right\}_i - \left\{p_2^n\right\}_i + \left\{p_1^n\right\}_j - \left\{p_2^n\right\}_j + \left\{p_1^n\right\}_k + \left\{p_2^n\right\}_k. \tag{3.23}$$

In Eq.(3.21) – (3.23), the subscript and superscript inside bracket mean location of elements and time increment number. The subscript outside bracket means the number of grain boundary connected to current junction point.

In some other boundary conditions, it requires additional functions. Like for symmetric boundaries, the flux at such grain boundary vanishes. Thus special boundary conditions are also applicable in this model following the same routine described above. A set of indicators is created to distinct internal point and different types boundary condition points.

3.4. Numerical Examples

3.4.1 Comparisons between FD based CZM and FEA diffusion

To verify the diffusion solver embedded in cohesive zone model, a three grain boundaries example model with one junction point is simulated with both FD based CZM and ABAQUS diffusion module. Since only sequential coupled diffusion process is provided in ABAQUS, merely diffusion procedure is compared in this section.

A tri-grain model consisting of three grains and one grain boundary junction point is adopted in for the comparison and illustrated in Fig. 3.5. The grain boundaries are illustrated with dashed circle. In FEA-based diffusion simulation, one-dimensional diffusion element (DC1D2) is implemented for grain boundary diffusion and four-node two-dimensional diffusion element (DC2D4) is utilized for grain internal diffusion. However, since the diffusion inside grains is not considered in CZM model, the diffusivity is set to be 0 for grain elements in order to suppress diffusion in FEA-based diffusion simulation. At model boundaries, there are boundary 1 and boundary 2 as illustrated in Fig. 3.5. Boundary 1 is considered as the boundary exposed to environment.

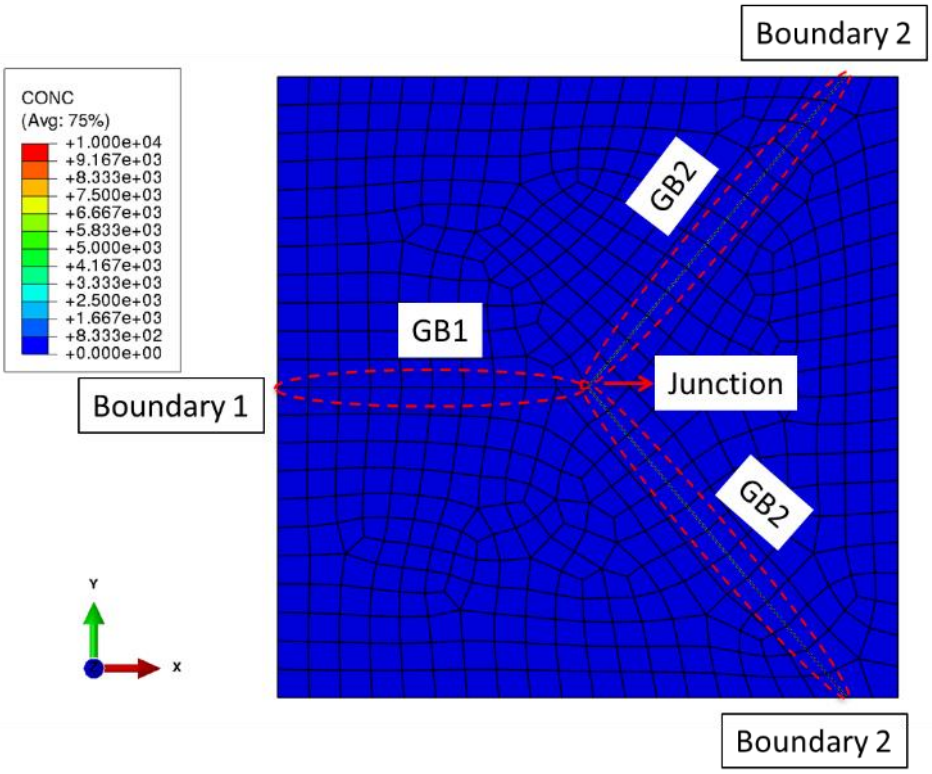

Figure 3.5 Tri-grain model for FD based CZM and FEA diffusion comparison.

Thus, it has a constant concentration same as environmental concentration. Since this tri-grain model is small relative to bulk material size, the concentration at Boundary 2 is assumed to be equal to bulk concentration and keep constantly. In FD based CZM model simulation, the cohesive elements are implemented along grain boundary as described in Section 3.1. Because the stress effects will not be considered in this comparison, the external load will be neglected in this simulation.

The length scale is very critical in the simulation for FD algorithm as indicated Eq. (18). To increase the limit of time span for long-term simulation, large element size is desired in the simulation. However, normal grain size is usually in the region of 0.01 mm to 0.1 mm. Millimeter is usually adopted in micro-scale simulation, but it is not suitable in this simulation. The time span is restricted to be in the scale of 10^{-4} according to Eq. (3.18) if millimeter is adopted in grain-level simulation. As a result, micrometer is proposed to be utilized in FD based CZM simulation. Unit consistency is explained in Appendix and all the relevant units are also tabulated. Since the no stress effect is considered in this comparison, diffusion relevant parameter is listed in Table 3.1.

Measurement for grain boundary diffusivities is very limited in current experimental techniques [62]. Oxygen diffusivity in nickel based supealloy is estimated based on the Focus Ion Beam observations for oxidation layer depth [21]. Besides, as mentioned in introduction, grain boundary diffusivity is usually $10^5 \sim 10^8$ times higher than that inside grains [46]. Thus, diffusivity is estimated as $0.1085 \mu m^2/s$ and oxygen diffusivity in nickel-based superalloy is adopted for the rest of this work as examples.

Table 3.1 Parameters in FD based CZM and FEA diffusion comparison.

Concentration at boundary 1, C_1	Concentration at boundary 2, C_2	Diffusivity, D	Element Size, Δx
$10^4\ atoms/\mu m^3$	$100\ atoms/\mu m^3$	$1.085\ \mu m^2/s$	$0.5\mu m$

FD based CZM and FEA diffusion simulations are conducted respectively with simulated diffusion time equal to 3600s. Since diffusion along grain boundary is relative fast, the concentration profile along each grain boundary reached stable condition and remains constant without stress effect considered. The comparisons for concentration profile along different grain boundaries are plotted in Fig. 3.6 in logarithmic scale for concentration axis. In Fig. 3.6, the distance for GB1 is measured starting from point from Boundary 1 as illustrated in Fig. 3.5 and distance for GB2 is measured from junction point. Due to the model symmetry, the profiles for two GB2 are consistent thus not shown for both GB2.

The predictions of FD based CZM and FEA diffusion shows similar concentration profile after 3600 seconds. The special technique described in Section 3.3 is utilized at junction point in FD based CZM, and this induces slight discrepancy for the concentration close to junction point.

3.4.2 Effects of stress fields on diffusional process

Researchers always use the impurity concentration as a criterion for material damage [21,38,56]. It has been recognized the pressure gradient can affects the impurities transporting speed in diffusion process. Impurities are likely to concentrate at the grain junction points due to the extraordinary heterogeneity of stress field, forming a “hot zone” of degradation. However, since the diffusion is time dependent, a competition exists between the external load and diffusion process.

To shows how stress field affects the diffusion process, a sequential coupled diffusion model is constructed with microstructure considered as shown in Fig. 3.2 (a). FEA-based diffusion simulation is only considered in this section, thus the settings of

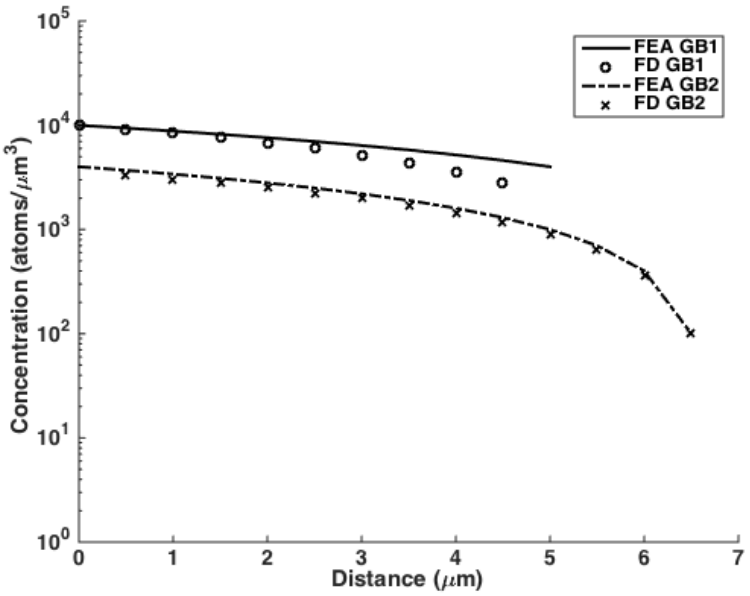

Figure 3.6 Concentration profiles for GB1 and GB2 are compared between FD based CZM and FEA diffusion at t=3600s.

model are similar with that in section 3.1 except that the mechanical loading is considered in this simulation. CPFEM is adopted for individual grain interior with various grain orientations, of which the governing equations are as described in Section 2.3. In our previous work [7], nickel-based superalloy material with CPFEM and the parameters from this reference will be utilized in our simulations, as listed in Table 3.2. Nickel-based superalloy has FCC structure with three independent anisotropic elastic constants c_{11}, c_{12} and c_{44} with values tabulated in Table 3.2. The activate slip system is chosen as $\{111\}\langle 110\rangle$ system for FCC crystallographic structure. The right and bottom model edges are subjected with horizontal and vertical symmetric boundary condition separately. A linearly time-dependent displacement is applied on the top, with a strain rate of $\dot{\varepsilon} = 10^{-3} s^{-1}$. The left boundary are exposed the external environment with a constant concentration of $c_0 = 10^4\ atom/\mu m^3$, while the other boundaries are assumed with a small bulk concentration as $c_{bulk} = 10\ atom/mm^3$.

The mechanical simulation is executed at first with output of pressure field in an external file. The contour plot of pressure at 100s is shown in Fig. 3.7(a). Following mechanical simulation, FEA based simulation is carried out considering the pressure effect. As mentioned in [21,62], very few studies presents the pressure factor and diffusivities in diffusions due to the limitation of measurement techniques. It can be only estimated from indirect experimental fittings. We adopted the pressure factors and diffusivities according to the predicted range from the study of [21] in this simulation. It has been pointed out the simulation of Karabela et al.'s study actually considered diffusion for grains without separating grain boundary and interiors.

Table 3.2 Constitutive parameters used in the crystal plasticity model of a nickel-based superalloy.

c_{11} (GPa)	c_{12} (GPa)	c_{44} (GPa)	n	h_0 (MPa)	τ_0 (MPa)	τ_s (MPa)	q
254.4	177.0	120.5	50	550	110	750	1.0

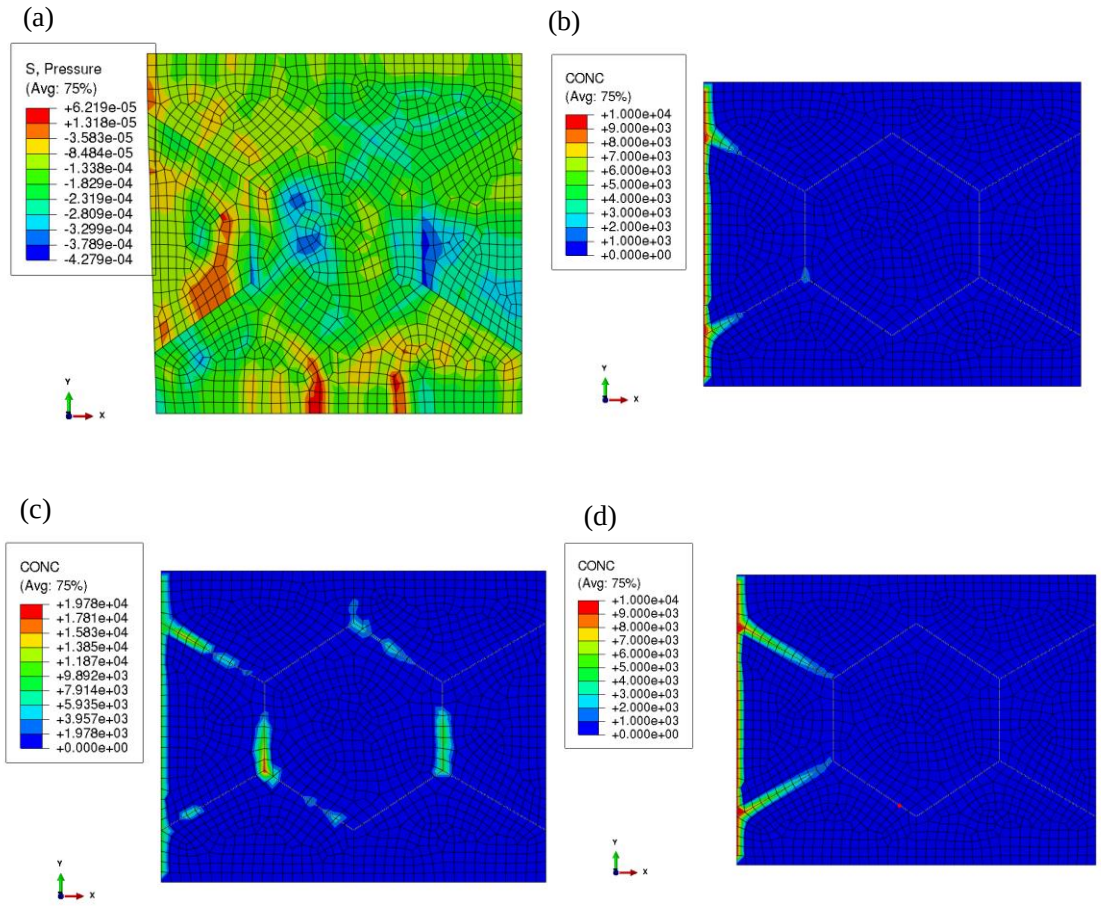

Figure 3.7 Sequentially coupled diffusion under pressure effects. (a) Pressure field at 100s; (b) Concentration distribution at 10s and (c) at 100s; (c) Comparative non-stress coupled diffusion at 100s.

Thus, the pressure factor k_p in Eq. (3.1) is $10^5\ \mu m^2/N$ for grain interiors, and $10^8\ \mu m^2/N$ for grain boundaries considering the diffusion process is more significant at grain boundary.

The contour plots of concentration distribution at 10s and 100s are shown in Fig. 3.7(b) and (c). In order to emphasis the pressure effect, a comparative simulation is conducted without stress coupled. Note that the legend spans in these contour plots are not same.

At 10s, the concentration distribute at the surfaces considering relative pressure gradient and short diffusion time. This will cause a localized corrosion at the surfaces, which may lead to a surface crack at the beginning. As the loading continues, both pressure and chemical gradient drive the impurities to diffuse deeper in the materials. However, as strong heterogeneous pressure field exists at several junction points, the impurities start to accumulate at these points as shown in Fig. 3.7 (c) comparing to Fig. 3.7 (d). This results in a severe degradation at the junction points as well as connecting grain boundaries. These results demonstrate the negative pressure field can drive the impurities to forming a "hot zone" with high concentration. These areas can be considered as weak points, which cause material internal fracture under degradation considered.

4.3. Fracture initiation mechanism

The impurity concentration field can be considered as a factor of material failure. However, merely concentration is not sufficient since the degradation of grain boundary is not considered in above simulation. In this section, stress coupled diffusion CZM will be used to study the fracture initiation mechanism of polycrystalline material.

The method to construct polycrystalline model with CZM has been introduced in Section 2.1. For stress-coupled diffusion CZM, both mechanical properties and mass transportation parameters are required as indicated in Section 2. Parameters for describing cohesive zone traction and separation relationship are based on the study of [63]. Characteristic separation δ_n and maximum characteristic traction $\sigma_{\max}$ in Eq. (3.5) - (3.6) are taken as, 1 nm and 1 GPa respectively. For simplicity, the mechanical parameters in tangential direction are identical to those in the normal direction. For diffusion part, diffusivity is identical to the parameter used in tri-grain model as listed in Table 1. As described in Eq. (3.7) - (3.9), the degradation of interfacial strength can be expressed with degradation factor μc_0 , where c_0 is reference concentration. In this simulation, c_0 is taken as the maximum concentration in the system. It is clear that μ has to satisfy $1-\mu c_0 > 0$. In this polycrystalline model, the points on left model boundary are considered to expose to environment, where the concentration keeps constant at these two points. All the points at other model boundaries are considered as material bulk concentration. The freedom of vertical direction for bottom boundary in Fig. 3.2 is constrained and one of the corner points at bottom is fixed. The top boundary applied with linearly increasing displacement with different strain rates.

At strain rate $\dot{\varepsilon} = 10^{-3} s^{-1}$, several simulations are carried out with different degradation factor μc_0. Three types of damage types are observed as illustrated in Fig. 3.8 (a) – (c) separately, and the corresponding stress-strain curves are plotted in Fig. 3.9. The stress-strain curves of two comparative models are also included. The “perfect bonding” means tied constrains is defined at the grain boundary, and “UEL without

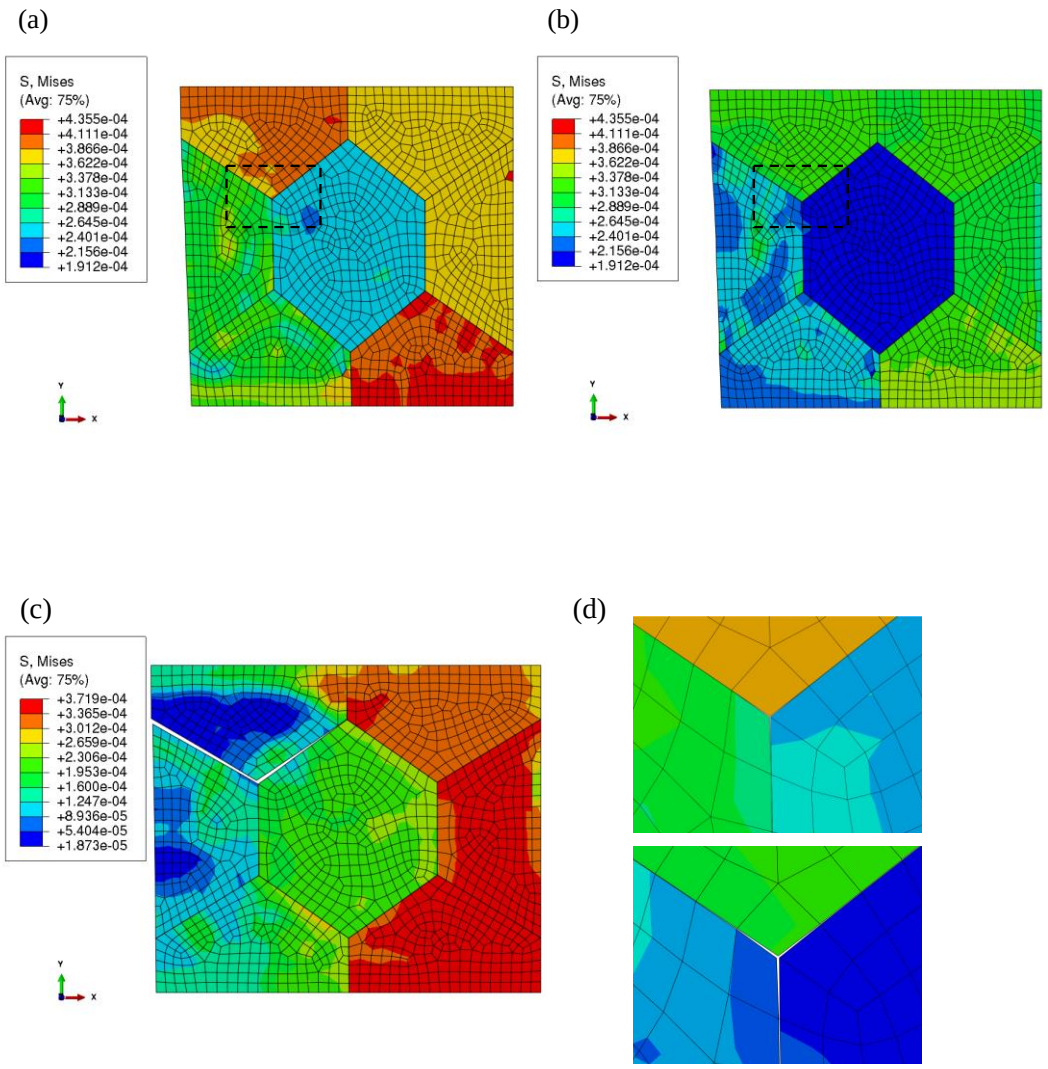

Figure 3.8 (a)-(c) Different damage types with various degradation factor at $\dot{\varepsilon} = 1 \times 10^{-3} s^{-1}$. (d) Zoomed-in images of junction points showing the internal crack (boxed area in (a) and (b)).

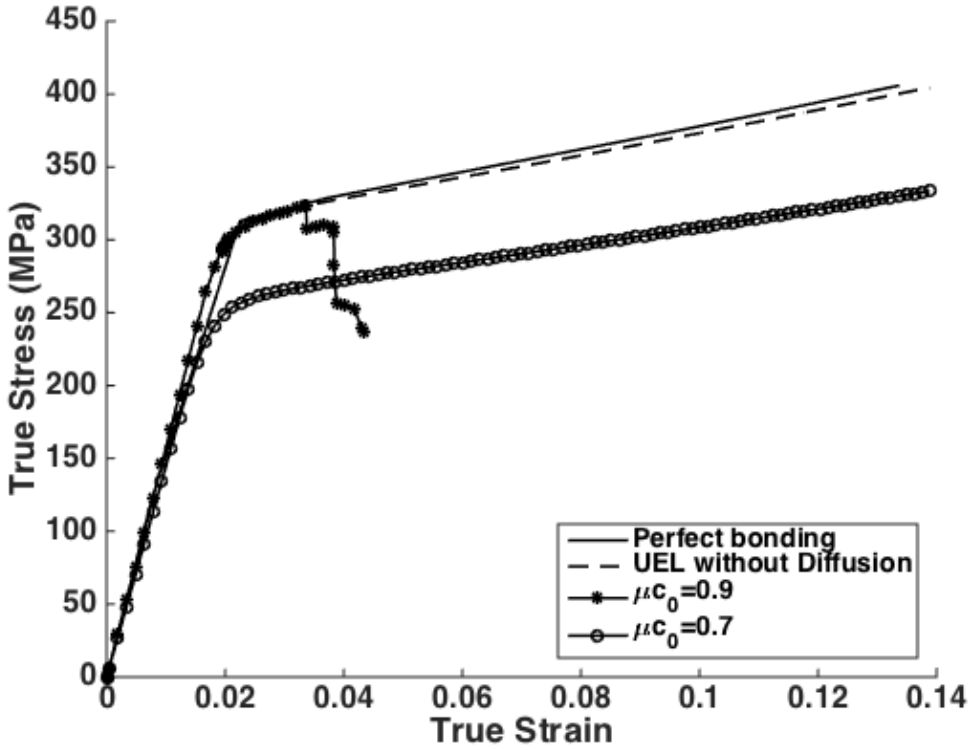

Figure 3.9 Stress strain curves for different type of fracture models at strain rate 10^{-3} s^{-1}.

diffusion" means cohesive element is applied at grain boundaries without diffusion process considered. Since the stress-strain curve overlaps that with that of "UEL without diffusion", it is not shown in Fig. 3.9.

Type 1 damage as shown in Fig. 3.8(a). In this type of damage, the concentration induced degradation is too small to effect intergranular cracking significantly. It shows a similar behavior as the model with non-concentration dependent cohesive elements.

Type 2 damage as shown in Fig. 3.8(b). No obvious cracking can be observed in this type of damage. However, the average stress level is much lower than the Type 1 damage. This means the impurities have degraded the strength of grain boundaries interactions. The grain boundary can hardly bear large tractions but can provide large separation to accommodate the structure elongation. However, the degradation is not significant enough to form a surface crack similar with Fig. 3.8(c). These internal cracks are very trivial in the image of whole model. When the boxed part of Fig. 3.8 (a) and (b) is zoomed in as shown in Fig. 3.7(d), it is more obvious. This damage pattern can be also observed in the stress-strain curve in Fig. 3.9.

Type 3 damage as shown in Fig. 3.8(c). The degradation plays an important role in the model damage, and crack is initiated at surface and prorogated along the grain boundary. When crack reaches the grain boundary junction point, a competition exits between two connecting boundaries. The crack propagates along the "weaker" boundary and causes a sudden drop of stress.

As we can see in above analysis, the degradation factor determines the damage types. In Type 1 and Type 2 damage, no surface crack is observed even though the surface

layer are exposed to environment and immediately charged with high concentration of impurities. But the degradation is not sufficient enough to form a crack. In these cases, the internal oxidation is dominant in the model of damage. On the other hand, when environmental corrosion is severe enough, it leads to a surface fracture and the crack propagate as external loading is kept until it stops at one competing point. The surface degradation intensity dominates this type of damage mode.

3.5. Conclusions

This study proposes a numerical approach to simulate intergranular cracking by considering stress coupled diffusion process along the grain boundary. The diffusion simulation is embedded in CZM model based on finite difference algorithm and implemented in ABAQUS UEL code. This diffusion-coupled CZM is applicable in different types of boundary conditions, such as grain junction point. A polycrystalline model is successfully simulated with combining CPFEM for grain interiors and diffusion-coupled CZM for grain boundary. The intergranular damage mechanism has been revealed for the material subjected to environmental corrosion and three types of damage modes are reveals with different degradation factors. This study still has limitation to study a comparable simulation with real experimental observation. Technical efforts are necessary for applying developed CZM code in more general cases consisting of a larger number of grains and complicated grain boundary configurations. Comprehensive model descriptions corresponding to diffusion degradation and mechanical response needs to be developed for specific conditions

Appendix. Unit Consistency for Micrometer Length Scale

To increase the time span limitation, micrometer is utilized in this simulation. According the ABAQUS manual [55], unit consistency need to be defined by users. Length unit and mass unit are required to be changed so as to keep force unit as newton in all SI unit consistent system. Based on this idea, all relevant units are converted and tabulated in Table 3.3.

Table 3.3. Unit consistency system

Quantity	**SI (m)**	**SI (μm)**
Length	m	μm
Force	N	N
Mass	kg	Mega-kg (10^6kg)
Time	s	s
Stress	Pa	Tetra-Pa (10^{12}Pa)
Diffusivity	m^2/s	$\mu\mathrm{m}^2/s$ (10^{-12} m^2/s)
Concentration	$\mathrm{atoms}/\mathrm{m}^3$	$\mathrm{atoms}/\mu\mathrm{m}^3$ (10^{18} $\mathrm{atoms}/\mathrm{m}^3$)

Chapter 4 Development, Application and Verification of Elevated Temperature Creep-Fatigue Code Based on Elastic-Perfectly Plastic Analysis

4.1. Introduction

Due to its strength at very high temperatures up to 950^oC, Alloy 617 is the reference material for Very High Temperature Reactor (VHTR) components that operate at or near the outlet gas temperature of the reactor. However, the current rules in Subsection NH for the evaluation of creep-fatigue damage using simplified methods based on elastic analysis have been deemed inappropriate for Alloy 617 at temperatures above 650^oC (1200^oF) [64]. The rationale for this exclusion is that at higher temperatures it is not feasible to decouple plasticity and creep, which is the basis for the current simplified rules. This temperature, 650^oC (1200^oF), is well below the temperature range of interest for this material for the High Temperature Gas Cooled Reactor (HTGR) as well as the VHTR. The only current alternative is, thus, a full inelastic analysis requiring sophisticated material models [65] that have not yet been formulated and verified. An additional impediment to the use of full inelastic analysis is the level of expertise and experience required to implement these models and interpret the results.

To address the limitation on the use of current methods at very high temperatures, proposed code rules have been developed which are based on the use of elastic-perfectly plastic (EPP) analysis methods and are expected to be applicable prediction for design life for high temperature sturctures [22,23]. The use of simplified elastic-plastic analysis methods avoids the complexities and limitations of the traditional ASME linear elastic

stress classification design methods. The simplified methods exploit the fact that elastic-plastic methods naturally handle the stress redistribution which is the key to stress classification schemes. For high temperature design, creep strain and stress redistribution occur naturally in service. The use of a time-independent analysis to characterize these processes is not necessarily intuitively obvious. Their justification by the judicious use of proofs based on general material models is therefore essential for complex high temperature design and life assessment.

One test concept, called a Simplified Model Test (SMT), takes into account the stress and strain redistribution in realistic structures by including representative elastic follow-up characteristics in the test specimen [25]. The SMT approach to determination of cyclic life at elevated temperature avoids parsing the damage into creep and fatigue components with the use of a test specimen with elastic follow-up to represent the stress and strain redistribution encountered in more complex structures. The SMT specimens, sized based on elastic-follow-up concepts, are cycled to failure and the data generated are used directly to develop a cyclic design curve for actual components.

Tests were also initiated on cylindrical specimens design to be compatible with a test setup designed to accommodate test specimens with the follow-up characteristics to provide an upper bound of actual components. During testing of the “standard” SMT specimens, there was a problem dealing with the need to have a long, larger diameter, “driver section” to achieve higher, bounding values of elastic follow-up, in order to cause failure to occur in the shorter, narrower “test section” and to meet the requirement for a uniform temperature throughout the active length of the specimen. The problem occurred because the specimens sized to have a uniform temperature did not have enough available

driver length to achieve the desired follow-up characteristics to envelope the response of actual components. This was exacerbated by the need to provide a generous transition radius between the narrower test section and the larger diameter driver section to avoid failure at the stress concentration at the start of the transition radius. Failure at the transition radius does not compromise the use of the data for validating the EPP Code Cases. This is because the EPP Code Case is applicable to any geometry, so in that sense, the transition radius is just another geometric variable to account. On the other hand, it does impact the use of the data for the longer term goal of design curve development because the design curve logic is based on failure in the test section.

To address this issue, a new type of specimen designated as the YSMT was developed to meet the multiple goals of uniform test temperature, failure in the test section and adequate bounding follow-up. Simply put, the YSMT specimen uses active control of a scaled driver section displacement in conjunction with the measured displacement in the test section to achieve the equivalent behavior of a standard SMT specimen. This approach also permits a generous transition radius to promote failure in the test section. Initial tests have been undertaken during the last reporting period to demonstrate the feasibility of the YSMT approach. Further YSMT testing identified a problem with buckling of the solid bar type specimens that was resolved by optimizing the design of a cost effective tubular specimen.

Finite element analysis is the fast and low-cost method to validate the EPP proposed creep-fatigue damage following the code case procedure. FEA model could accurately represent the component geometry and loading conditions, transient and steady state including details such as local stress risers and local thermal stresses. According to the

proposed EPP code case, creep damage and fatigue damage can be calculated based on the FEA simulation results. What's more, with the function of buckling analysis, the simulation results provide the instruction for YSMT specimen design.

This chapter is outlined as follows. At first, background of shakedown analysis for cyclic creep damage and SMT test will be briefly introduced. Then, the conservation of EPP methodology is demonstrated analytically. In the next section, FEA EPP analysis will be presented to compare with SMT test results, and then allowable design life will be predicted as well in this section. EPP development and validation will be summarized at last.

4.2. Theoretical Basis of EPP Analysis

The use of bounding simplified solutions to characterize complex structural creep problems is well established. The most widely used methods are for reference stress solutions to constant load problems as, for example, reviewed in [66].These ideas have been developed and implemented for this application with the use of a temperature-dependent material property as an artificial yield stress in limiting elastic-plastic calculations. This approach is common to low and high temperature primary load design methods [22,23], and to high temperature cyclic load designs[23,66].

The use of simplified elastic-plastic analysis methods avoids the complexities and limitations of the traditional ASME linear elastic stress classification design methods. These simplified methods exploit the fact that elastic-plastic methods naturally handle the stress redistribution which is the key to stress classification schemes. For high temperature design, creep strain and stress re-distribution occur naturally in service. The use of a time-independent analysis to characterize these processes is not necessarily intuitively obvious.

Their justification by the judicious use of proofs based on general material models is therefore essential for complex high temperature design and life assessment.

The basis for the proposed simplified methods is generally expressed in terms of solutions which approximate the limiting case of the “rapid cycle” solution. This is the “optimum” shakedown solution. There is a “hierarchy” of bounding solutions which reflects the trade-off between problem complexity and bounding accuracy as follows.

The elastic shakedown solution (SD) is not unique and refers to any elastic solution with a constant residual solution. It provides a conservative (upper bound) estimate of the energy dissipation per cycle, or of creep damage per cycle. The optimum shakedown solution, that is, the rapid cycle solution (RC). This is the least conservative, physically achievable shakedown, or time-independent, solution. The realistic steady cyclic creep solution (SC). This requires a full cyclic creep analysis to obtain.

These three solutions are ranked by decreasing conservatism, (increasing accuracy) and increasing difficulty of calculation. In this code case, the focus is on creep-fatigue and cyclic creep damage. The optimum, or least conservative, shakedown solution, will therefore maximize rupture time. The proposed method for evaluation of creep-fatigue damage makes use of a rapid cycle solution (RC), which will provide a conservative bound to rupture time, energy, work, strains and displacements for the realistic steady cyclic solution (SC)

Rapid cycles have no creep relaxation during the cycle, but generally have the most advantageous residual stress system, which ensures that deformation rates over the cycle are as low as possible. In terms of deformation and strain accumulation over time, rapid

cycles are more conservative than slow cycles. Therefore, if creep-fatigue limits can be demonstrated for rapid cycles, slower cycles with relaxation will also satisfy the creep-fatigue limits.

The proposed creep-fatigue code case uses a conventional creep-fatigue damage summation. The cyclic creep component of damage is defined by an elastic-perfectly plastic (EPP) shakedown calculation. Taking shakedown solution into consideration, the solutions can be ranked in terms of energy dissipation per cycle as follows[23,66]

$$W_{SC} \leq W_{RC} \leq W_{SD} \tag{4.1}$$

The steady cyclic solution and the limiting case of the rapid cycle solution are physically realistic and achievable, the latter in the limit of short cycle times. The EPP strain limits analysis for the maximum acceptable design life bears a similar relationship to the RC solution that a reference stress limit analysis bears to a steady state creep solution.

Because of the point-wise nature of the cyclic creep-fatigue damage EPP calculation, damage and energy dissipation integrated over the volume are not directly used for prediction of cyclic creep damage.

The example of a creep-fatigue test analyzed is given in later sections. It will show the conservatism of the shakedown solution is consistent and reasonable.

4.3. Conceptual Basis of SMT Approach

Elastic follow-up can cause larger strains in a structure with displacement-controlled loading than would be predicted using an elastic analysis[25]. In a two bar example as shown in Fig. 4.1 (a), a displacement is applied to the end of the highly stressed bar. Although the stress in both A and B will relax due to creep, the higher stress in B will

cause further creep deformation in B and some of the initial elastic deformation in A will be absorbed in B – hence the term "elastic follow-up". Referring to Fig. 4.1 (b), elastic follow-up may be quantified by computing the ratio of ε_{0-2}, the creep strain in the test section including elastic follow-up, to the creep strain that would have occurred under pure relaxation, ε_{0-1}. Thus, the elastic follow-up, q, is given by:

$$q = \varepsilon_{0-2} / \varepsilon_{0-1} \tag{4.1}$$

The basic concept of the SMT methodology is shown in Fig. 4.2 (a). The component design is represented by a stepped cylinder with a stress concentration at the shoulder fillet radius. The component has a global elastic follow-up, q_n, which is due to the interaction between the two cylindrical sections, and a local follow-up, q_L, which is due to the local stress concentration. Generally, q is the ratio of the elastic follow-up strain to the elastically calculated strain as defined by Eq. (4.1).

If the thick cylinder is displaced radially inward a fixed amount, δ_{comp}, there will be a maximum strain at the area where stress concentration occurs. Although the actual strain may be higher, the relevant parameter in this approach is the maximum elastically calculated strain in the component, $\varepsilon_{E,\,comp}$. The effects of plasticity, creep and strain redistribution are accounted for in the simplified model test simulation. It is essentially the same as that used in Subsection NB, where the damage fraction is determined as the ratio of actual number of cycles, n, to the allowed number of cycles, N. The design curve envelopes the effects of hold time duration and follow-up magnitude without being excessively conservative. It is developed from SMT data that is plotted as elastically calculated strain vs. observed cycles to failure, Fig. 4.2 (b). The two-bar SMT

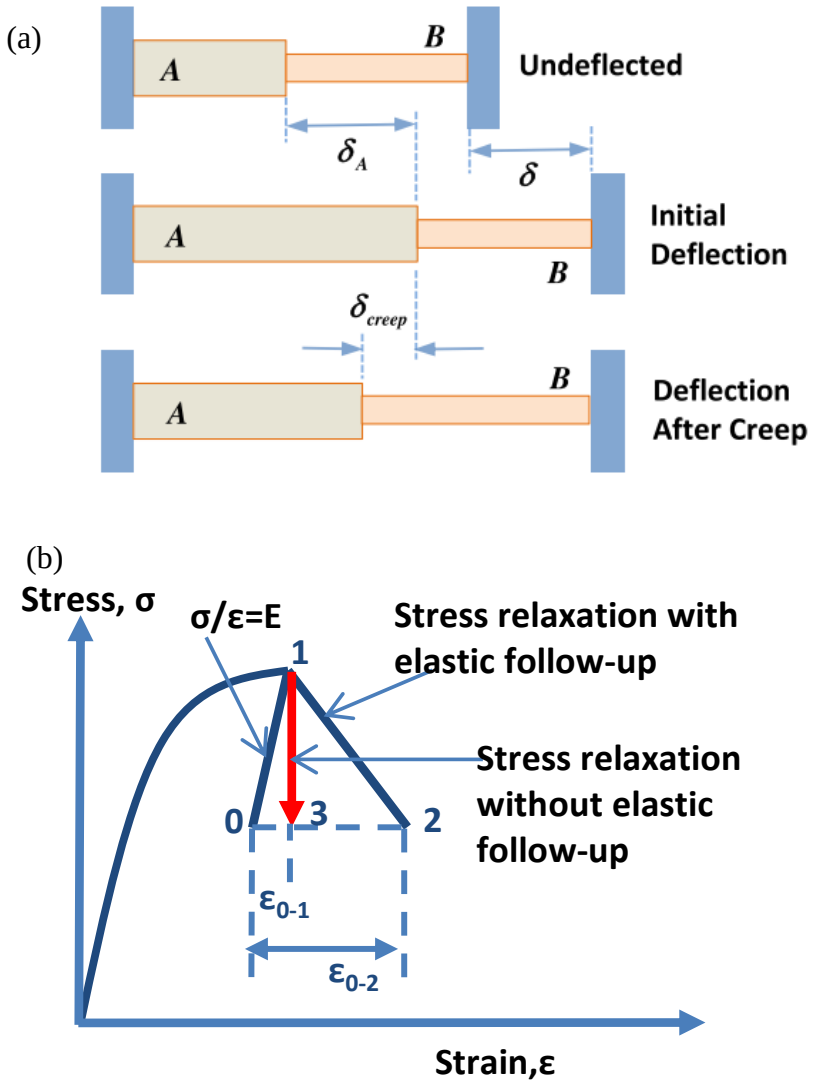

Figure 4.1 (a) Two-bar model to illustrate elastic follow up. (b) Definition of Elastic follow up

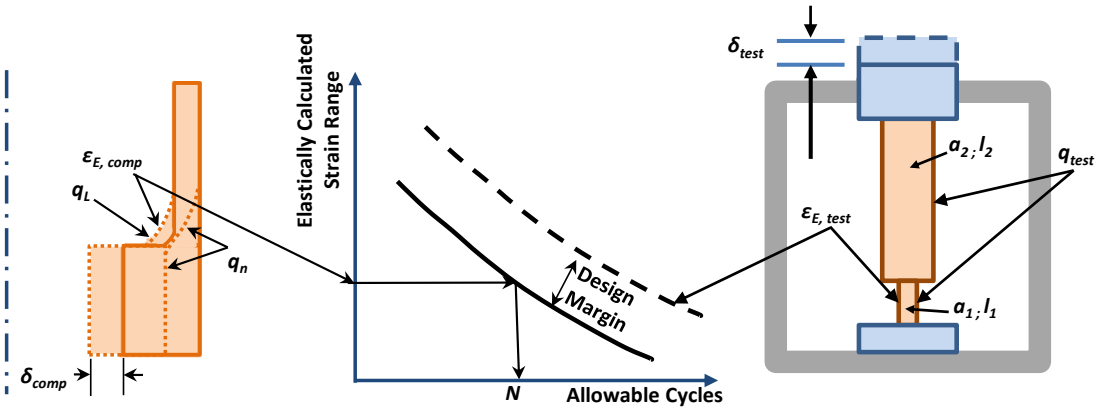

Figure 4.2 (a) Shell structure with stress concentration and elastic follow-up (b) Design curves for SMT methodology (c) Creep fatigue test setting up with elastic follow-up

specimen is sized to envelope the follow-up characteristics of interest.

A key point in the SMT approach is the use of elastically calculated strain in the test specimen to correlate the test results. The idea is that if, for the same elastically calculated strain, the effects of plasticity, creep and strain redistribution in the SMT specimen result in a stress-strain hysteresis loop that envelopes the hysteresis loop in the component, then the SMT results can be used to assess the cyclic damage in the component. A design margin must be applied to the test data to account for factors such as data scatter and extrapolation to longer hold times.

4.4. Bounding Analysis of Strain Controlled Creep-Fatigue Test Specimen

In this section, the EPP shakedown analysis is applied to the case of a strain-controlled creep-fatigue test. The Appendix A provides further details of calculations for stress and creep damage for a strain- controlled cyclic test.

Consider an example with ASME Section III, Division 5 Subsection HB, Subpart B Data for 316H stainless steel at 1400 ^{o}F. The test is characterized by a strain cycle $\Delta\varepsilon$ at temperature *T*.

For stress $2.5 \le \sigma \le 12$ *ksi* , creep and damage rates are:

$$\frac{d\varepsilon_c}{dt} = k\sigma^n, \frac{dD_c}{dt} = k'\sigma^{n'} \tag{4.2}$$

where constants *k, k', n, n'* are shown in Table 4.1.

According to the energy bounding theory, two solutions are taken into considered here.

4.4.1 EPP Elastic Shakedown Solution

Assuming within the test range, the geometry achieved shakedown condition as illustrated in Fig. 4.3 in red line, which satisfies

$$\sigma_1 = E\Delta\varepsilon / 2, \sigma_2 = -\sigma_1 \tag{4.3}$$

where Δε is the strain range during the experiment.

The damage accumulation over a half-cycle from the E-PP elastic shakedown solution, D_{epp}, is given by,

$$D_{epp} = k'\sigma_1^{n'}\frac{\tau}{2} \tag{4.4}$$

where τ is the time period of each loading cycle. Considering the holding time is much longer than the loading and unloading section, the time period during loading and unloading section is neglected in this condition.

4.4.2 Steady Cyclic Creep Solution

Under the constant strain rate condition with $\dot{\varepsilon} = 0$, the stress relaxation behavior can be obtained from

$$\int_{\sigma_0}^{\sigma(t)} \frac{d\sigma}{\sigma^n} = -Ekt \tag{4.5}$$

where $\sigma = \sigma_0$ at $t = 0$ neglecting the relatively short loading period. Integrating Eq. (4.5), we find

$$\frac{1}{1-n}\left(\left[\sigma(t)\right]^{1-n} - \sigma_0^{1-n}\right) = -Ekt \tag{4.6}$$

Table 4.1 Creep and damage constants for 316H stainless steel at 1400 ℉

	strain rate (n,k)	*damage rate (n', k')*
n, n'	5.192	4.369
k, k'	2.1992E-09	5.2083E-08

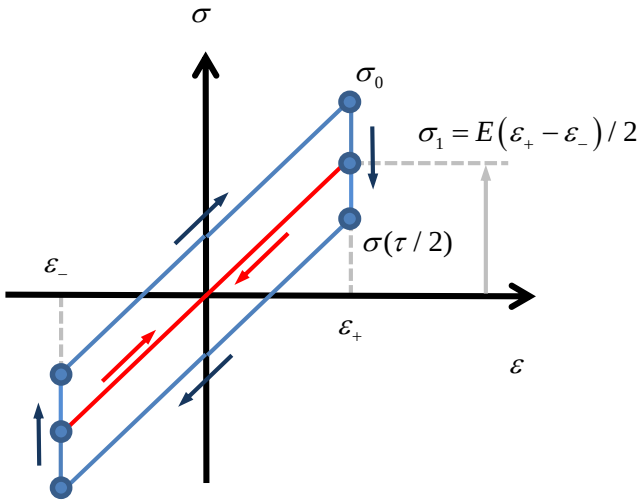

Figure 4.3 Steady cyclic creep condition (in blue) and EPP elastic shakedown condition (in red).

And

$$\sigma(t) = \left(\sigma_0^{1-n} - (1-n)Ekt\right)^{\frac{1}{1-n}} \tag{4.7}$$

The stress relaxation expression in Eq. (4.7) admits the limit

$$\lim_{n\to 1}\sigma(t) = \sigma_0 \exp(-Ekt) \tag{4.8}$$

According to Eq. (4.2), the damage accumulation over a half-cycle from the steady cyclic-creep solution, D_c, is given by

$$D_c = \int_0^{\tau/2} k'\left[\sigma(t)\right]^{n'} dt \tag{4.9}$$

Substituting the stress relaxation expression from Eq. (4.7) into Eq. (4.9), we find

$$D_c = \frac{k'}{kE(n-1-n')}\left[\left[\sigma(\tfrac{\tau}{2})\right]^{n'+1-n} - \sigma_0^{n'+1-n}\right] \tag{4.8}$$

According to the relationship between maximum stress and strain range as illustrated in Fig. 4.3, the condition for steady cyclic-creep solution is

$$\sigma_0 + \sigma(\tfrac{\tau}{2}) = E\left(\varepsilon_+ - \varepsilon_-\right) = E\Delta\varepsilon \tag{4.9}$$

Using Eqs.(4.4) and (4.8), the damage ratio between the steady cyclic-creep solution and the EPP elastic shakedown solution is

$$\frac{D_c}{D_{epp}} = \frac{1}{kE(n-1-n')}\frac{\left[\sigma(\tfrac{\tau}{2})\right]^{n'+1-n} - \sigma_0^{n'+1-n}}{\sigma_1^{n'}\tau/2} \tag{4.10}$$

where $\sigma_1 = \frac{1}{2}\left(\sigma_0 + \sigma(\frac{\tau}{2})\right) = E\Delta\varepsilon/2$. And from Eq. (4.6) at half cycle, i.e., at $t = \tau/2$, we get

$$Ek\frac{\tau}{2} = \frac{1}{1-n}\left[\sigma_0^{1-n} - \left[\sigma(\tfrac{\tau}{2})\right]^{1-n}\right] \tag{4.11}$$

Substituting Eqs. (4.10) and (4.11) into Eq. (4.8), the damage ratio becomes

$$\frac{D_c}{D_{epp}} = \frac{(n-1)2^{n'}}{(n-1-n')}\frac{\sigma_0^{n'+1-n} - \left[\sigma(\tfrac{\tau}{2})\right]^{n'+1-n}}{\left(\sigma_0^{1-n} - \left[\sigma(\tfrac{\tau}{2})\right]^{1-n}\right)\left[\sigma_0 + \sigma(\tfrac{\tau}{2})\right]^{n'}} \tag{4.12}$$

Under the condition of $n' = n$ the damage ratio is further reduced to

$$\frac{D_c}{D_{epp}} = 2^n(n-1)\frac{\sigma_0 - \sigma(\frac{\tau}{2})}{\left(\left[\sigma(\tfrac{\tau}{2})\right]^{1-n} - \sigma_0^{1-n}\right)\left[\sigma_0 + \sigma(\tfrac{\tau}{2})\right]^{n}} \tag{4.13}$$

To simplify the notation, we introduce the stress ratio s as

$$s \equiv \sigma_0 / \sigma(\tfrac{\tau}{2}) \tag{4.14}$$

The damage ratio then becomes

$$\frac{D_c}{D_{epp}} = \frac{2^n(n-1)(s-1)s^{n-1}}{\left(s^{n-1}-1\right)\left(s+1\right)^n} \tag{4.15}$$

We now investigate the behavior of the damage ratio as a function of n and s. Let

$$f(n,s) \equiv \frac{2^n(n-1)(s-1)s^{n-1}}{\left(s^{n-1}-1\right)\left(s+1\right)^n} \tag{4.16}$$

The result in Eq. (4.16) implies that as $s \to 1$ the creep deformation becomes vanishingly small and in the limit of $s = 1$ the creep deformation is frozen (e.g., $k = 0$) and the steady cyclic-creep stress state is reduced to the EPP elastic shakedown solution. This can be seen from Fig. 4.3. The Taylor series expansion of $f(n,s)$ about $s = 1$ gives

$$f(n,s) = 1 - a_0(s-1)^2 + a_0(s-1)^3 + O\left((s-1)^4\right), \quad a_0 = \frac{1}{24}n(n+1) \qquad (4.17)$$

where $O(\ )$ is the order symbol. This confirms that $f(n,s) \to 1$ as $s \to 1$. Also, for values of s slightly larger than one, Eq. (4.17) shows that $f(n,s) < 1$. Hence the damage accumulation from the steady cyclic-creep solution for small amounts of stress relaxation over the half-cycle is less than the damage calculated from the EPP elastic shakedown solution.

For large s, we find from Eq. (4.16) that

$$f(n,s) \sim \frac{2^n(n-1)}{s^{n-1}\left(1+\frac{n}{s}+\cdots\right)} \qquad (4.18)$$

so $f \to 0$ in the limit as $s \to \infty$. This is the case when the stress relaxation from the steady cyclic-creep solution over the half-cycle is complete, and the damage accumulation is vanishingly small as compared with the corresponding damage accumulation from the EPP elastic shakedown solution.

We now study the behavior of $f(n,s)$ near $n = 1$. A Taylor series expansion of $f(n,s)$ about $n = 1$ gives

$$f(n,s) = b_0 + b_1(n-1) + O\left((n-1)^2\right) \qquad (4.19)$$

where

$$b_0 = \frac{2(s-1)}{(s+1)\ell n(s)} = 1 - \frac{1}{12}(s-1)^2 + \frac{1}{12}(s-1)^3 + O\left((s-1)^4\right) \quad (4.20)$$

$$b_1 = \frac{(s-1)\left(2\ell n(2) + \ell n(s) - 2\ell n(s+1)\right)}{(s+1)\ell n(s)} = -\frac{1}{8}(s-1)^2 + \frac{1}{8}(s-1)^3 + O\left((s-1)^4\right) \quad (4.21)$$

Hence $f \to b_0$ as $n \to 1$ and Eq. (4.20) shows that $b_0 \le 1$.

From the above analysis, it can be concluded that the damage ratio is one at $n = 1$ and $s = 1$. It decays from one to zero as n and s are increased. A three-dimensional plot of $f(n,s)$ for $1 \le n \le 10$ and $1 \le s \le 10$ is shown in Fig. 4.4.

In summary, under the assumption that the creep rate and damage rate have the same stress dependency, i.e., $n' = n$, it is shown that the damage accumulation over a half-cycle of creep-fatigue straining as determined from an elastic, power-law creep model is bounded by, or less than, the corresponding damage accumulation from the EPP elastic shakedown solution:

$$0 \le \frac{D_c}{D_{epp}} \le 1 \quad (4.22)$$

4.5. EPP Simulation on A617 Creep Fatigue Test

Creep-fatigue tests have been conducted on key-feature test articles of Alloy 617 at 950 °C. The key feature test articles, the so-called Simplified Model Test (SMT) geometries, were developed to mock up the effects of elastic follow-up in reactor pressure boundary components. These data provide an opportunity to assess the conservatism of the EPP creep-fatigue procedure developed for very high temperature applications.

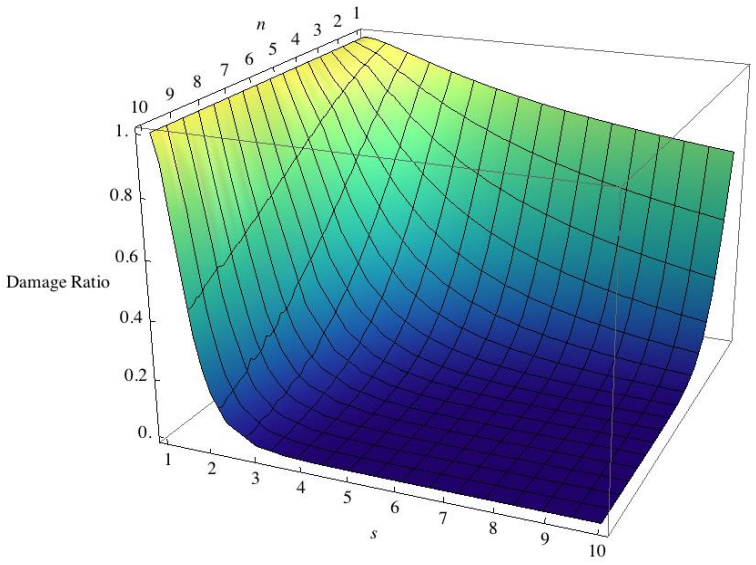

Figure 4.4 A 3D plot of damage ratio as a function of n and s defined in Eqs. (4.2) and (4.15)

4.5.1 EPP Calculation Material Parameters

Young's modulus, E, shear modulus, G, yield strength, S_y, minimum rupture strength, S_r, and pseudo yield stress are material parameters required in the EPP creep-fatigue evaluation procedure. The temperature dependence of E, G and S_y for Alloy 617, given in the units of MPa, are given as

$$E(T_k) = -7.57834280\times10^{-6}T_k^3 - 3.06384586\times10^{-3}T_k^2 - 52.8928996T_k + 227.043102\times10^3 \quad (4.23)$$

$$G(T_k) = -6.14747367\times10^{-6}T_k^3 + 5.87486911\times10^{-3}T_k^2 - 25.2278723T_k + 88.4508513\times10^3 \quad (4.25)$$

$$S_y(T_k) = 240\times\begin{pmatrix} -2.78261712\times10^{-9}T_k^3 + 6.45428719\times10^{-6}T_k^2 \\ -4.96338300\times10^{-3}T_k + 1.98846231 \end{pmatrix} \quad (4.26)$$

where T_k is the absolute temperature in kelvin. The data for S_y were based on testing to high temperature ASTM tensile testing standard.

The correlation for the minimum rupture strength in the units of MPa was given by Eno et al.[67]as,

$$S_r = A^{-1/m}\exp\left(-\frac{Q}{mRT_k}\right)t_r^{1/m} \quad (4.27)$$

where t_r is the rupture time in hours and

$$\begin{gathered} A = \exp(\beta_0), \quad Q = R\beta_1, \quad m = \beta_2 + \beta_3/T_k \\ \beta_0 = -[20.07 + 0.356z]\times\ell n(10), \quad \beta_1 = 37531\times\ell n(10), \quad \beta_2 = 1.20, \quad \beta_3 = -7568 \\ z = 1.645, \quad R = 8.31447215 \end{gathered} \quad (4.28)$$

The pseudo yield stress is given as according to the proposed EPP code case drafted in Appendix A,

$$pseudo\ yield\ stress = lesser\ of\ \left(S_y, K'S_r\right) \tag{4.29}$$

where K' is a design factor with the condition of $K' \leq 1$.

The EPP creep-fatigue code case specifies the use of a pseudo yield stress corresponding to a trial time T_d' that is greater than or equal to the design time t_{design} for the EPP finite element analysis. Eqs. (4.26) and (4.27) can demonstrate that both S_y and S_r are monotonic decreasing as trial time increases. A trial time of $T_d' = t_{design}$ sets the critical condition for assessing whether shakedown to elastic action would take place. That is, if an EPP finite element analysis could not demonstrate shakedown to elastic action when $T_d' = t_{design}$ is used to set the pseudo yield stress, shakedown to elastic action would not take place for any other selected time $T_d' > t_{design}$ to set the pseudo yield stress.

4.5.2 A617 SMT Test and Simulations

There were two A617 SMT test article geometries used in the test program with the dimensions shown in Fig. 4.5 (a) and (b). They differ mainly in the root radius of the transition region. The test data were provided by Y. Wang of the Oak Ridge National Laboratory.

Extensometer probes were mounted on the driver sections of the SMT test article over a gage length of L, as shown in Fig. 4.6. The change in this gage length, ΔL, is controlled according to a prescribed cyclic profile. Another extensometer was mounted on the test section to measure the strain response independently.

Similar to the case of exercising the EPP creep-fatigue procedure to the Alloy 617 standard creep-fatigue test specimens, design times for the case of SMT testing are also

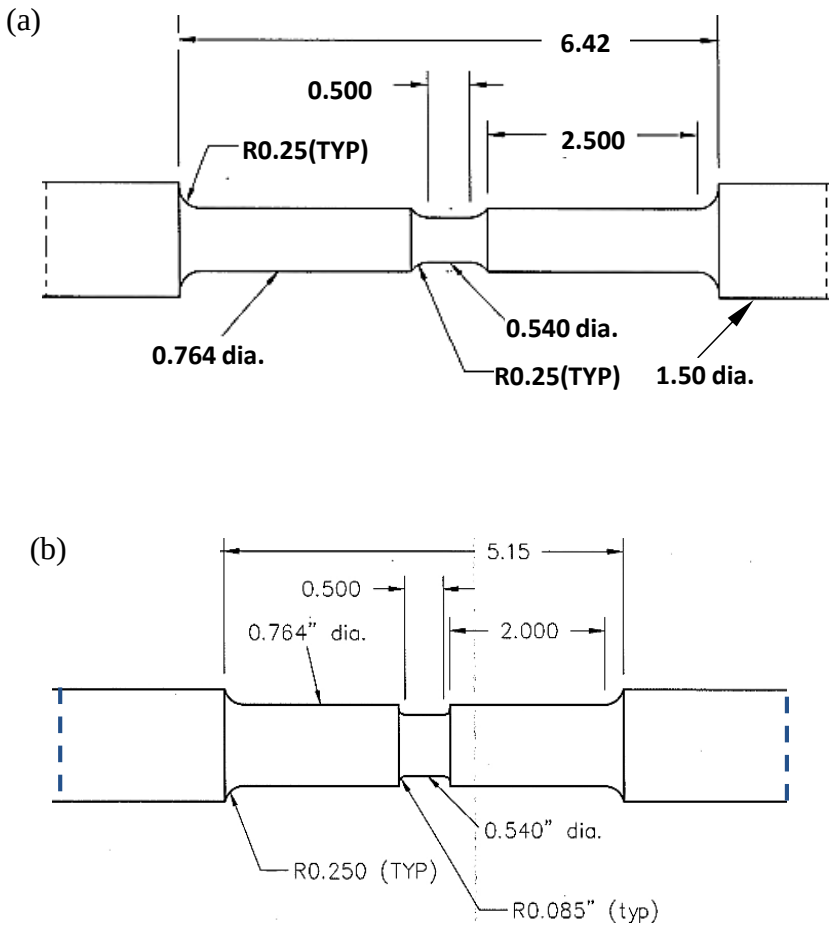

Figure 4.5 Drawing for two SMT specimen test articles. The detail dimensions of (a) Type I geometry and (b) Type II geometry are listed in Table 4.2

.

taken to be the life times of the SMT test articles, and hence they are calculated as time per cycle multiplied by the observed/measured cycles to failure. Such life times calculated for the SMT test cases are shown in the last column of Table 4.2.

As discussed previously, the use of the design time as the trial time for the determination of the pseudo yield stress will provide a critical condition for assessing if an elastic shakedown state can be achieved. Thus using such a choice for the trial times, the pseudo yield stresses were computed from Eqs. (4.23) to (4.29). EPP finite element analyses were then performed for the seven cases listed in Table 4.2. Typical axisymmetric, quarter-symmetric finite element meshes for Types I and II SMT test articles are shown in Fig. 4.8. For each case, finite element analysis for 15 cycles was carried out.

In the first analysis step of the EPP Creep-Fatigue Code Case, an elastic shakedown state is sought from the finite element results. Achieving an elastic shakedown state means that the incremental response for every integration point in the finite element mesh, and every time increment within a cycle, is elastic. Plasticity accumulated in previous cycles is permitted.

There are a number of ways to assess whether an elastic shakedown state is achieved for a cycle from the finite element results. General purpose finite element code ABAQUS was used for the finite element analyses in this study. In ABAQUS, a history variable called AC YIELD is provided for each integration point to store the information on whether an integration point has active plasticity for the current time increment. Such a condition can be detected easily within ABAQUS internal plasticity routines. If plasticity is active for the current time increment, AC YIELD has a value of one, and if not, i.e., the incremental response is elastic, AC YIELD is zero.

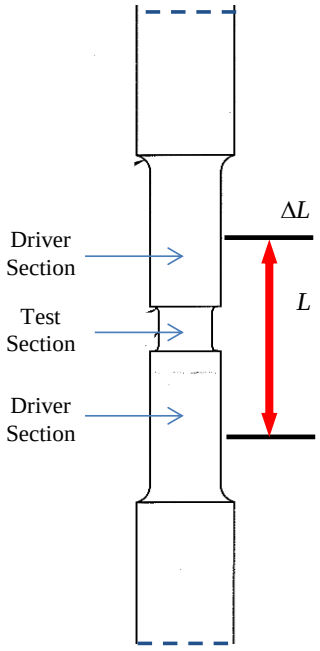

Figure 4.6 Test setup of SMT specimen. Two extensometers are mounted over a gage length of *L*. Another extensometer is mounted at the end

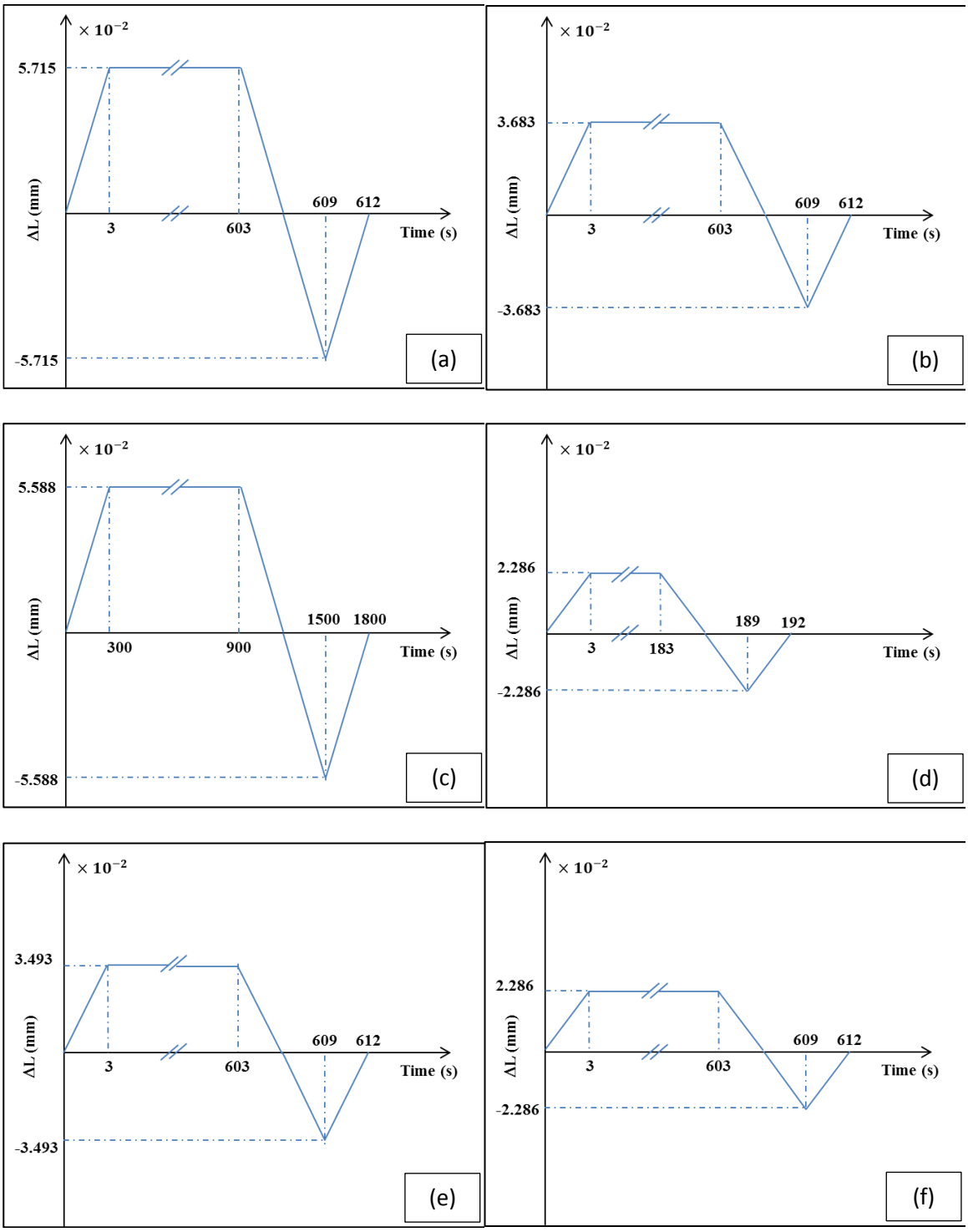

Figure 4.7 Profiles of ΔL for imposing the prescribed displacements over the gage length L for A617. Displacement hold was applied at the maximum tensileΔL value. Cycles were fully reversed.

Table 4.2 SMT test conditions and data for Alloy 617

Case	*Spec. Geom. Type*	*Test Temp. (C)*	*Gage Length, L (mm)*	*ΔL Cyclic Profile (see Fig 4.7)*	*Hold Time (s)*	*Time per Cycle (h)*	*Cycles to Failure*	*Life Time (h)*
1	Type I	950	127.0	(a)	600	0.17	450	76.5
2	Type I	950	127.0	(b)	600	0.17	1000	170.0
3	Type I	950	127.0	(c)	600	0.50	950	475.0
4	Type I	950	127.0	(d)	180	0.05	1050	56.0
5	Type II	950	73.7	(e)	600	0.17	370	62.9
6	Type II	950	73.7	(e)	600	0.17	350	59.5
7	Type II	950	73.7	(f)	600	0.17	940	159.8

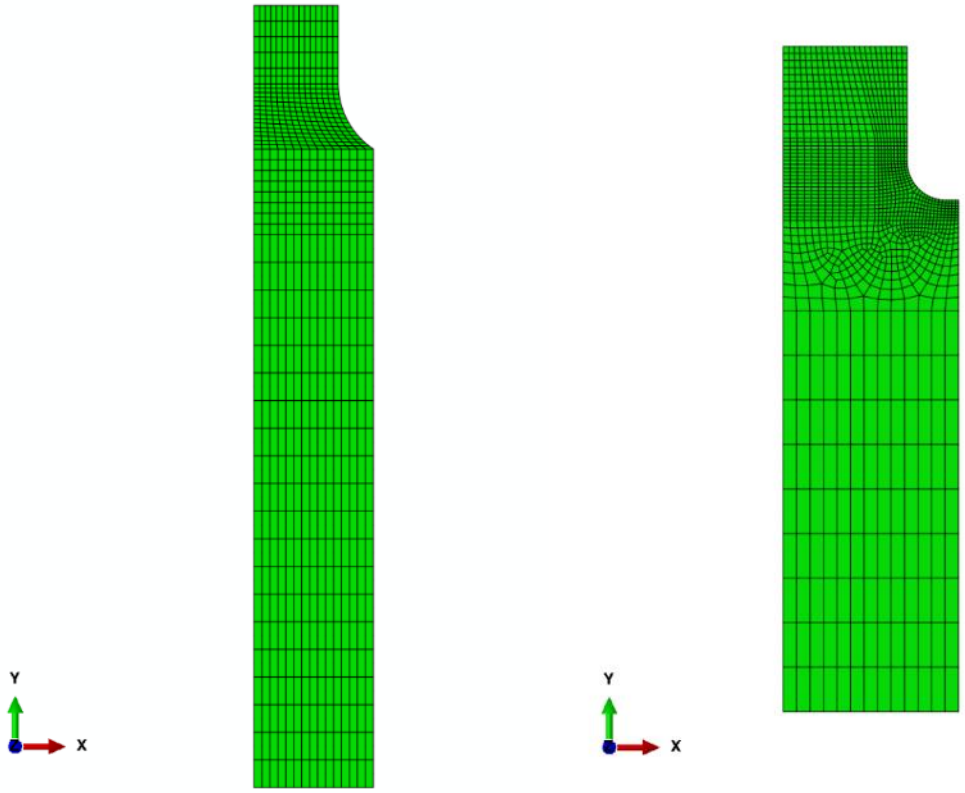

Type I Type II

Figure 4.8. Typical axisymmetric finite element meshes for Type I and Type II SMT test articles

Post-processing scripts were developed to extract the information on AC YIELD for every integration point, every time increment, and every cycle. Using these results, we were not able to demonstrate elastic shakedown for each of the seven SMT test cases. Plots of the AC YIELD values for a selected time increment from the 15^{th} cycle are shown in Fig. 4.9.

Some of the input material parameters for the EPP finite element analyses are given in Table 4.3 for completeness. The EPP Creep-Fatigue Code Case procedure would predict zero allowable creep-fatigue cycles for all these seven cases.

It is noted that we arrived at the same conclusion of not being able to demonstrate elastic shakedown when the design factor was not used (i.e., setting $K' = 1$) in establishing the pseudo yield stress for the EPP finite element analyses.

Application of the Code Case rules to these tests led to the predictions of zero allowable creep-fatigue cycles, and this simply means that designs under these temperatures and strain cycles are not viable.

4.6. EPP Code Case Prediction on Allowable Design Life

In the preceding comparisons, the pseudo yield strength was limited by the tabulated yield strength. The relatively low value of pseudo yield strength prevented elastic shakedown for the high load levels required to achieve relatively short test durations. In a typical component design, the design life would be about three orders of magnitude longer than the test duration and the pseudo yield stress would typically be limited by the creep-rupture strength. Failure to achieve elastic shakedown is a “go, no-go” type criteria and does not provide a quantitative assessment of the design margin.

Figure 4.9 Plots of ABAQUS active plasticity variable AC YIELD for Alloy 167. Essentially grey color indicates active plasticity and blue color denotes incremental elastic response.

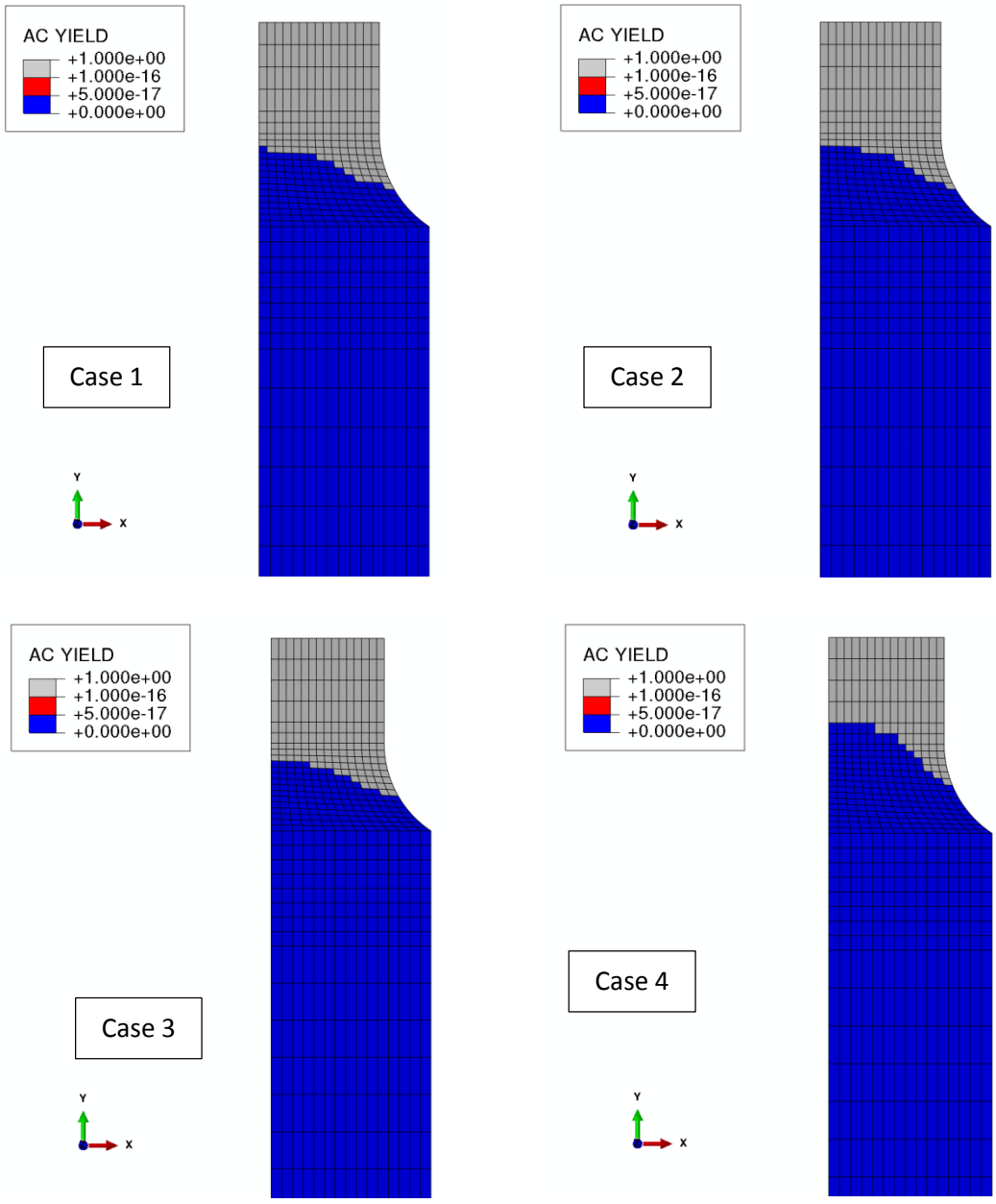

Figure 4.9 continued

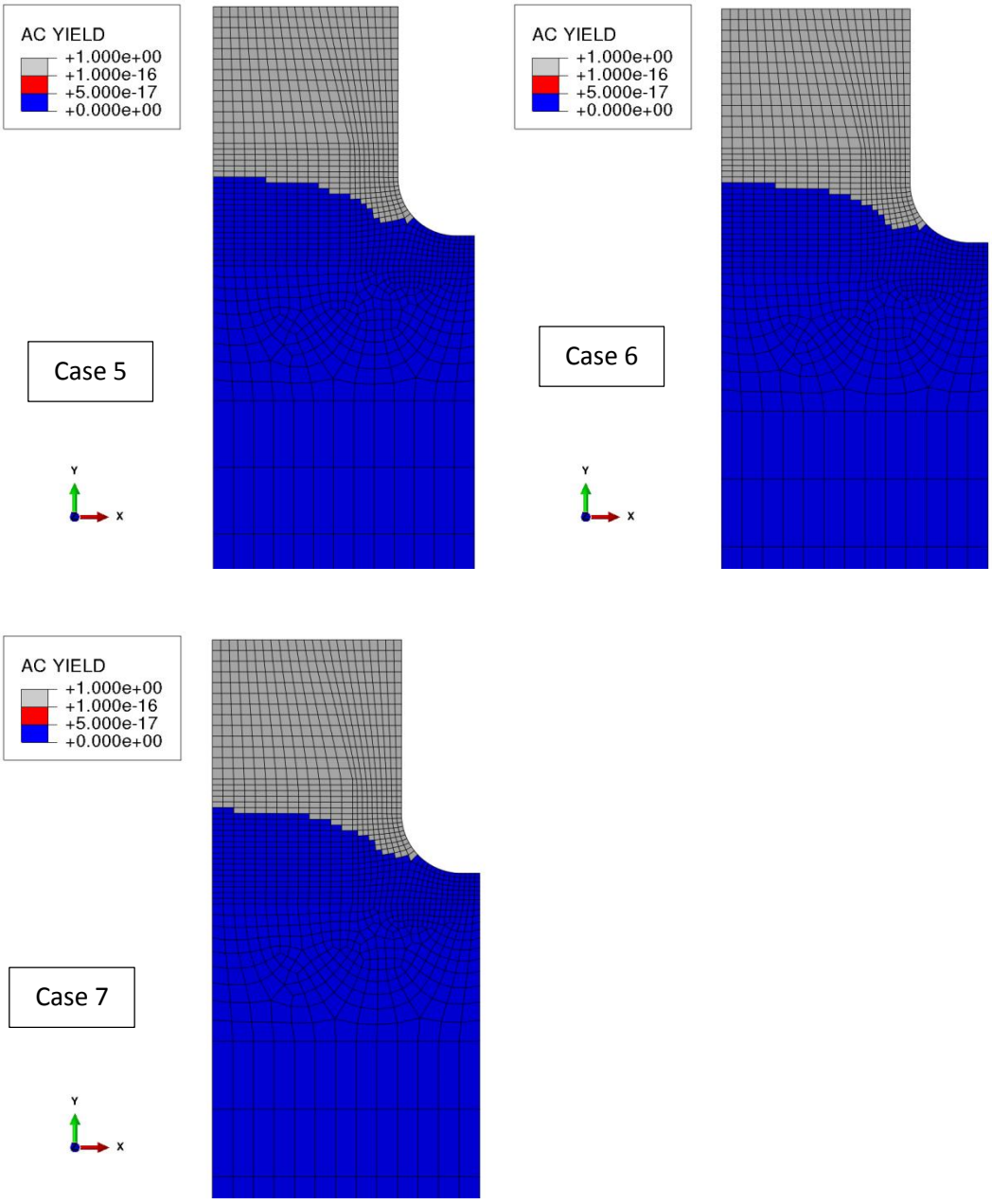

Figure 4.9 continued

To get such a quantitative assessment it is necessary disregard the yield strength and use an extrapolation of the creep-rupture strength to an allowable design life that is shorter, perhaps significantly shorter, than the test duration. As the life is shortened the extrapolated creep rupture stress, and hence the pseudo yield strength, becomes higher. Then, comparing the allowable design life to the measured test life provides a quantitative design margin assessment.

To implement this procedure, three Alloy 617 test cases were selected with varying loading amplitudes as shown in Table 4.4. Given engineering component geometry and mechanical or thermal loading history definition, a series of iterative cyclic E-PP simulations are conducted to find a transition pseudo yield stress point $S_{shakedown}$ ensuring the elastic shakedown condition by tuning the value of pseudo yield stress.

Based on the transition pseudo yield stress $S_{shakedown}$ found in last step, the minimum rupture stress S_r is calculated with dividing $S_{shakedown}$ by the multiply factor K'. From the relationship between S_r and creep rupture time, a required rupture time $t_{rupture}$ corresponding to above S_r value. And given the time period in each loading cycle, cycle number N_1 in period $t_{rupture}$ can be calculated.

Then, calculate the equivalent strain range $\Delta\varepsilon_{equivalent}$ according to NH-T-1431 for each integration point in the simulation at transition pseudo yield stress. The procedure in NH-T-1431 takes the three dimensional effects into consideration to evaluate the maximum equivalent strain range in studied component. The allowable fatigue cycles N_{allow} is calculated according to the maximum equivalent strain range. Then the fatigue damage ratio can be calculated using

Table 4.3 Material parameters used in the EPP finite element analyses for A617

Case	*E (MPa)*	*G (MPa)*	*Sy (MPa)*	*Sr @ Life Time (MPa)*	*PYS @ Life Time, K'=0.9 (MPa)*	*Elastic Shake-Down? (Y/N)*	*Allowable CF Cycles from EPP-CF Code Case*
1	143910	55139	115.7	43.0	38.7	N	0
2	143910	55139	115.7	36.6	33.0	N	0
3	143910	55139	115.7	29.8	26.8	N	0
4	143910	55139	115.7	45.8	41.2	N	0
5	143910	55139	115.7	44.7	40.3	N	0
6	143910	55139	115.7	45.2	40.7	N	0
7	143910	55139	115.7	37.1	33.4	N	0

Table 4.4 Experimental of A617 at 950 ℃ to compare with allowable design life with EPP predictions.

Test Num.	Amplitude (mils)	Holding time (s)	Loading time (s)	Cycle number to failure	Allowed lifetime (hrs)
1	1.8	180	3	1050	56
2	2.9	600	3	1000	170
3	4.5	600	3	450	77

$$D_f = \frac{N_1}{N_{Allow}} \tag{4.30}$$

The allowable creep damage was then determined from the damage diagram (0.1, 0.1 intercept) for the calculated fatigue damage. The allowable time was then determined by multiplying the previously determined required time to rupture by the allowable creep damage fraction. The resulting Alloy 617 and 316H stainless steel design margins are illustrated in Figure 4.10 and 4.11. From the comparison figures, it is evident that there is a significant design margin between the Creep-fatigue Code Case allowable life and the experimentally measured life for both Alloy 617 and 316H stainless steel.

4.7. Y-SMT Specimen Design with Buckling Analysis

To ensure a buckling safety design for YSMT, tubular YSMT and SMT testing, a series of buckling simulations were conducted using ABAQUS finite element analysis software before the sample preparation. The geometric drawings of YSMT, tubular YSMT and SMT are listed in the left column of Fig. 4.12 with enumerated as (a), (b) and (c) respectively. The corresponding numerical models are listed with same order in the right column of Fig. 4.12. In the geometric drawings, some sections are for gripping section, which is not effective for the buckling analysis.

The effective length for buckling analysis is sketched as the section between the red dashed lines.

Two rigid planes are added at both ends of each simulation model with only Y displacement freedom unconstrained for bottom plane and all displacement freedom constrained for top plane. The angular rotations in all directions are constrained to ensure

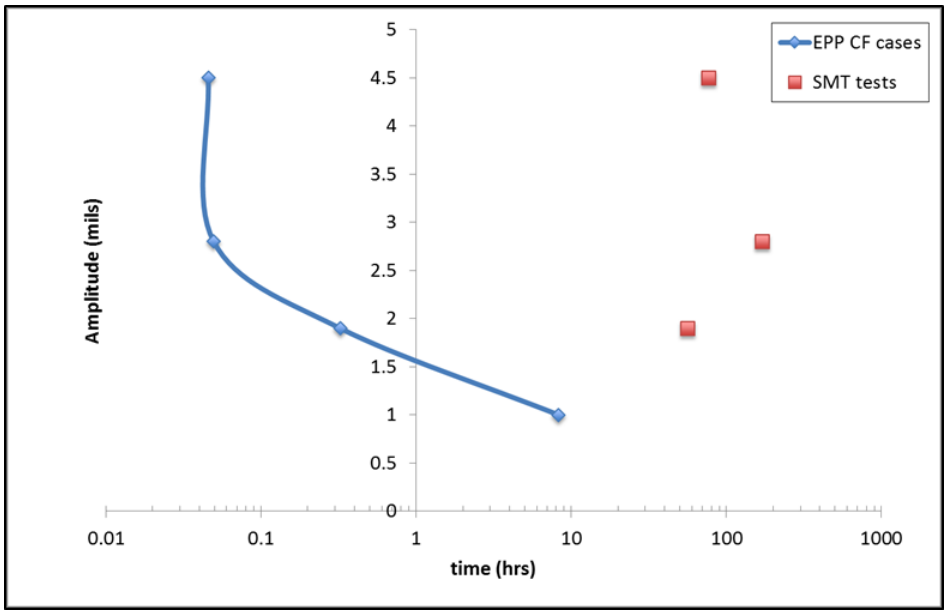

Figure 4.10 EPP creep fatigue code case allowable life prediction comparing to A617 SMT data

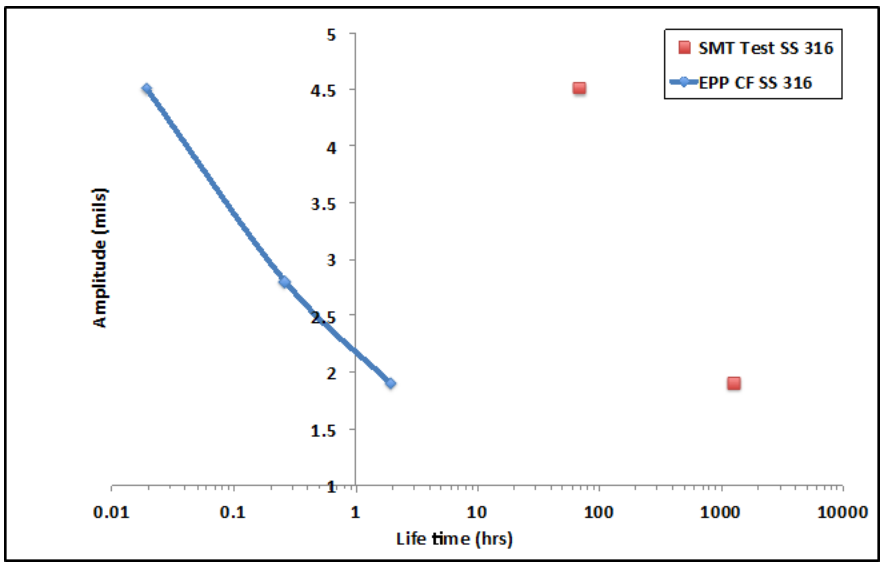

Figure 4.11 EPP creep-fatigue code case allowable loft comparing to 316H stainless steel SMT data which is also a reference material for code case

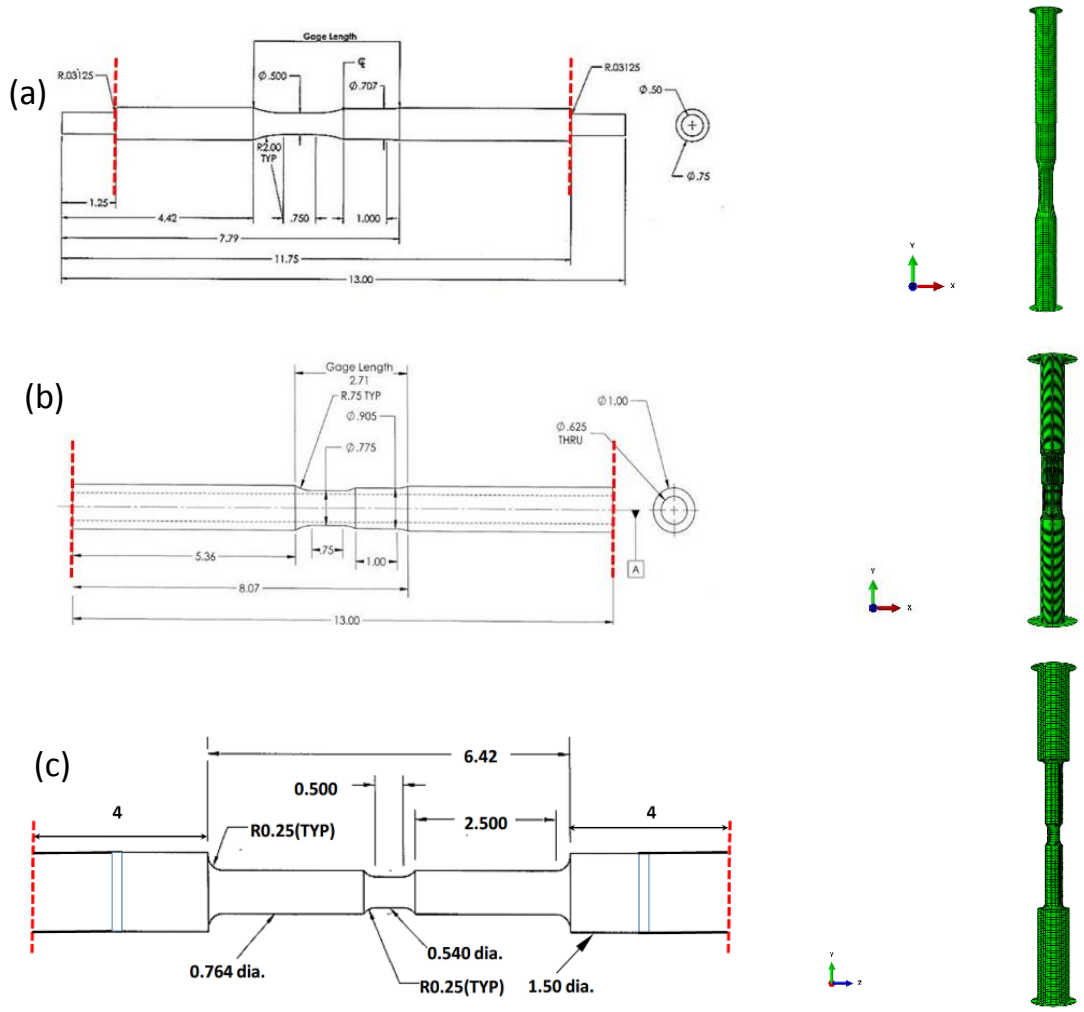

Figure 4.12 (a) YSMT, (b) tubular YSMT and (c) SMT configuration and corresponding FEA model

that an axial loading force can be applied to the model evenly. A unit force is applied to the bottom plane and a buckling analysis step is conducted to get the first modal eigenvalue. The critical loading force is evaluated with the value of unit force timing first modal eigenvalue. The critical buckling loads for three types of geometries are tabulated in Table 4.5. Since stress in testing section is critical in studies, the corresponding stress values are also tabulated. These results are not intended to be a prediction of the absolute load to buckle but, rather, a prediction of the relative buckling resistance since the effects of plasticity and creep were not accounted. Note that the Tubular YSMT specimen has much greater buckling resistance than the original solid bar specimen and somewhat greater resistance than the SMT specimen which did not encounter buckling issues.

Buckling patterns for each model are also shown in Fig. 4.13. Note the triad directions are different for three contour plots, and the directions have been shown at left bottom corners.

4.8. Summary and Conclusions

The goal of this chapter is to illustrate and verify the application of the developed code case to permit evaluation creep-fatigue damage that take advantage of the unique features of elastic-perfectly plastic analysis. Analytic solutions were developed for the example of a creep-fatigue test specimen subjected to cyclic, displacement controlled loading. Using these analytic solutions, it was demonstrated that the creep damage from the EPP solution would be bound the creep damage of steady cyclic solution calculated from a time fraction damage summation using the calculated stress and time history. These detailed analytic solutions for the creep-fatigue test thus demonstrate the conservatism of the EPP code case methodology for a simplified yet realistic example.

Table 4.5 Buckling load and stress values for each model

Model Name	Area (inch^2)	Buckling load (N)	Buckling Stress (ksi)
Solid YSMT	0.196349541	267,000	305.7
Tubular YSMT	0.164933614	715,434	975.1
Standard SMT	0.229022104	946,000	928.6

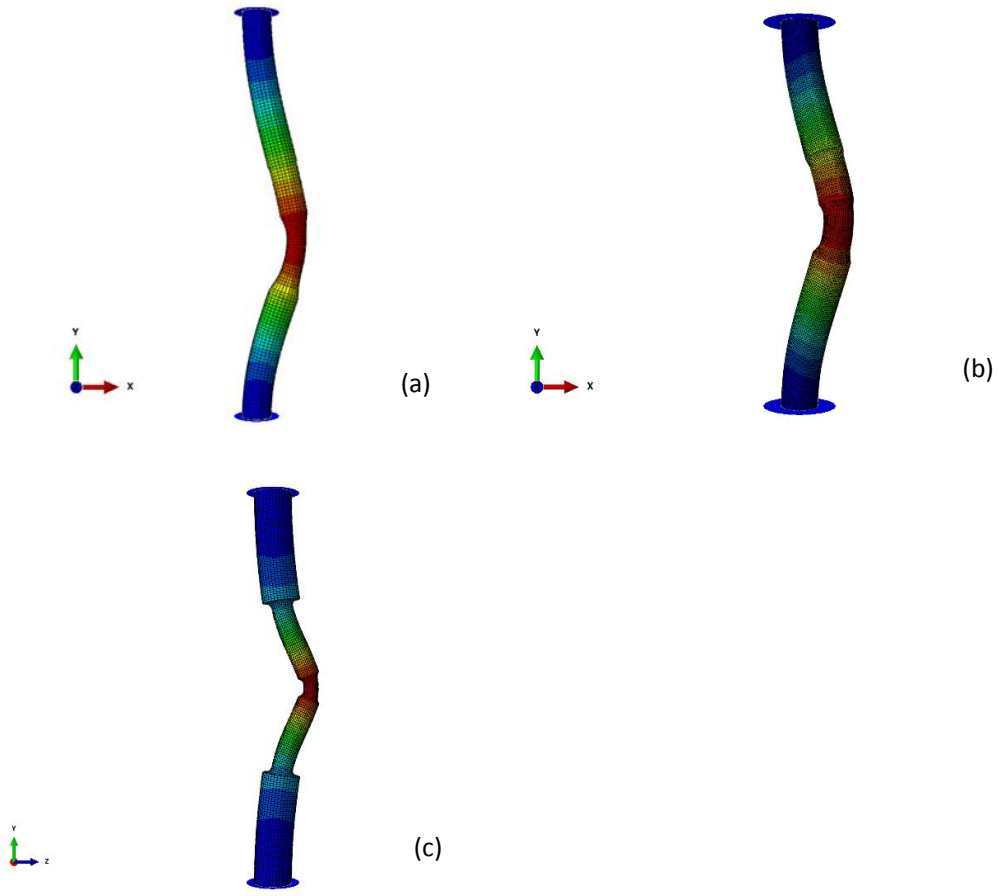

Figure 4.13 Buckling contour plot for (a) YSMT, (b) tubular YSMT and (c) SMT models

With the SMT experimental technique, the evaluation of the implementation of creep-fatigue code case was successful. The implementation requires shakedown to elastic behavior with trial-and-error finite element EPP using a pseudo yield strength based on a creep-rupture strength target life iterated with successively longer values until the combined creep damage and fatigue damage satisfy the damage criteria envelope in Subsection HB, Subpart B. If shakedown cannot be achieved within the allowable creep and fatigue damage envelopes, then the applied loadings are not acceptable. The creep damage calculation is a bounding value applicable to all points in the structure and not a specific value for each location. The creep damage value is combined with the maximum value of the fatigue damage to bound the total damage for the component.

As summarized above, the creep-fatigue code case, (1) can be implemented on a representative component configuration with realistic loading conditions, (2) provides comparable results to current AMSE evaluation procedures at moderate creep temperatures, and, (3) is conservative with respect to the evaluation of creep-damage on experiments with Alloy 617 and 316H stainless steel at very high temperatures.

Chapter 5 Computational Methodology Development in FEA Simulations

5.1. Introduction

With the development of computational resources and utilities, the finite element simulation is more and more powerful and applicable in experiments and practical applications designs and validations. FEA simulations provide a low-cost tool to evaluate the feasibilities of experimental designs, and present designer a comprehensive figure of new test even before they start testing. As a result, FEA is widely adopted in both academic and industrial fields for the studies of structural and material behaviors at different length scales and different disciplines.

As the evolution of FEA applications and increase of modeling size, researchers and users are seeking methods to combine FEA simulation with other utilities for the accomplishment of computational automation and coupling with other algorithms, such as optimization. These procedures have been widely utilized in automotive industries to propose better design for engineering components [68].

During the development of these extended utilities, the automatic post-processing cannot be avoided. The automatic post-processing does not only provide an essential bridge for coupling FEA and optimization tools, but also give the researcher a fast and clear view of simulation results with hands free and error free.

In this section, one FEA assisted experimental study will be presented which is to evaluate the mechanical feasibility of Zr-based bulk metallic glass for arterial stent design

[69]. At last, a computation automation methodology is introduced to present assistive tools which are greatly facilitate my graduate studies.

5.2. Finite Element Modeling in the Evaluation of Zr-base Bulk Metallic Glass in Vascular Stent

Atherosclerosis is caused by plaque build-up in arteries, narrowing or clogging of the blood vessel, and leading to insufficient oxygen and nutrient delivery to the end organs. Adverse events of atherosclerotic disease include heart attack and stroke, both of which can be lethal to patients. Stent technology is employed as a typical treatment for atherosclerosis.

Vascular stents are medical devices typically used to restore the lumen of narrowed or clogged blood vessel. Despite the clinical success of metallic materials in stent-assisted angioplasty, post-surgery complications persist due to the mechanical failures, corrosion, and in-stent restenosis of current stents. To overcome these hurdles, strategies including new designs and surface functionalization have been exercised. In addition, the development of new materials with higher performance and biocompatibility can intrinsically reduce stent failure rates. The present study from our collaboration group demonstrates the advantages of a novel material, named bulk metallic glass (BMG), over the benchmarked 316L stainless steel through experimental methods and computational simulations. It raises the curtain of new research endeavors on BMGs as competitive alternatives for stent applications.

To evaluate the performance of BMG material in stent from a mechanical aspect, finite element model is built up to simulate the stent response responding to the vessel beats pressure. In this model, the structure of stent and blood vessel is described explicitly.

5.2.1 Description of Stent and Blood Vessel Model

Due to complexity of stent model, the CAD model of stent structure and blood vessel is constructed in SolidWorks, a professional advanced CAD package, with the geometric parameters shown in Table 5.1. Considering stent sliding in the vessel was more disastrous, the outer diameter was set to be 0.1mm larger than vessel inner diameter to ensure anchoring. Then, these two geometries were imported into ABAQUS CAE for meshing and setting-up for FEA simulation. The meshes of two model are shown in Fig. 5.1. The axial of two components were aligned, and a local cylinder coordinate system was constructed in order to set up boundary conditions in the later step.

. A 5-parameter third-order Mooney-Rivlin hyperelastic material was designated to simulate the arterial vessel wall with the constitutive model parameters summarized in a previous report [70–73]. The strain-energy density functions for hyperelastic model can be expressed as,

$$W = a_{10}(I_3 - 3) + a_{01}(I_2 - 3) + a_{20}(I_1 - 3)^2 + a_{11}(I_1 - 3)(I_2 - 3) + a_{30}(I_1 - 3)^3 \quad (5.1)$$

where W is the strain energy density functions, a_{ij} are the constitutive model parameter and I_1, I_2, I_3 are the strain invariants.

The ZrAlFeCu BMG (elastic modulus, E = 80 GPa; Poisson's ration, ν = 0.38) and 316L SS (E = 193 GPa, ν = 0.28) were treated as linear elastic materials for comparison simulations. Based on axisymmetric boundary condition, the tangential degree of freedom was constrained on the axial cross sections of stent and vessel segments to only allow radial expansion/compression. Due to the symmetric condition in the axial direction and

Table 5.1 Geometric parameters of the stent-vessel system for FEA

Part	Inner diameter (mm)	Outer diameter (mm)	Length (mm)
Stent	2.90	3.10	3.85
Vessel	3.00	3.40	5.00

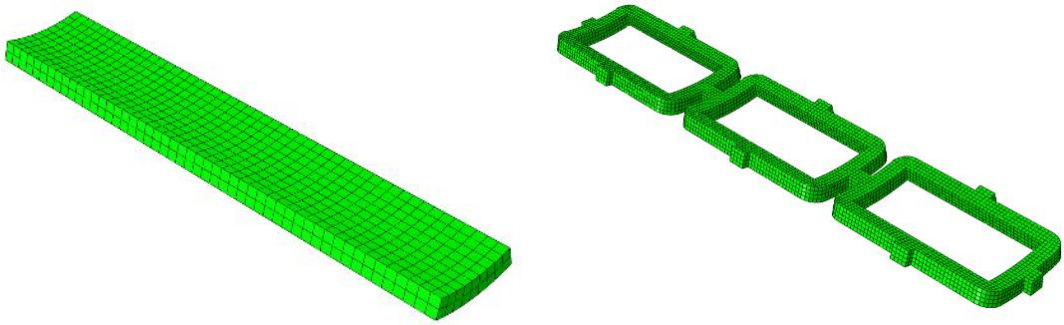

Figure 5.1 Meshing of Vessel wall and stent components

axisymmetry in tangential directions, a ‘‘30°’’ segment of half model (as shown in Fig.5.1) was considered in our simulation. A general contact model with friction coefficient of 0.3 and non-penetrating normal condition was adopted to simulate the interfacial interactions between the two components.

5.2.2 Simulation Steps

In order to simulate the virtual stent anchoring process and stent deformation under physiological loadings with systolic and diastolic pressure, four calculation steps are used in this simulation.

Since there is interference between outer diameter (OD) of stent and inner diameter (ID) of blood vessel, in practical stent planting process, either the vessel will be expanded by a balloon, or the stent will be squeezed in order to transport stent into the vessel. Since in our simulation, both stent and vessel are using reversible material properties, we will just use the vessel expansion in the first step to make the vessel ID is larger than stent OD.

At the beginning of calculation, stent will be placed outside the vessel component. After vessel expansion step, the stent component will be moved along the axis into the vessel until the top end of stent and vessel are aligned. Meanwhile, the vessel will keep in the expansion state.

In the third step, the vessel expansion constrain will be released and vessel material wraps around the stent material. Due to the nonlinearity from the contact and hyperelastic deformation, the convergence is hard to achieve. Thus, calculation stabilization technique will be adopted to improve numerical performance.

After the stent is anchored in the vessel, physiological loadings with systolic and diastolic pressure loads of 50 mmHg and 150 mmHg, respectively, according to American Society for Testing and Materials (ASTM) F2477 will be applied at the vessel outer wall to see the performance of stent.

5.2.3 Simulation Results and Analysis

The distributions of Von Mises stress and maxi- mum principle strain were modeled over a fully expanded stent under applied pressure loads ranging from 50 to 150 mmHg to simulate the diastolic and systolic pressures from the vessel, according to ASTM F2477. The maximum Von Mises stress on the ZrAlFeCu BMG stent was found to be approximately 65 MPa under 150 mmHg pressure loading (Fig. 5.2a and 5.2b), which was similar to the maximum stress of around 67 MPa for 316L SS (Fig. 5.2c). The maximum strain on the ZrAlFeCu BMG stent, as shown in Fig. 5.2d, was predicted to be 7.1×10^{-4}. In contrast, the maximum strain on a 316L SS stent was estimated to be near 3.0×10^{-4} (Fig. 5.2e).

The maximum Von Mises stress on both ZrAlFeCu BMG and 316L SS stent were equivalent and significantly lower than the yield stress and fatigue endurance limit of the Zr-based BMG, indicating the capability of the structure to sustain the physiological loadings and the possibility to further reduce the geometry of the stent. The maximum strains on stents made of both materials were much smaller than their elastic limits, indicating that the deformation of stent with the blood vessel would be constrained within elastic region. However, the strain for Zr-based BMG was found twice as large as that for 316L SS, which suggested that the stent made of ZrAlFeCu BMG could be more flexible and deflected more easily with the blood vessel during the beats. It is noted that we

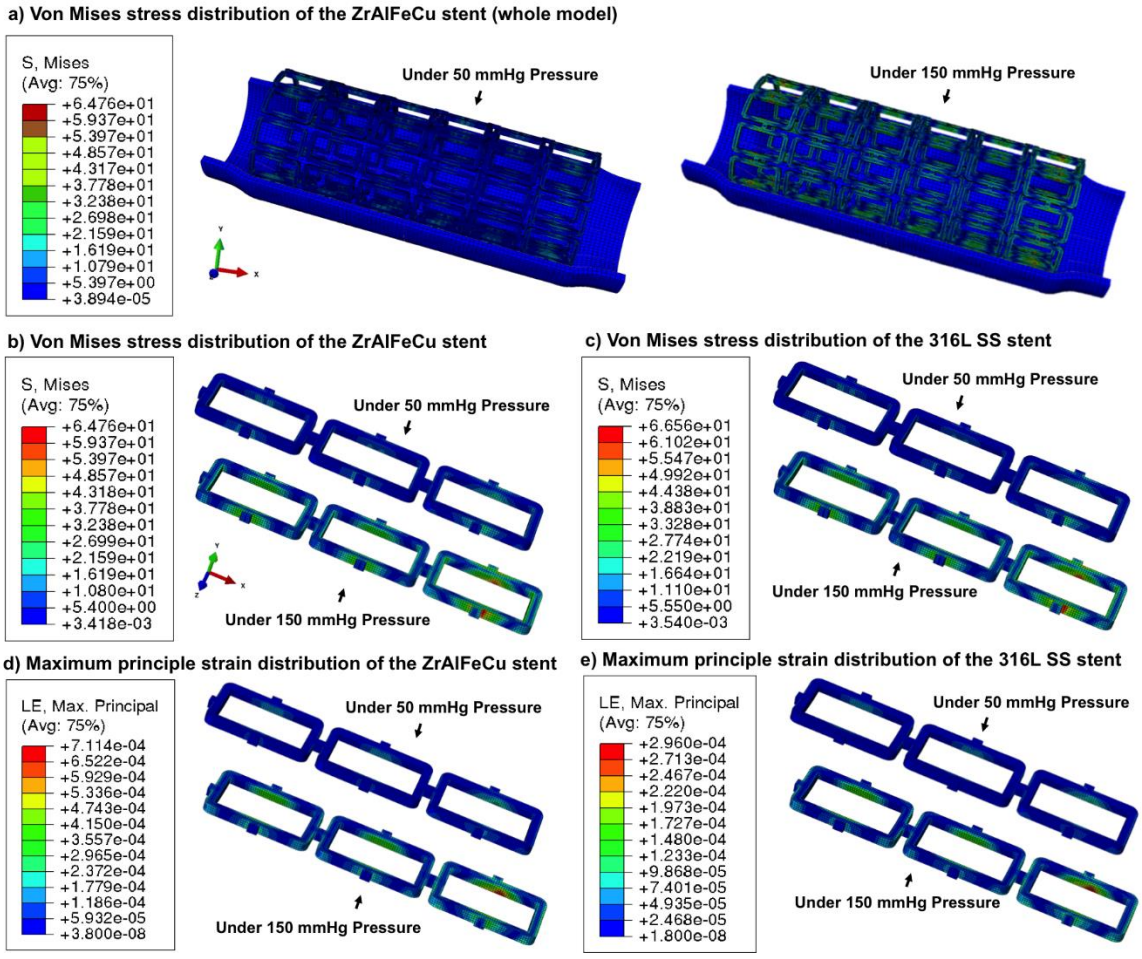

Figure 5.2 Finite element analysis on the Von Mises stress and maximum principle strain distributions of ZrAlFeCu BMG or 316L SS stent under 50 or 150 mmHg pressure load

demonstrated in the present study a specific case on the mechanical responses of a stent configuration, aiming at initially revealing the advantages of Zr-based BMGs. By altering the design parameters, stent with improved performance could be achieved, which requires additional FEA assistances in our future study.

5.3. Development of Simulation Extension Utilities

In this section, the development of simulation extension utilities will be introduced, and one of applications in EPP code case studies will be illustrated as a demonstration of efficiency of such utility. Even though such development will lead to few scientific impacts, it will provide the researcher a "shortcut" to the solution and even realize "impossible" missions. Such advantages will broaden the range of FEA application in the scientific studies.

5.3.1 Scripting Methods

Python script is an interface that ABAQUS provides to fully control simulation by execute the scripts including pre-processing, post processing and job execution. Python itself is a popular programing language famous for powerful functions and high calculation efficiency. Additional to the built-in function in python, ABAQUS add a new function library enable to accomplish ABAQUS specified functions easily. In our studies, python mainly serve in post-processing simulation data and provide solver with certain algorithm.

Except python, shell scripting provides a handy tool to integrate all scripts together and generate a loop of calculation until a certain goal is achieved. It enable batch mode of massive calculation with hands free and error free.

Matlab is a well-known mathematic software which provide more ready-to-use toolbox such as optimization, plots or much more functions. However, it has certain limitations comparing to python script because of its weakness while dealing with big data. So in our studies, Matlab usually work as a plotting tool to export the visualized results.

5.3.2 Examples and Flow Chart

We will take the work in Section 4.6 as an example to illustrate the efficiency and feasibility of extension utility development.

In order to satisfy the EPP code case conditions, a suitable pseudo yield stress is required to make model achieve shakedown condition at each integration point at each increment within a loading cycle. Up to this end, it would be difficult to achieve if this process was done manually. At first, no specific pseudo yield stress was given, so people need to use experience to estimate a rough range of possible values. Then considering the size of the model and integration, it requires numerous work to check yield condition at each integration in the model at all time frames in a loading cycle. This will require at least one week's efforts to finish without any stop.

To make it even worse, while calculating the equivalent strain range to evaluate the fatigue damage of predictions, the current ASME procedure requires using each integration point as a reference point. With a certain reference point, the strain range will be calculated according to the AMSE algorithm. The detailed procedure is as the following,

(1) Calculate all the strain components $\left(\varepsilon_{xi}, \varepsilon_{yi}, \varepsilon_{zi}, \gamma_{xyi}, \gamma_{yzi}, \gamma_{xzi}\right)$ for each point, i, for each calculation time during a complete loading cycle.

(2) Set the reference time to a random time increment at first, and get the stress components at this reference time as $\left(\varepsilon_{xo}, \varepsilon_{yo}, \varepsilon_{zo}, \gamma_{xyo}, \gamma_{yzo}, \gamma_{xzo}\right)$

(3) For each point in time, i, calculate the history of the change in each strain components by subtracting the values at the time o to have $\Delta\varepsilon_{xi} = \varepsilon_{xi} - \varepsilon_{xo}, \Delta\varepsilon_{yi} = \varepsilon_{yi} - \varepsilon_{yo}$, etc.

(4) Calculate the equivalent strain range for each point with the reference time point o,

$$\Delta\varepsilon_{equiv,i} = \frac{\sqrt{2}}{2(1+\upsilon)}\left[\begin{array}{c}\left(\Delta\varepsilon_{xi} - \Delta\varepsilon_{yi}\right)^2 + \left(\Delta\varepsilon_{xi} - \Delta\varepsilon_{zi}\right)^2 + \left(\Delta\varepsilon_{yi} - \Delta\varepsilon_{zi}\right)^2 \\ + \frac{3}{2}\left(\Delta\gamma_{xyi}^2 + \Delta\gamma_{yzi}^2 + \Delta\gamma_{xzi}^2\right)\end{array}\right]^{1/2} \quad (5.1)$$

(5) Choose a different reference time point, and repeat the Step (2) – (4) to and get the equivalent strain range with different reference time point.

(6) Choose the maximum value of equivalent range out of all integration points with different reference time point.

Suppose there are N integration points in total in the model and K increment in each cycle, the calculation of equivalent strain will be repeated by $N^2 \times K$ times. This work load requires the use of comprised method to evaluate equivalent strain range. However, with the development of utilities, all these works will be done by computer automatically. User will get a clear list of report and the final results without manpower.

The calculation flow chart is shown in Fig. 5.3. Shell script is the outer platform providing a loop logic and driving different scripts.

At the beginning of the calculation, a wide range of pseudo yield stress is given. It has been pointed out in Section 4 that in order to achieve the elastic shakedown, a higher pseudo yield stress is required. So the upper limit of PYS range will be checked if it is larger enough to achieve elastic shakedown. Replace the yield stress in ABAQUS input file with upper limit, and delivery this job to ABAQUS for simulation.

After the first job is done, the post-processing python will be called to check the shakedown condition. If shakedown judgement returns a negative value, the whole process will be terminated and suggests user to use a higher upper value. Otherwise, a "for" loop will start with initial $PYS_1 = \left(\sigma_{upper} + \sigma_{lower}\right)/2$ and proceed to ABAQUS, post-processing script to judge the shakedown condition. Within the "for" loop, a bi-section algorithm to seek the solution with a sketch illustrated in Fig. 5.4. While the shell script is executed, an output file including the PYS value at each iteration will be outputted. By checking the convergence of PYS values, it can be told that whether a reasonable PYS is attained at the end of 20 iterations.

After 20 iterations finish, a python script is called to calculate the equivalent strain range as described before using last elastic shakedown's simulation results. With the correlation between strain range and fatigue life, another python solver is called to solve the correlation equations at different temperature range in [74] with the following correlation equation at current testing temperature 950 ℃,

$$\Delta\varepsilon_{total} = 68\left(N_f\right)^{-0.76} + 0.47\left(N_f\right)^{-0.08} \tag{5.2}$$

With the calculated allowable fatigue cycles, the fatigue damage can be calculated by comparing with loading cycles from SMT tests. The predicted allowed design life will be calculated and plotted in the comparison plot accordingly by calling a Matlab script automatically. The comparison results have been shown in Fig. 4.10 and Fig 4.1.

5.4. Summary and Conclusion

In this chapter, several extended studies using numerical method are illustrated in this chapter. A numerical model was constructed for blood vessel and stent explicitly and use

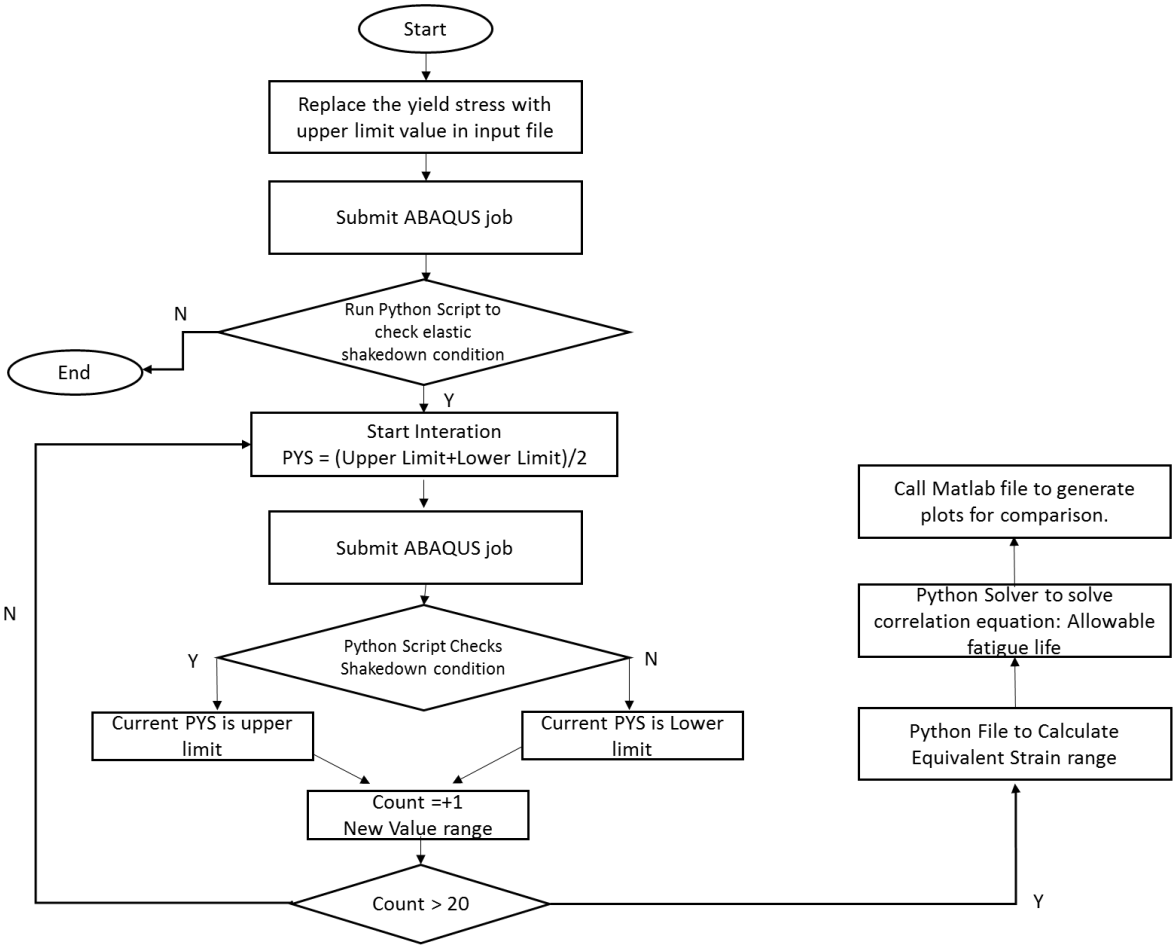

Figure 5.3 Flow chart of script driving calculation

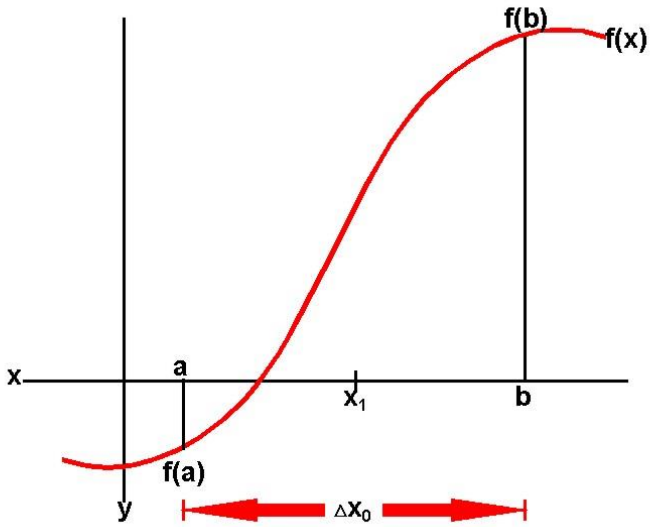

Figure 5.4 Illustration of bi-section algorithm embedded in “for” loop

proper material properties to simulate the mechanical response of vascular stent under cyclic systolic and diastolic pressure, in order to validate the feasibility of Zr-based BMG in stent applications.

Additionally, a numerical procedure is presented here with scheme illustrated. This utility provides a delicate work frame driving ABAQUS simulation and post processing automatically. With the benefits of this utility, we can finish a series of calculation merely using computer without human interactions.

Chapter 6 Conclusions and Perspectives

As concluding remarks, the objective of this dissertation work is to understand the deformation mechanism and evaluate damage of structural materials with computational methods at different length scales. To achieve this goal, finite element simulations with crystal plasticity theory were performed to investigate the microscopic deformation of polycrystalline materials by comparing with advanced diffraction measurements. Cohesive zone model was adopted to study the coupling effect of impurity transportation and anisotropic deformation. At macroscopic level, elastic perfect plastic model is developed and validated to evaluate creep fatigue damage with the support of SMT experimental technique. The summary of thesis work is as follows,

(1) Intergranular and interphase interactions in DP steel and multilayered steel are investigated by crystal plasticity finite element simulations. Based on the characteristic microstructures of dual-phase and multilayered steels, two polycrystalline aggregate models are constructed to simulate the microscopic lattice strain evolution of these materials during uniaxial tensile tests. Microstructural models are constructed from experimentally observed features such as the locations of martensite phase in DP steel and volume fraction of constituent phases. By comparing the lattice strain evolution from crystal plasticity finite element simulations with advanced in situ diffraction measurements in literature, this study investigates the correlations between the material microstructure and the micromechanical interactions on the intergranular and interphase levels. Three deformation stages are identified on the lattice strain evolution with respect to the applied stress. It is found that although the applied stress will be ultimately

accommodated by the hard phase and hard grain families, the sequence of the stress partitioning on grain and phase levels can be altered by microstructural designs. The dependence of the effectiveness of stress transfer on the microstructure is investigated by the comparisons of a fictitious DP model (with austenite and martensite) and the multilayered steel. The enhanced stress transfer to the martensite phase will help delay localized failure such as martensite phase fracture and interface debonding.

(2) A diffusion-coupled cohesive zone model (CZM) is proposed to accomplish the simulation of fully stress coupled diffusion process along the grain boundaries and mechanical response of grain boundary sliding and separation. This numerical model considers both diffusion affected by pressure gradient and degradation of grain boundary interfacial strength induced by impurity corrosion. The numerical scheme and techniques are presented to demonstrate the computational capability for different types of boundary condition. The diffusion-coupled CZM is combined with crystal plasticity finite element model (CPFEM) to simulate intergranular fracture of polycrystalline material under corrosive environment. Significant heterogeneity of stress field and inelastic deformation is observed at grain boundaries and junction points. The competition of grain-boundary diffusion and grain boundary mechanical response dominates intergranular fracture at different periods. The intergranular damage mechanism has been revealed for the material subjected to environmental corrosion and three types of damage modes are revealed with different degradation factors.

(3) Based on the energy bounding theorems, a simplified method by taking advantage of the unique features of elastic perfect plastic analysis is developed to permit evaluation of creep-fatigue damage. An analytical derivation is developed for an example standard creep-fatigue test specimen subjected to cyclic, displacement controlled loading, in order to demonstrate the damage bounding of EPP solution. These analytic solution for example creep-fatigue test demonstrate the conservation of the EPP code case methodology. Then, the creep-fatigue code case is applied to an example problem representative of a realistic components with realistic loading conditions. With the comparison of SMT tests with A617 and 316H stainless steel at elevated temperature, this creep-fatigue methodology has been proved be conservative and allowable design life is compared with test data with a design margin.

(4) The FEA simulation methods were also adopted in practical applications to validate the material properties and feasibility in stent design and also test specimen buckling analysis. These simulations provide the prediction of material behavior under different loading condition and instruct the design of engineering components and experimental design.

(5) With the utility developed to pre- and post-process data, FEA simulation is more suitable with handling massive simulation data, and present a clear prediction trend. A utility package is developed to demonstrate the efficiency and calculation feasibility of developed automation solution seeking procedure based on FEA simulation.

This dissertation presents a couple of original works on computational methods for structural material simulations. Although many insightful findings are obtained, these works can be further extended along the following lines:

(1) The current dual-phase crystal plastic model can be utilized in other advanced dual phase materials to study their microstructure properties such as grain orientation rotation pattern due to the shock impact.

(2) As mentioned above, the diffusion coupled cohesive zone model in this study still has limitation to study a comparable simulation with real experimental observation. Technical efforts are needed for applying developed CZM code in more general cases consisting of a larger number of grains and complicated grain boundary configurations. Sophisticated model descriptions corresponding to diffusion degradation and mechanical response needs to be developed for specific conditions

(3) The EPP creep-fatigue methodology needs improvement with specifying the applicable conditions in order to reduce the design margin for prediction.

List of References

[1] Chen, P., Ghassemi-Armaki, H., Kumar, S., Bower, A., Bhat, S., and Sadagopan, S., 2014, "Microscale-calibrated modeling of the deformation response of dual-phase steels," Acta Mater., **65**, pp. 133–149.

[2] Jia, N., Cong, Z. H., Sun, X., Cheng, S., Nie, Z. H., Ren, Y., Liaw, P. K., and Wang, Y. D., 2009, "An in situ high-energy X-ray diffraction study of micromechanical behavior of multiple phases in advanced high-strength steels," Acta Mater., **57**(13), pp. 3965–3977.

[3] Wright, J. K., Carroll, L. J., Simpson, J. a., and Wright, R. N., 2013, "Low Cycle Fatigue of Alloy 617 at 850 °C and 950 °C," J. Eng. Mater. Technol., **135**(3), p. 031005.

[4] Zheng, L., 2011, "Micromechanical Studies of Intergranular Strain and Lattice Misorientation Fields and Comparisons to Advanced Diffraction Measurements."

[5] Peirce, D., Asaro, R. J., Needleman, A., and Park, A., 1983, "Overview: Material Rate Dependence and Localized Deformation in Crystalline Solids," Acta Mater., **31**(12), pp. 1951–1976.

[6] Krajewski, P. E., Hector, L. G. J., Qi, Y., Mishra, R. K., Sachdev, A. K., Bower, A. F., and Curtin, W. A., 2011, "Atoms to autos : a multiscale approach to modeling Aluminum deformation," Jom, **63**(11), pp. 24–32.

[7] Zheng, L. L., Gao, Y. F., Lee, S. Y., Barabash, R. I., Lee, J. H., and Liaw, P. K., 2011, "Intergranular strain evolution near fatigue crack tips in polycrystalline metals," J. Mech. Phys. Solids, **59**(11), pp. 2307–2322.

[8] Huang, S., Gao, Y., An, K., Zheng, L., Wu, W., Teng, Z., and Liaw, P. K., 2015, "Deformation mechanisms in a precipitation-strengthened ferritic superalloy revealed by in situ neutron diffraction studies at elevated temperatures," Acta Mater., **83**, pp. 137–148.

[9] Zheng, L. L., Gao, Y. F., Wang, Y. D., Stoica, a. D., An, K., and Wang, X. L., 2013, "Grain orientation dependence of lattice strains and intergranular damage rates in polycrystals under cyclic loading," Scr. Mater., **68**(5), pp. 265–268.

[10] Chuang, C., 2013, "High Energy Synchrotron X-ray Study of Fatigue Damage in Amorphous and Polycrystalline Engineering Alloys," University of Tennessee.

[11] Huang, Y., 1991, "A user-material subroutine incorporating single crystal plasticity in the ABAQUS finite element program," Mech. Rep. 179, Div. Engienering Appl. Sci. Harvard Univ.

[12] Gurtin, M. E., 2000, "On the plasticity of single crystals: free energy, microforces, plastic-strain gradients," J. Mech. Phys. Solids, **48**(5), pp. 989–1036.

[13] Ojima, M., Inoue, J., Nambu, S., Xu, P., Akita, K., Suzuki, H., and Koseki, T., 2012, "Stress partitioning behavior of multilayered steels during tensile deformation measured by in situ neutron diffraction," Scr. Mater., **66**(3-4), pp. 139–142.

[14] Elena Garlea, 2008, "Fundamental Deformation Micromechanics in a Zircaloy-4 Alloy and the Hydrogen Effects on its Microstructure, Internal Stresses, and Fatigue Behavior.," University of Tennessee, Knoxville.

[15] Faulkner, R. G., 2005, "Grain boundary segregation and fracture," Zeitschrift für Met., **96**(10), pp. 1213–1218.

[16] Haftbaradaran, H., Song, J., Curtin, W. a., and Gao, H., 2011, "Continuum and atomistic models of strongly coupled diffusion, stress, and solute concentration," J. Power Sources, **196**(1), pp. 361–370.

[17] Olden, V., Thaulow, C., Johnsen, R., Østby, E., and Berstad, T., 2008, "Application of hydrogen influenced cohesive laws in the prediction of hydrogen induced stress cracking in 25%Cr duplex stainless steel," Eng. Fract. Mech., **75**(8), pp. 2333–2351.

[18] Raykar, N. R., Maiti, S. K., Singh Raman, R. K., and Aryan, S., 2013, "Study of hydrogen concentration dependent growth of external annular crack in round tensile specimen using cohesive zone model," Eng. Fract. Mech., **106**, pp. 49–66.

[19] Scheider, I., Pfuff, M., and Dietzel, W., 2008, "Simulation of hydrogen assisted stress corrosion cracking using the cohesive model," Eng. Fract. Mech., **75**(15), pp. 4283–4291.

[20] Shanati, S., Ellis, N. S., Randall, T. J., and Marshall, J. M., 1995, "Coupled diffusion and stress by the finite element method," Appl. Math. Model., **19**(2), pp. 87–94.

[21] Karabela, a., Zhao, L. G., Lin, B., Tong, J., and Hardy, M. C., 2013, "Oxygen diffusion and crack growth for a nickel-based superalloy under fatigue-oxidation

conditions," Mater. Sci. Eng. A, **567**, pp. 46–57.

[22] Carter, P., Jetter, R. I., and T.-L., S., 2014, "Verification of elastic-perfectly plastic methods for evaluation of strain limits-analytical comparisons," Proceedings of the ASME 2014 Pressure Vessels & Piping Conference, Anaheim, California, USA.

[23] Carter, P., Jetter, R., and Sham, T. L., 2012, "Application of Elastic-Perfectly Plastic Cyclic Analysis to Assessment of Creep Strain," ASME Pap. No. PVP2012-78082.

[24] Wang, Y., and Jetter, R. I., 2013, Progress report on the development of test procedure for the two-bar thermal ratcheting experiment for Alloy 617 Prepared by.

[25] Wang, Y., Tianlei, L., Sham, T.-L. (Sam), and Jetter, R. I., 2013, "Evaluation of Creep-Fatigue Damage Based on Simplified Model Test," Proceedings of the ASME 2013 Pressure Vessels & Piping Division Conference, p. 11.

[26] Barabash, R. I., Barabash, O. M., Ojima, M., Yu, Z., Inoue, J., Nambu, S., Koseki, T., Xu, R., and Feng, Z., 2013, "Interphase Strain Gradients in Multilayered Steel Composite from Microdiffraction," Metall. Mater. Trans. A, **45**(1), pp. 98–108.

[27] Kim, D. H., Kim, S.-J., Kim, S.-H., Rollett, A. D., Oh, K. H., and Han, H. N., 2011, "Microtexture development during equibiaxial tensile deformation in monolithic and dual phase steels," Acta Mater., **59**(14), pp. 5462–5471.

[28] Koseki, T., Inoue, J., and Nambu, S., 2014, "Development of Multilayer Steels for Improved Combinations of High Strength and High Ductility," Mater. Trans., **55**(2), pp. 227–237.

[29] Ohashi, T., Roslan, L., Takahashi, K., Shimokawa, T., Tanaka, M., and Higashida, K., 2013, "A multiscale approach for the deformation mechanism in pearlite microstructure: Numerical evaluation of elasto-plastic deformation in fine lamellar structures," Mater. Sci. Eng. A, **588**, pp. 214–220.

[30] Wong, S. L., and Dawson, P. R., 2010, "Influence of directional strength-to-stiffness on the elastic–plastic transition of fcc polycrystals under uniaxial tensile loading," Acta Mater., **58**(5), pp. 1658–1678.

[31] Clausen, B., Lorentzen, T., and Leffers, T., 1998, "Self-consistent Modelling of the Plastic Deformation of F.C.C. Polycrystals and its Implications for Diffraction

Measurements of Internal Stresses," **46**(9).

[32] Jia, N., Lin Peng, R., Wang, Y. D., Johansson, S., and Liaw, P. K., 2008, "Micromechanical behavior and texture evolution of duplex stainless steel studied by neutron diffraction and self-consistent modeling," Acta Mater., **56**(4), pp. 782–793.

[33] Saylor, D., Fridy, J., El-Dasher, B., Jung, K.-Y., and Rollett, A., 2004, "Statistically representative three-dimensional microstructures based on orthogonal observation sections," Metall. Mater. Trans. A, **35**(7), pp. 1969–1979.

[34] Tanaka, Y., Kishimoto, S., Yin, F., Kobayshi, M., Tomimatsu, T., and Kagawa, K., 2009, "Multi-scale deformation behavior for multi-layer steel by in-situ FE-SEM," Fourth Int. Conf. Exp. Mech., **7522**, p. 7520N–1.

[35] Feng, K., Cai, X., Li, Z., and Chu, P. K., 2012, "Improved corrosion resistance of stainless steel 316L by Ti ion implantation," Mater. Lett., **68**, pp. 450–452.

[36] Barabash, R. I., Bei, H., Gao, Y. F., and Ice, G. E., 2011, "Interface strength in NiAl–Mo composites from 3-D X-ray microdiffraction," Scr. Mater., **64**(9), pp. 900–903.

[37] Busso, E. P., Lin, J., Sakurai, S., and Nakayama, M., 2001, "A MECHANISTIC STUDY OF OXIDATION-INDUCED DEGRADATION IN A PLASMA-SPRAYED THERMAL BARRIER COATING SYSTEM . PART I : MODEL FORMULATION," **49**, pp. 1515–1528.

[38] Dumoulin, S., Busso†, E. P., O'Dowd, N. P., and Allen, D., 2003, "A multiscale approach for coupled phenomena in fcc materials at high temperatures," Philos. Mag., **83**(31-34), pp. 3895–3916.

[39] Zhao, L. G., Tong, J., and Hardy, M. C., 2010, "Prediction of crack growth in a nickel-based superalloy under fatigue-oxidation conditions," Eng. Fract. Mech., **77**(6), pp. 925–938.

[40] Sato, a., Chiu, Y.-L., and Reed, R. C., 2011, "Oxidation of nickel-based single-crystal superalloys for industrial gas turbine applications," Acta Mater., **59**(1), pp. 225–240.

[41] Bhandakkar, T. K., and Gao, H., 2010, "Cohesive modeling of crack nucleation

under diffusion induced stresses in a thin strip: Implications on the critical size for flaw tolerant battery electrodes," Int. J. Solids Struct., **47**(10), pp. 1424–1434.

[42] Olden, V., Thaulow, C., and Johnsen, R., 2008, "Modelling of hydrogen diffusion and hydrogen induced cracking in supermartensitic and duplex stainless steels," Mater. Des., **29**(10), pp. 1934–1948.

[43] Olden, V., Thaulow, C., Johnsen, R., Østby, E., and Berstad, T., 2009, "Influence of hydrogen from cathodic protection on the fracture susceptibility of 25%Cr duplex stainless steel – Constant load SENT testing and FE-modelling using hydrogen influenced cohesive zone elements," Eng. Fract. Mech., **76**(7), pp. 827–844.

[44] Fisher, J. C., 1951, "Calculation of Diffusion Penetration Curves for Surface and Grain Boundary Diffusion," J. Appl. Phys., **22**(1).

[45] Whipple, R. T. P., 1954, "CXXXVIII. Concentration contours in grain boundary diffusion," London, Edinburgh, Dublin Philos. Mag. J. Sci., **45**(371), pp. 1225–1236.

[46] Herzig, C., and Mishin, Y., 2005, "Grain Boundary Diffusion in Metals," Diffusion in Condensed Matter SE - 8, P. Heitjans, and J. Kärger, eds., Springer Berlin Heidelberg, pp. 337–366.

[47] Bower, A. F., and Wininger, E., 2004, "A two-dimensional finite element method for simulating the constitutive response and microstructure of polycrystals during high temperature plastic deformation," J. Mech. Phys. Solids, **52**(6), pp. 1289–1317.

[48] Wei, Y. J., and Anand, L., 2004, "Grain-boundary sliding and separation in polycrystalline metals: application to nanocrystalline fcc metals," J. Mech. Phys. Solids, **52**(11), pp. 2587–2616.

[49] Xu, X.-P., and Needleman, A., 1994, "Numerical simulations of fast crack growth in brittle solids," J. Mech. Phys. Solids, **42**(9), pp. 1397–1434.

[50] Yu, C., Huang, C., and Chen, C., 2013, "A micromechanics study of competing mechanisms for creep fracture of zirconium diboride polycrystals," J. Eur. …, **33**(10), pp. 1625–1637.

[51] Cabet, C., and Duprey, B., 2010, "Long term high-temperature oxidation of Alloys for intermediate heat exchangers," Proceedings of the 2010 International Congress

on Advances in Nuclear Power Plants-ICAPP'10.

[52] Materiaux, C. De, Cnrs, U. R. A., Paris, M. De, France, E. C., and Materiaux, C., 1992, "Intergranular crack tip oxidation mechanism in a nickel-based superalloy," Mater. Sci. Eng. A, **154**, pp. 21–28.

[53] Pu, C., and Gao, Y., 2015, "Crystal Plasticity Analysis of Stress Partitioning Mechanisms and Their Microstructural Dependence in Advanced Steels," J. Appl. Mech., **82**(3), p. 031003.

[54] Jia, H. L., Zheng, L. L., Li, W. D., Li, N., Qiao, J. W., Wang, G. Y., Ren, Y., Liaw, P. K., and Gao, Y., 2015, "Insights from the Lattice-Strain Evolution on Deformation Mechanisms in Metallic-Glass-Matrix Composites," Metall. Mater. Trans. A.

[55] 2012, ABAQUS Analysis User Manual (v6.12), Systèmes, Dassault, Providence, RI, USA.

[56] Zhao, L., Odowd, N., and Busso, E., 2006, "A coupled kinetic-constitutive approach to the study of high temperature crack initiation in single crystal nickel-base superalloys☆," J. Mech. Phys. Solids, **54**(2), pp. 288–309.

[57] Zhao, L., and Tong, J., 2008, "A viscoplastic study of crack-tip deformation and crack growth in a nickel-based superalloy at elevated temperature," J. Mech. Phys. Solids, **56**(12), pp. 3363–3378.

[58] Bower, A. F., 2009, Applied mechanics of solids, CRC press.

[59] Gao, Y. F., and Bower, a F., 2004, "A simple technique for avoiding convergence problems in finite element simulations of crack nucleation and growth on cohesive interfaces," Model. Simul. Mater. Sci. Eng., **12**(3), pp. 453–463.

[60] Taha, A., and Sofronis, P., 2001, "A micromechanics approach to the study of hydrogen transport and embrittlement," Eng. Fract. Mech., **68**(6), pp. 803–837.

[61] Kwon, J., Bowers, M. L., Brandes, M. C., McCreary, V., Robertson, I. M., Phani, P. S., Bei, H., Gao, Y. F., Pharr, G. M., George, E. P., and Mills, M. J., 2015, "Characterization of dislocation structures and deformation mechanisms in as-grown and deformed directionally solidified NiAl–Mo composites," Acta Mater.,

89, pp. 315–326.

[62] Lu, H.-M., Delph, T. J., Dwyer, D. J., Gao, M., and Wei, R. P., 1996, "Pergamon 1359-6454(95)00405-X," Acta Metall., **44**(8), pp. 3259–3266.

[63] Wei, Y., Su, C., and Anand, L., 2006, "A computational study of the mechanical behavior of nanocrystalline fcc metals," Acta Mater., **54**(12), pp. 3177–3190.

[64] Corum, J. M., Blass, J. J., Ridge, O., and Ridge, O., 1991, "Rules for design of Alloy 617 nuclear components to very high temperatures," ASME PVP, **215**, pp. 147–153.

[65] Takahashi, Y., Dogan, B., and Gandy, D., 2009, "Systematic evaluation of creep-fatigue life prediction methods for various alloys," ASME 2009 Pressure Vessels and Piping Conference, American Society of Mechanical Engineers, pp. 1461–1470.

[66] Carter, P., 2005, "Analysis of cyclic creep and rupture. Part 1: bounding theorems and cyclic reference stresses," Int. J. Press. Vessel. Pip., **82**(1), pp. 15–26.

[67] Eno, D. R., Young, G. A., and Sham, T.-L., 2008, "A unified view of engineering creep parameters," ASME 2008 Pressure Vessels and Piping Conference, American Society of Mechanical Engineers, pp. 777–792.

[68] Yang, R. J., and Chahande, A. I., 1995, "Automotive applications of topology optimization," Struct. Optim., **9**(3-4), pp. 245–249.

[69] Huang, L., Pu, C., Fisher, R. K., Mountain, D. J. H., Gao, Y., Liaw, P. K., Zhang, W., and He, W., 2015, "A Zr-based bulk metallic glass for future stent applications: Materials properties, finite element modeling, and in vitro human vascular cell response," Acta Biomater., **25**, pp. 356–368.

[70] Liang, D. K., Yang, D. Z., Qi, M., and Wang, W. Q., 2005, "Finite element analysis of the implantation of a balloon-expandable stent in a stenosed artery.," Int. J. Cardiol., **104**(3), pp. 314–8.

[71] Lally, C., Dolan, F., and Prendergast, P. J., 2005, "Cardiovascular stent design and vessel stresses: a finite element analysis.," J. Biomech., **38**(8), pp. 1574–81.

[72] Marrey, R. V, Burgermeister, R., Grishaber, R. B., and Ritchie, R. O., 2006, "Fatigue and life prediction for cobalt-chromium stents: A fracture mechanics

analysis.," Biomaterials, **27**(9), pp. 1988–2000.

[73] Pelton, a R., Schroeder, V., Mitchell, M. R., Gong, X.-Y., Barney, M., and Robertson, S. W., 2008, "Fatigue and durability of Nitinol stents.," J. Mech. Behav. Biomed. Mater., **1**(2), pp. 153–64.

[74] Yukawa, S., 1991, "Elevated Temperature Fatigue Design Curves for Ni-Cr-Co-Mo Alloy 617," The 1st JSME/ASME joint international conference on nuclear engineering.

Vita

Chao Pu was born on March 28th, 1989 in Anshan City, Liaoning Province, China, a city known as "The Capital of Steels" in China for its steel production. He received his Bachelor's degree in 2012, majoring in Engineering Mechanics, from Shanghai Jiao Tong University in China. After undergraduate study, he came to USA in 2012 and enrolled in doctoral degree program in Department of Material Science and Engineering at the University of Tennessee, Knoxville in 2012, directly after his bachelor degree. The Doctor of Philosophy degree with a minor in Computational Science was received in December 2015. Following his PhD study, he works as a CAE Engineer at Fiat Chrysler Automobile in Auburn Hills, MI, USA.